The Energy Spectrum of Cosmic Electrons measured with the MAGIC telescopes

D i s s e r t a t i o n

zur Erlangung des akademischen Grades

d o c t o r r e r u m n a t u r a l i u m

(Dr. rer. nat.)

im Fach Physik

mit Spezialisierung Experimentalphysik

eingereicht an der

Mathematisch-Naturwissenschafltichen Fakultät

der Humboldt-Universität zu Berlin

von

Dipl.Phys. Ann Kathrin Mallot

Präsidentin der Humboldt-Universität zu Berlin:

Prof. Dr.-Ing. Dr. Sabine Kunst

Dekan der Mathematisch-Naturwissenschaftlichen Fakultät:

Prof. Dr. Elmar Kulke

Gutachter/in:
1. Prof. Dr. Elisa Bernardini
2. Prof. Dr. Marek Kowalski
3. Prof. Dr. Barbara de Lotto

Tag der mündlichen Prüfung: 27.01.2017

Abstract

This thesis seeks to further explore the origin of cosmic electrons and positrons. The unexpected excess of very-high-energy electrons above 100 GeV has been established and is now considered proof of a new class of electron sources. Many source classes ranging from astrophysical sources such as super nova remnants to decaying or annihilating DM have been proposed. While these models all explain the excess of cosmic electrons in the GeV range, they differ in the TeV range. Fermi-LAT and AMS-02 have performed precision measurements of the electron spectrum up to 1 TeV which show the flux following a single power-law with an index of -3.2. Measurements covering the energy range up to 6 TeV were performed by H.E.S.S. and VERITAS. They show a break at roughly 800 GeV and a strong decline of the cosmic electron flux above that. There are slight discrepancies in the flux normalization between H.E.S.S. and Fermi-LAT, as well as no break being seen by the satellite missions.

The measurement presented in this thesis seeks to provide an increased overlap of the Fermi-LAT and AMS-02 measurement, as well as the very-high-energy H.E.S.S. and VERITAS measurement. The MAGIC telescopes, a stereoscopic system of imaging air-shower Cherenkov telescopes, are a good candidate for such a measurement. They overlap largely with the Fermi-LAT energy range, down to 130 GeV, and extend into the energy range of the H.E.S.S. system, extending the measurement up to 4 TeV.

The measurement performed in this thesis uses a non-standard method developed especially for this analysis. It is based on a machine-learning-algorithm which differentiates between hadronic and electro-magnetic air showers. The background needs to be simulated from Monte Carlo protons, which were produced in large quantities for this thesis.

As this is an indirect detection method, the systematic uncertainties are much larger than those of the satellite missions. A detailed study of the systematic uncertainties was performed in the scope of this thesis, which prove to be much larger than the statistical uncertainties.

The measured spectrum presented here extends from 135 GeV up to 4 TeV. It shows no clear break in the spectrum and is in line with an extension of the single power-law observed by Fermi-LAT and AMS-02. A broken power-law interpretation was disfavored when compared to the single power-law. The final spectrum can be parameterized as follows:

$$\frac{\mathrm{d}F}{\mathrm{d}E} = (1.17 \pm 0.08_{\mathrm{stat}} \pm 0.47_{\mathrm{sys}}) \times 10^{-7} \times \left(\frac{E}{1\,\mathrm{TeV}}\right)^{-3.14\pm0.05_{\mathrm{stat}}\pm0.5_{\mathrm{sys}}} \mathrm{GeV}^{-1}\,\mathrm{m}^{-2}\,\mathrm{s}^{-1}\,\mathrm{sr}^{-1}$$

Due to the large uncertainties no definitive conclusion can be given at this point. Also, the cutoff seen by H.E.S.S. can not be ruled out. The result presented in this thesis is compatible with the Fermi-LAT and AMS-02 results, however there is minor tension with the H.E.S.S. and VERITAS results around 4 TeV. The limiting factor of the method is the large systematic uncertainty, making it impossible to distinguish between different electron sources for the results presented in this thesis.

Zusammenfassung

Diese Arbeit soll zu einem besseren Verständnis der Herkunft hochenergetischer kosmischer Elektronen und Positronen beitragen. In den letzten zehn Jahren haben verschiedene Experimente unabhängig voneinander bestätigt, dass der gemessene hochenergetische Elektronenfluss die erwartete Anzahl an Sekundärelektronen weit übersteigt. Aufgrund dessen wurden zahlreiche Modelle entwickelt, welche diesen Exzess als Primärelektronen aus bisher nicht berücksichtigten kosmischen Quellen beschreiben. Diese Quellen reichen von Pulsaren bis zu Dunkler Materie. Der ihnen zugeschriebene Elektronenfluss stimmt im GeV-Bereich mit den Präzisionsmessungen von Fermi-LAT und AMS-02 überein, unterscheidet sich aber zum Teil grundlegend im TeV-Bereich.

Die Satellitenmissionen Fermi-LAT und AMS-02 haben das Elektronenspektrum von 10 GeV bis 1 TeV vermessen. Der Fluss von Elektronen wird in diesem Energiebereich durch ein Potenzgesetz mit einem Spektralindex von -3.2 beschrieben. Oberhalb von 1 TeV wurde das Spektrum von H.E.S.S. bis zu 6 TeV vermessen. Die VERITAS-Kollaboration hat dieses Jahr ebenfalls ihr Elektronspektrum in diesem Energiebereich vorgestellt. Sowohl H.E.S.S. als auch VERITAS sehen einen Bruch im Spektrum bei etwa 800 GeV sowie einen darauffolgenden steilen Abfall des Flusses. Die Messungen von Fermi-LAT und AMS-02 können unterhalb von 1 TeV ein solches Einbrechen nicht bestätigen. Auch in der Normalisierung des Flusses sind kleinere Abweichungen zwischen den Ergebnissen der Satellitenmissionen und Cherenkov-Teleskope zu verzeichnen.

Die hier vorgestellte Analyse nutzt die MAGIC Teleskope, zwei abbildende Cherenkov-Teleskope, zum Vermessen des Elektronenflusses. Der Energiebereich dieser Teleskope überschneidet sich großflächig sowohl mit dem der Satellitenmissionen Fermi-LAT und AMS-02 als auch mit den hochenergetischen Messungen der Cherenkov-Teleskope VERITAS und H.E.S.S..

Die für diese Messung entwickelte Analyse weicht grundlegend von der Standardanalyse in MAGIC ab. Die Differenzierung von Signal und Untergrund kann nicht anhand der Richtung der eintreffenden Teilchen vorgenommen werden. Stattdessen basiert die Differenzierung auf einem Algorithmus für maschinelles Lernen, welcher eine Unterscheidung zwischen elektromagnetischen und hadronischen Luftschauern ermöglicht. Der Untergrund muss für diese Analyse anhand von Monte Carlo Simulationen geschätzt werden. Dafür wurden Protonen simuliert. Zudem liegt ein Schwerpunkt der Arbeit auf der Abschätzung systematischer Fehler und Unsicherheiten der neuen Analyse.

Diese Arbeit hat das Elektronenspektrum im Bereich von 135 GeV bis 4 TeV mittels der MAGIC Teleskope vermesssen. Das Spektrum lässt sich in diesem Bereich mit einem einfachen Potenzgesetz beschreiben:

$$\frac{\mathrm{d}F}{\mathrm{d}E} = (1.17 \pm 0.08_{\mathrm{stat}} \pm 0.47_{\mathrm{sys}}) \times 10^{-7} \times \left(\frac{E}{1\,\mathrm{TeV}}\right)^{-3.14 \pm 0.05_{\mathrm{stat}} \pm 0.5_{\mathrm{sys}}} \mathrm{GeV}^{-1}\,\mathrm{m}^{-2}\,\mathrm{s}^{-1}\,\mathrm{sr}^{-1}$$

Erwartungsgemäß sind die Unsicherheiten dieser indirekten Messmethode deutlich größer als bei direkten Messungen der Satellitenexperimente. Aufgrund der großen Unsicherheiten kann ein Bruch bei 800 GeV jedoch auch nicht ausgeschlossen werden. Die hier präsentierte

Messung stimmt innerhalb der Fehler mit den Ergebnissen von AMS-02 und Fermi-LAT sowie innerhalb von zwei Standardabweichungen mit den Messungen von H.E.S.S. und VERITAS überein. Eine Interpretation des Elektronenflusses gestaltet sich aufgrund des großen Fehlers als schwierig. Im Endeffekt kann keine der potentiellen neuen Quellen kosmischer Elektronen ausgeschlossen werden.

Contents

Introduction

Cosmic rays give us the unique possibility to learn more about our universe at distances out of mankind's reach. They travel close to the speed of light and can cover huge distances of up to 93 billion light years. However, not all cosmic rays are equally likely to reach the Earth from such distances. In particular the cosmic electrons on which this thesis will focus, reach Earth from much smaller distances. This is due to the strong energy losses they undergo in the magnetic field of the Milky Way. In fact cosmic electrons reaching Earth with energies higher than 1 TeV originate at distances of less than a few kpc, making close-by astrophysical objects the most likely sources.

The energy spectrum of cosmic electrons has been measured by a multitude of experiments over the last 30 years. The first measurements were done by balloon flights, followed by satellite missions as well as ground based experiments. The MAGIC telescopes, a system of two 17 m-diameter imaging Cherenkov telescopes, have a lower energy threshold than the competing ground-based imaging atmospheric Cherenkov telescopes, H.E.S.S. and VERITAS. As such, they offer a good overlap with both the satellites mission and the other Cherenkov telescopes. This is of particular interest as the Cherenkov telescopes observe a cutoff in the electron spectrum just above the energy range measured by the satellites.

This thesis presents the final electron spectrum as measured by MAGIC. The electrons are a diffuse flux making the determination of the spectrum proves challenging, as the telescopes are not optimized for diffuse measurements. The standard point-source analysis can not be applied in this case as it uses the incoming direction of the cosmic ray: cosmic rays coming from the position pointed at are considered signal events and the rest is being considered background. A simultaneous measurement of the background at a small offset allows to calculate the background contamination in the signal in the point-source analysis.

For the diffuse measurement, presented in this thesis, the direction information can not be used. A new analysis had to be developed. It is based on differentiating between the images produced by hadronic and electro-magnetic air showers on the ground. The background estimation is done from Monte Carlo simulations of protons, which constitute the majority of cosmic rays. This measurement is affected by large systematic uncertainties stemming from the experimental setup not being optimized for this type of analysis. Additional theoretical uncertainties are due to the limited knowledge of the relevant strong interaction physics at high energies needed for the simulations of protons.

This thesis is structured in five chapters:

- The first chapter covers the theoretical motivation for this measurement, as well as possible source classes for the observed electron flux.

- The second chapter describes the experimental setup and standard analysis performed for point-like sources.

- The third chapter is dedicated to the new method developed for the measurement of diffuse fluxes.
- The fourth chapter presents the results of the method and the electron spectrum as measured by the MAGIC telescopes.
- The fifth and final chapter is a detailed study of the systematic uncertainties affecting the method presented in this chapter.

1. Cosmic electrons and positrons

This chapter gives a summary of the scientific motivations for the study of the electron spectrum, as well as a general overview of cosmic ray physics presenting their (assumed) origin, propagation and composition. It also gives a historical overview of the measurements of the electron spectrum. The focus will be put on the energy range of very-high-energy cosmic rays, roughly between 100 GeV and 100 TeV as this is the energy range of interest for this thesis.

In section 1.1 a brief overview of cosmic rays will be given, followed by the propagation of the cosmic rays in section 1.2 and the possible origins of the observed very-high-energy electrons and positrons in section 1.3.

1.1. Cosmic Rays

At the beginning of the 20th century Domenico Pacini showed that measured natural radioactivity was not coming from the Earth's crust as previously assumed[149]. It was Victor Hess who discovered shortly thereafter the incoming highly energetic cosmic radiation through a series of balloon flights[89]. In 1926, Millikan suggested an extra-terrestrial origin of the radiation and named it cosmic rays[133]. It was already clear, that the particles observed in balloon flights were not the primary cosmic particles[68]. During the next decade, Auger and Rossi studied the composition of the secondary particles observed on the ground and discovered that cosmic ray particles initiated air-showers[48, 49]. The first direct detection of cosmic rays happened in the 1950s with the help of satellites[123, 125].

This was the starting point of the field of astroparticle physics. To this day cosmic rays are the object of scientific interest and detailed measurements as their origin remains under debate.

The flux of cosmic rays is usually given in terms of particles per unit time, area, solid angle and energy. This is the differential flux:

$$\Phi(E) = \frac{\text{particles}}{dA\, dt\, d\Omega\, dE}, \tag{1.1}$$

where E is the energy, A is the area, t is the time unit and Ω the solid angle. Alternatively the flux can be given as integral flux, giving the total flux of all particles with energy higher than E. It is a function of area, time and solid angle:

$$\Phi(E) = \frac{\text{particles}}{dA\, dt\, d\Omega}. \tag{1.2}$$

Cosmic rays consist in large parts of protons and atomic nuclei, while electrons, positrons and photons represent only a small percentage. The differential energy spectrum of cosmic electrons and positrons is also less well known than the hadronic spectrum. It is known to

be steeper, meaning that it is dominated by low-energy particles. This is to be expected, as electrons and positrons suffer greater energy losses by synchrotron radiation due to the galactic magnetic field.

A summary plot of the known differential spectra of the main components of cosmic rays is shown in Fig. 1.1. This section will first discuss the main component of cosmic rays: the hadronic part, followed by the electrons, positrons and the diffuse γ-rays.

1.1.1. Hadronic cosmic rays

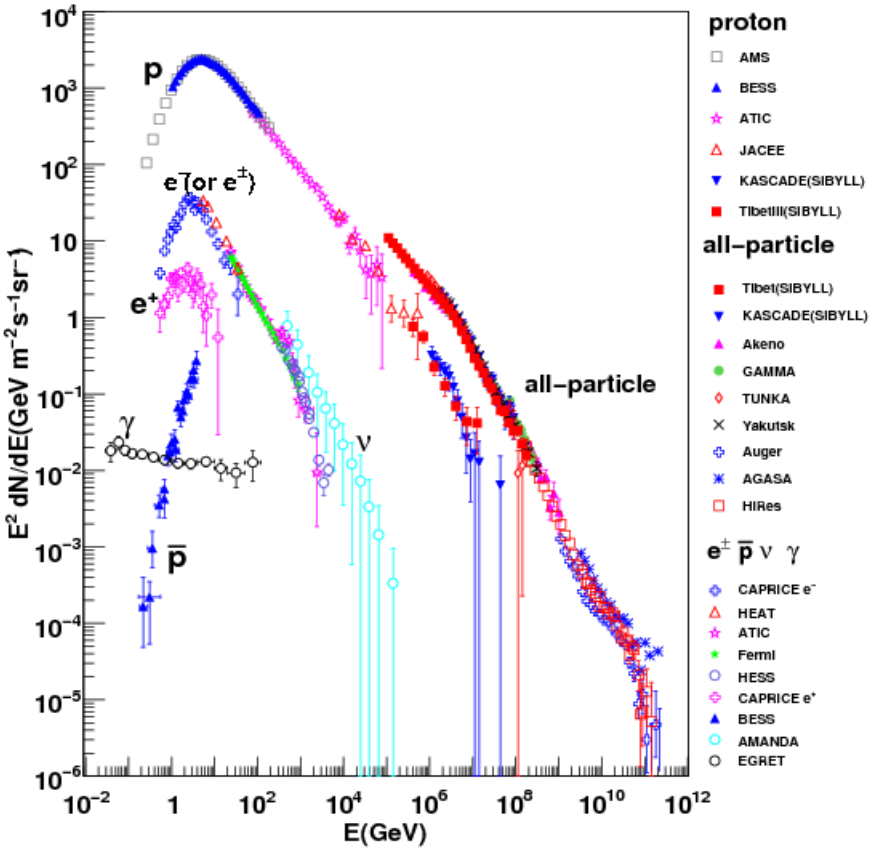

Figure 1.1: Measurement of the total cosmic ray flux over the entire known energy range, as well as the individual flux for protons, anti-protons, electrons and positrons at low energies. Taken from [111].

Hadronic cosmic rays have been measured over twelve decades in energy and about 30 decades in flux, as seen in Fig. 1.1.

Below 1 TeV, different particle types have been measured separately and their individual differential energy spectra are known, while for the highest energies only the total differential flux of cosmic rays is known. Here the composition is less clear and only upper limits of the

integral flux of different particle types are known. In the simplest approximation cosmic rays follow a pure power law over a wide range of energies:

$$\Phi(E)dE = E^{-\alpha}dE. \tag{1.3}$$

α is the spectral index of the cosmic ray flux. There are two main features: The so-called knee at 4×10^{15} eV, steepening the spectral index from $\alpha = -2.7$ to $\alpha = -3.1$, and the ankle at 3×10^{18} eV where the spectrum hardens again to $\alpha = -2.7$[86].

The current understanding of the cosmic ray spectrum is that galactic cosmic rays contribute dominantly below the knee, while the dominant contribution above the knee stems from extragalactic sources[108, 181]. Recently, the idea of a galactic contribution above the knee has become more popular[86, 176].

However, as the energy range of interest for this thesis does not reach energies above the knee, this will not be explored in detail.

It is considered proven that the bulk of cosmic rays below the knee is of galactic origin. For one, in the GeV regime, extensive measurements have been done showing that the intensity of the flux of cosmic rays decreases as one moves away from the galactic plane[4]. This allows to conclude that cosmic rays at those energies are accelerated inside the galaxy. In addition the measurement of the diffuse γ-rays above 100 MeV is in good agreement with the expected flux from neutral pion decay of hadronic cosmic rays colliding with the gas in the Milky Way[4]. Last but not least the γ-ray emission above 100 MeV measured in the small Magellanic cloud shows a substantially lower cosmic ray density than the density in the Milky Way[7, 168], proving that the Milky Way is not submerged in a sea of extragalactic cosmic rays, but rather that the cosmic rays are generated in the galaxy.

Taking into account the energy range of the analysis presented in this thesis, the cosmic rays measured will mostly be galactic. Both, for the hadronic cosmic rays that constitute the background for presented analysis and the signal of cosmic electrons and positrons. In the remainder of this section, the galactic origin of cosmic rays will be covered, followed by a short overview of the main extragalactic sources.

1.1.2. Galactic sources of cosmic rays

The spectrum of cosmic rays measured at Earth is limited at low energies by solar activities. Solar winds and the expanding magnetized plasma prevent charged cosmic rays below 300 MeV from entering the solar system due to deceleration. Up to 10 GeV cosmic rays are still affected by solar winds. They show an anti-correlation between the solar activity and the total flux based on the 11-year-cycle of solar activity[26, 144]. Indirect measurements of the cosmic ray flux are performed by studying the behavior of passive molecular clouds. By measuring the γ-ray flux at low energies from passive molecular clouds, one can recover the amount of low energy cosmic rays interacting with the gas. The results are based on the assumed interaction and a free line of sight between the cloud and the observer. Such measurements have been performed by Fermi-LAT[143, 188], extending the measurement of the unattenuated cosmic ray spectrum down to 1 GeV.

The decomposition of the cosmic ray flux into different particles is well documented[116]. The measured spectra of its main components can be seen in Fig. 1.1. The total flux roughly consists of 87% protons and 12% helium, the contribution of heavier elements is

negligible in the energy range relevant for this thesis. The composition is in agreement with solar abundance[166], which implies that cosmic rays are simply accelerated matter. The primary method of acceleration for galactic cosmic rays is thought to be by diffuse shock acceleration in super nova remnant (SNR), which will be illustrated in the next section.

In an exploding supernova the outer shell of the star is ejected and preceded by a shock front traveling at supersonic speeds through the Inter Stellar Medium (ISM). This is called the free expansion phase during which the ISM is accumulated in front of the expanding shell.

As the mass accumulates in front of the shock wave of the expanding SNR, it is slowed down. The matter density inside the expanding wave increases at the border between the shock wave and the accumulated ISM. This generates an internal shock reheating the gas inside the shock wave and is known as the second phase of the expansion, also called adiabatic phase. The first two phases are thought to be the main phases in which cosmic rays are accelerated by the diffuse shock acceleration explained below.

The final phase, the radiative phase, starts at $\sim$ 10000 years and the energy losses of the shock front are mostly radiative. It no longer accelerates surrounding particles.

1.1.3. Diffuse Shock Acceleration

SNR being the main source of cosmic rays in this galaxy, the diffuse shock acceleration will be explained in the context of the SNR. However, any shock front, as present in gamma ray bursts, pulsar wind nebulae or active galactic nuclei, is expected to accelerate particles with the same mechanism.

The benefit of the diffuse shock acceleration, is that it is collisionless, so every interaction results in an energy gain for the particle. There are two mechanisms called first-order and second-order Fermi acceleration. They are named after Enrico Fermi, as the idea of energy gain of a scattered particle in a moving, ionized medium was first proposed by him in 1949[92]. first-order and second-order refers to the energy gain per shock crossing which is proportional to the speed of the shock front, divided by the speed of light: $\frac{v}{c}$ or its square.

Second-order Fermi acceleration

The original idea of Fermi is now known as second-order acceleration, as it is proportional to the squared velocity: $(\frac{v}{c})^2$. It needs a molecular cloud to interact with.

Fermi's idea has cosmic rays gaining energy from collisions with molecular clouds. The particle gains energy from a head-on collision, where the particle and the cloud move in opposite directions. It loses energy from tail-on collisions, where the particle and the cloud move in the same direction. During the collision, energy is transferred from the cloud to the particle and the energy gain will be[126]:

$$\Delta\mathcal{E} = \mathcal{E}\left(\frac{2Vv\cos\theta}{c^2} + 2\left(\frac{V}{c}\right)^2\right), \tag{1.4}$$

with $\mathcal{E}$ being the particle energy, V being the speed of the molecular cloud, v being the speed of the particle and θ being the angle of collision. Averaging over the angle of incidence

yields[117]:

$$\left\langle \frac{\Delta \mathcal{E}}{\mathcal{E}} \right\rangle = \frac{8}{c} \left(\frac{V}{c} \right)^2, \tag{1.5}$$

resulting in an energy gain proportional to $\left(\frac{V}{c}\right)^2$. The major drawback of this acceleration method is that it is very inefficient with only a few interactions per year. Additionally most clouds move with non-relativistic speeds, limiting the energy gain.

First-order Fermi acceleration

The idea was expanded on by several people and became the first-order Fermi acceleration, which is today assumed to be the main acceleration mechanism in SNR[52, 62].

As an illustration, the Bell approach[52] to the first-order Fermi acceleration is given here. It is based on the assumption of an isotropic distribution of cosmic rays on both sides of the expanding shock wave. The isotropization is important, as it enables the particles to cross the shock several times. With every crossing of the shock a net energy gain is achieved, so a high probability of having multiple crossings is desired. To quantify the probability, one can look at the number of particles escaping downstream versus the number of particles located at the shock. The particle density downstream of the shock is defined by the amount of particles n, advecting away from the shock with velocity u_2: nu_2.

The number of particles crossing the shock from upstream to downstream is $\int_0^1 \mu c n \frac{d\mu}{2} = \frac{nc}{4}$[85], where μ is the pitch of the particle and c is the speed of light. This is the particle's velocity relative to the local fluid frame, since the particles are assumed to be relativistic. Then the fraction of particles not returning to the shock is $\frac{nu_2}{nc/4}$. That means the probability of a recrossing is:

$$P = 1 - 4\frac{u_2}{c}, \tag{1.6}$$

which is close to 1 for non-relativistic shocks.

The energy gain can be gathered from Lorentz-transforming the particle's energy when it passes into the downstream region[163]:

$$E' = \gamma_v \left(E + p_x v\right) = E\left(1 + \cos(\theta)\frac{v}{c}\right). \tag{1.7}$$

$v = u_1 - u_2 = \frac{3}{4}U$, where U is the speed at which the shock is moving. Since $U \ll c$ is assumed, the Lorentz-factor can be set to $\gamma_v = 1$, while the particles are assumed to be moving at relativistic speeds allowing for $E = pc$ and $p_x = \frac{E}{c}\cos(\theta)$.

Integrating over the angle to get the average energy gain and doubling the energy gain for a round trip yields:

$$\left\langle \frac{\Delta E}{E} \right\rangle = \frac{4}{3}\frac{v}{c}. \tag{1.8}$$

The energy gain is the same crossing the shock in both directions, as the sign is inverted for $v = u_2 - u_1$ and p_x.

For the first-order acceleration the energy gain is proportional to $\frac{v}{c}$ and not its square, making the acceleration more efficient.

Another feature of this acceleration is the recovery of the observed energy spectrum: after i cycles the number of particles N will be $N_0 P^i$, where N_0 is the original amount of particles, P is defined in Eq. 1.6 as the probability of the particle remaining in the acceleration region. The average energy of the particles is defined as $E = \beta^i E_0$, where E_0 is the original energy average and β is the average energy gain:

$$\beta = \frac{E}{E_0} = 1 + \frac{4}{3}\frac{v}{c}. \tag{1.9}$$

Solving for i yields:

$$\frac{\ln(N/N_0)}{\ln(E/E_0)} = \frac{\ln(P)}{\ln(\beta)}. \tag{1.10}$$

Which gives:

$$\frac{N}{N_0} = \left(\frac{E}{E_0}\right)^{\frac{\ln(P)}{\ln(\beta)}}. \tag{1.11}$$

Inserting P, β and v into the exponent:

$$\frac{\ln(P)}{\ln(\beta)} = \frac{\ln\left(1 - 4\frac{u_2}{c}\right)}{\ln\left(1 + \frac{4}{3}\frac{u_1 - u_2}{c}\right)} \approx \frac{-4\frac{u_2}{c}}{\frac{4}{3}\frac{u_1 - u_2}{c}} = -\frac{3}{\left(\frac{u_1}{u_2} - 1\right)}. \tag{1.12}$$

The ratio $r = \frac{u_1}{u2}$ is also known as the compression ratio of the shock. Based on the Rankine-Hugoniot conditions[113, 158] one can show that the compression radio for a monatomic non-relativistic gas is $r = 4$[85]. Inserting this in Eq. 1.11, one recovers:

$$N(E)dE \propto E^{-1+\frac{-3}{r-1}} dE = E^{-2} dE. \tag{1.13}$$

This also shows that the energy spectrum of the cosmic rays only depend on the compression ratio of the shock, and no other parameters. This fits well with the fact that the galactic cosmic ray spectrum seems to have a single generic spectral index.

If a particle escapes the acceleration region, it will no longer be accelerated. The maximal energy can be quantified as:

$$E_{MAX} = zBL. \tag{1.14}$$

Where z is the charge of the particle, B is the magnetic field and L is the size of the acceleration region. The maximal energy comes from the condition that the Larmor radius $r_L = \frac{E}{zB}$ must be smaller than the acceleration region. This is known as the Hillas criterion[105].

The simple case presented here can accelerate particles up to $\sim 10^{14}$ eV. In recent years acceleration to higher energies thanks to magnetic field amplification[53] was discussed allowing to extend the acceleration of protons up to 10^{16} eV to 10^{17} eV using strong magnetic fields observed in young SNRs[182].

Regardless of which acceleration mechanism is used, the fact that hadronic matter is accelerated in SNR seems very likely. In particular for protons, the observation of a γ-ray spectrum characteristic for the π^0 decay by Fermi-LAT in SNR[18] is compelling evidence there are p-p collisions and hence acceleration there. More recently H.E.S.S. published

evidence of PeV protons in the galactic center[12], suggesting that cosmic rays are also being accelerated by super massive black holes.

1.1.4. Extra-galactic sources of cosmic rays

In a simplified picture extragalactic cosmic rays start becoming dominant above the knee, following a simple power-law up to the ankle and beyond, while the galactic component slowly declines. However, the flux is not a pure power-law, as several features have been observed within that range, e.g. the second knee. These features are likely due to a change in cosmic ray composition. The galactic iron component dying out could be the origin of the second knee[45].

It is believed that there is a variety of extragalactic sources which accelerate the ultra-high-energy cosmic rays (Energy $> 10^{18}$ eV), even if the acceleration mechanism is expected to largely be the first-order Fermi acceleration. As shown in Eq. 1.14, the acceleration only depends on the magnetic field and the size of the acceleration region. Possible source classes can then be classified in a so-called Hillas plot[105], as shown in Fig. 1.2. In particular for energies above 10^{18} eV particles can no longer be contained within the galaxy and must be extragalactic. Active galactic nuclei seem to be a likely candidate, however, the evidence so far is mostly incidental[140]. Not much is known about the flux above the ankle due to the

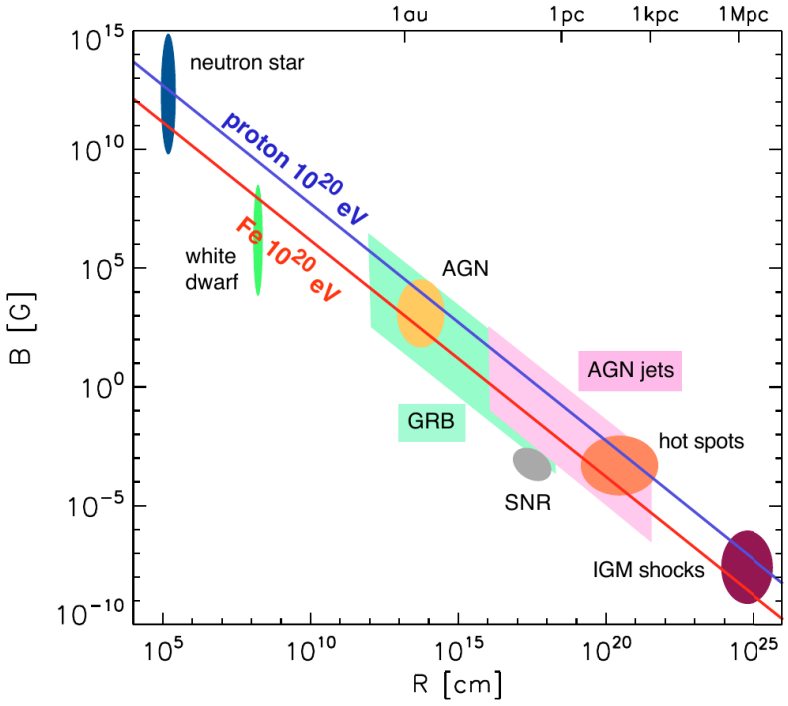

Figure 1.2: Hillas diagram showing the di erent source classes and their acceleration potential for cosmic rays. Taken from [122].

extremely low flux. The flux is about 0.5 to 1 event per century per square kilometer per steradian. In addition, at ultra-high energies cosmic rays start interacting with the cosmic

microwave background (CMB) and lose energy before reaching earth, further reducing the flux. The dominating interactions at those energies are:

$$\begin{aligned} \gamma_{CMB} + p \rightarrow \Delta^* \rightarrow & p + \pi_0 \\ \gamma_{CMB} + p \rightarrow \Delta^* \rightarrow & n + \pi^+ \end{aligned} \tag{1.15}$$

This is known as the Greisen–Zatsepin–Kuzmin (GZK) cutoff[102, 190] and has been confirmed by AUGER and HiRES[3, 13] as can be seen in Fig. 1.1. However, some tension remains concerning the composition of ultra-high energetic cosmic rays. The cutoff could also be due to sources reaching their maximum acceleration power[185]. The blue line in Fig. 1.2 indicates the conditions needed for protons to be accelerated to 10^{20} eV, excluding already most of the known sources of cosmic rays. Recent reviews show the known acceleration mechanisms can not exceed 10^{21} eV[148]. This implies that the cosmic ray spectrum has been measured to its full extend possible in our solar system. It is limited from the lower end by the solar interference and on the upper end by the GZK-cutoff or possibly the power of the accelerators of cosmic rays.

1.1.5. Electrons

In the analysis part of this thesis, electrons usually refers to both cosmic electrons and positrons as they can not be distinguished experimentally with the method presented here. Electrons and positrons as charged, light particles are limited in distance by the energy losses incurred from the galactic magnetic field. This means, that very-high-energy electrons and positrons can reach us from no further than roughly the edge of our galaxy. A quantitative description of why the range is limited and how the electrons and positrons propagate will be provided in section 1.2. In the simplest models the origin of propagated electrons and positrons is the same source as for galactic hadronic cosmic rays: SNR. Even though the picture is less clear than for hadronic particles.

The energy gap between thermal energy and the energy at which the particles can be accelerated are small for protons and ions, but quite large for electrons and positrons. An initial acceleration of electrons and positrons is needed for the particles to reach the minimal energy to be further accelerated by diffuse shock acceleration. This is known as the injection problem and is still under analysis today, see for example[137].

The galactic magnetic field also modifies the flight direction of the particle itself, so that the original source of electrons and positrons can not be determined from the reconstructed direction in the detector. Hence only the diffuse incoming flux can be measured. The flux is assumed to be homogeneous, although that may be an oversimplification as discussed in section 1.2.1.

There must be an additional source of primaries, in particular of primary positrons. Even with a careful treatment of all theoretical uncertainties, the current model can not be reconciled with the measured spectra[83]. A short overview of the measurements will be given here, a detailed explanation of the sources of galactic electrons and positrons will follow in section 1.3.

The measurement of most energetic electrons and positrons are currently done by imaging air Cherenkov telescopes, such as MAGIC. MAGIC is in a unique place, as its energy range actually extends down to a few 100 GeV allowing for a good overlap with the highest

current precision measurements of the electron spectrum done by satellite missions. The other imaging air Cherenkov telescopes, VERITAS and H.E.S.S., have a higher energy threshold and therefore only overlap in a small range with the satellite missions.

Measuring the energy spectrum of cosmic electrons and positrons

Originally the total cosmic ray and the electrons and positrons spectrum were measured with balloon experiments. But the balloon experiments are limited in their size and exposure time by the balloon carrying the experiment and therefore can not reach very-high-energy ranges. The latest measurements for the electron spectrum have consequently been done via satellite measurements and ground-based Cherenkov telescopes. The latter have yielded first results in the TeV range. A summary of the most recent results is shown in Fig. 1.3.

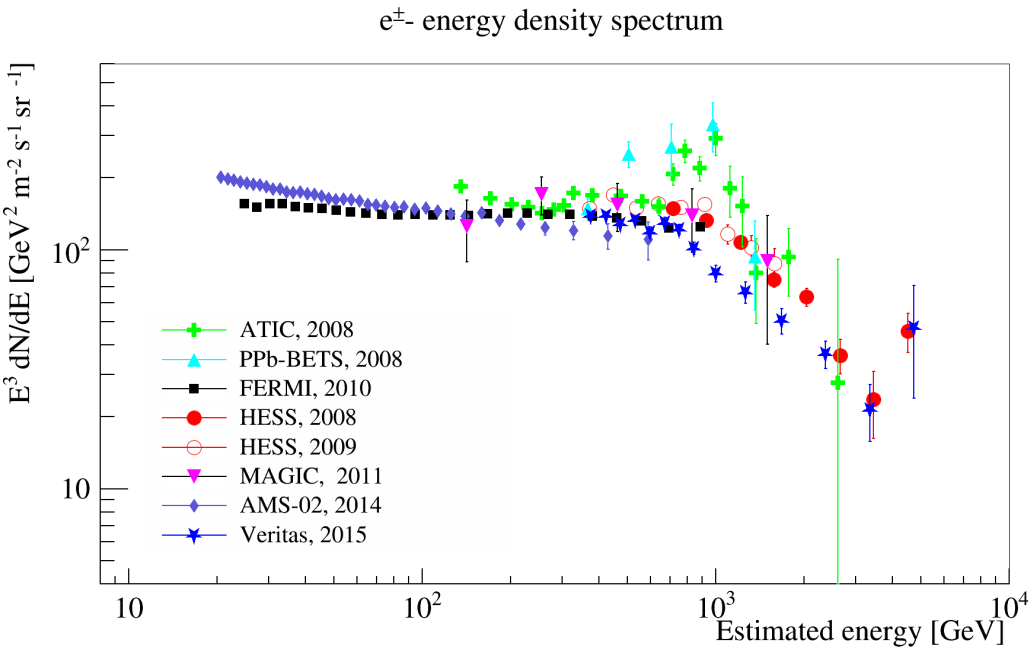

Figure 1.3: Energy density spectrum of cosmic electrons and positrons as measured by Fermi-LAT[5, 21],ATIC[73],PPB-BETS[189], H.E.S.S.[34, 87], MAGIC[66], AMS-02[32] and VERITAS[169]. Systematic uncertainties are not included.

Balloon experiments Balloon experiments, in general, were the first method of choice, as planes could not reach the altitudes necessary for the studies at the beginning of the 20th century. However, since this thesis focuses on the GeV–TeV energy range, the first experiment of interest dates back to 1980 with the measurement of cosmic electrons and positrons ranging between 30 GeV and 1 TeV[145]. The group used an emulsion chamber consisting of layered lead plates, X-ray sensitive films and emulsion layers which was launched on a balloon and later read out by hand. Several such balloon flights took place in the last century in Japan and in the US. The latest combined, updated data was published in 2012[120].

Balloon flights are not permanent installations, but are usually flown for a few days, before being collected and read out. In order to allow for longer flight times, several balloon flights were launched from Antarctica at the beginning of this century. These balloons no longer used a simple emulsion chamber, but rather expanded the concept using complex detectors. PPB-BETS used a calorimeter composed of scintillating-fiber belts and plastic scintillators alternating with lead plates and three trigger plates (top, middle, bottom) to veto up-going events[189]. Contrary to PPB-BETS, ATIC was more geared towards heavier elements, consisting of a silicon matrix for charge reconstruction, three hodoscopes for charge and trajectory reconstruction followed by a carbon target and a calorimeter. Both PPB-BETS and the ATIC experiment measured a peak at roughly 600 GeV in the otherwise featureless spectrum ranging from 10 GeV to 1 TeV[73].

An attempt was made to measure the electron spectrum in the TeV range with a balloon experiment by CREST in 2011. However, the collaboration came to the conclusion that due to the high background of hadronic cosmic rays, they would be unable to extract a signal. They gave an upper limit for the integral flux above 15 TeV of $7.11 \times 10^{-3}\,\mathrm{m^{-2}s^{-1}sr^{-1}}$[142].

Satellites After the success of balloon flights mapping the electrons and positrons spectrum up to roughly 1 TeV, the next step was the precision measurement of the electron spectrum in the same energy range. The Fermi-LAT satellite was launched in 2008 and consists of a particle tracker and a calorimeter covered by anti-coincidence shields[47]. Its components were tested in a beam to calibrate the detector and study uncertainties. They published their electrons and positrons spectrum from 20 GeV to 1 TeV in 2008[5]. Extending it down to 7 GeV in 2010[21].

The latest space mission to publish their electrons and positrons spectrum is the AMS-02 experiment which is located on the International Space Station (ISS). The results were published in 2014[32] and are compatible within one standard deviation with the Fermi-LAT results. Neither Fermi-LAT nor AMS-02 confirm the bump seen by ATIC at 600 GeV. A subsequent reanalysis of the ATIC data showed that the results are not compatible with Fermi-LAT within systematic uncertainties and show further substructures in the spectrum[151]. Today, the so-called ATIC-bump is considered ruled out, as neither Fermi-LAT[5, 21], AMS-02[32], H.E.S.S.[34] nor VERITAS[169] could reproduce the bump.

Ground based observations Simultaneously to the precision measurement up to 1 TeV, the spectrum was extended up to even higher energies using a new approach. This was first done by the H.E.S.S. telescopes, who published their result in 2009, extending the known spectrum up to 6 TeV[87]. Followed by MAGIC in 2011[66] and VERITAS in 2016[169]. This thesis will show the final spectrum by MAGIC extending it up to 3 TeV. MAGIC operates in a similar energy range as VERITAS and H.E.S.S., but extends down to lower energies giving a better overlap with other experiments, such as Fermi-LAT.

Future experiments In August of last year, the CALET experiment was sent to the ISS[130], it has an operating range up to 100 TeV for heavier elements and up to 10 TeV for electrons and positrons. The results are expected within the next 5 years extending the precision measurement up to 10 TeV.

1.1.6. Positron fraction

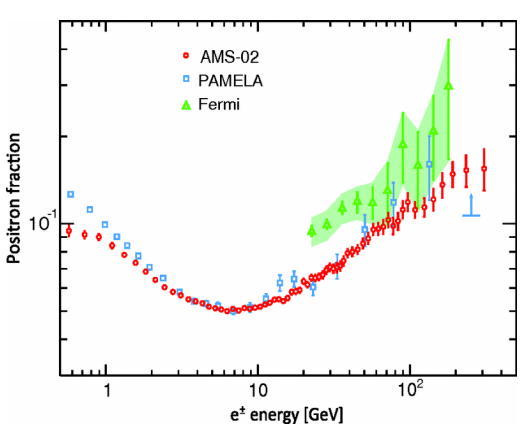

(a) The increase in the positron fraction as measured by PAMELA[28], Fermi-LAT[17] and AMS-02[14]. Taken from [33].

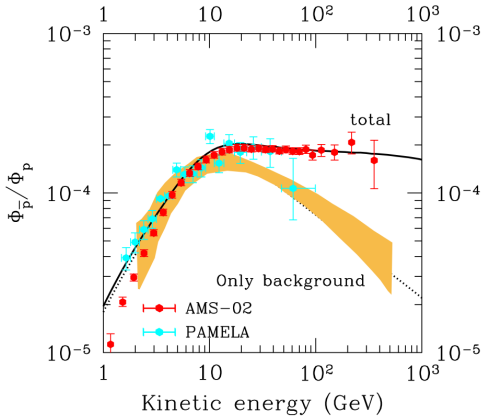

(b) anti-proton to proton ratio as measured by PAMELA[29] and AMS-02[1]. Taken from [121].

Figure 1.4: The most recent measurements of the positron and anti-proton fraction.

The basic model of cosmic rays proposed the flux of electrons and positrons consisting of primary electrons accelerated in SNRs and secondary electrons and positrons coming mostly from spallation. This implies that the positron flux decreases faster than the electron flux with energy. The positron fraction, defined as the flux of positrons, divided by the flux of positrons and electrons, has gotten a lot of attention over the past few years[91, 129, 132].

Recent experiments show a clear increase of the positron ratio at high energies. This is shown in Fig. 1.4a.The three most recent measurement done by PAMELA, Fermi-LAT and AMS-02 all confirm the increase in high-energy positrons with respect to electrons.

The positron fraction is a smoking gun for a new source class of very-high-energy electrons and positrons, in addition to the already mentioned excess at high energies for the combined electron-positron flux. In this context it is also important to look at the anti-proton flux, as it helps distinguish between several source classes. The PAMELA experiment saw a decrease compatible with the expected values from pure secondary production[29]. More recently, AMS-02 showed results suggesting an overabundance of high-energy anti-protons as well[1], shown in Fig. 1.4b. These results are preliminary, the final spectrum by AMS-02 remains to be published and might deviate quite strongly from the currently latest results as they identified a problem with their data analysis recently which was over-smoothing their data.

This is still a very active field, making a definite statement on the origin of very-high-energy electrons and even more so very-high-energy positrons difficult. Possible sources are given in section 1.3.

1.1.7. Diffuse gamma ray

Another noteworthy cosmic ray component for the energy range and analysis of this thesis are γ-rays. Notably the diffuse flux of γ-rays since the analysis presented in this thesis can not distinguish them from the signal, the electrons and positrons. This means they are an irreducible background and their contribution needs to be quantified to be able to rule out significant distortion in the final all electron spectrum by them. It is necessary to distinguish between two different components: First the galactic diffuse γ-ray emission and second the extragalactic γ-ray emission. Since the γ-rays are not electrically charged they are not deflected by magnetic fields and their arrival direction points back to their origin. This is different from the previously discussed cosmic rays and allows to separate galactic and extragalactic spatially. However, the extragalactic gamma ray background (EGRB) depends on the assumed foreground of galactic γ-ray flux[21].

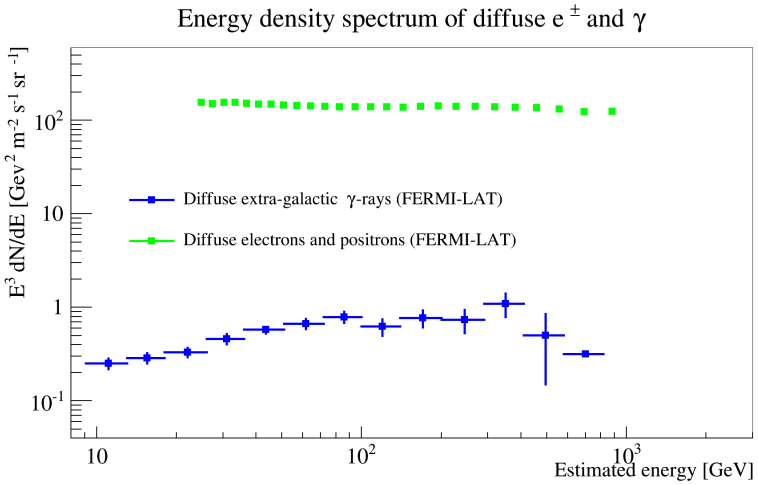

Figure 1.5: Diffuse extragalactic γ-ray flux and diffuse electron and positron flux as measured by Fermi-LAT. Data taken from [16] and [21].

The galactic diffuse γ-ray flux is understood to be produced by interactions of very-high-energy cosmic rays with the ISM. At low energies it actually dominates over the emission from resolved sources[22]. At high energies, the diffuse galactic γ-ray fluxes is expected to come in large parts from unresolved sources. Also bremsstrahlung becomes negligible and the main generating mechanism are expected to be π_0 decays from protons and inverse Compton for electrons and positrons [126]. They are expected to mirror the distribution of matter in the galaxy, in particular nearby molecular clouds, as evidenced by Fermi-LAT observations[19, 139].

The diffuse flux measured at 1 TeV is $3 \times 10^{-9}\,\mathrm{TeV}^{-1}\,\mathrm{s}^{-1}\,\mathrm{cm}^{-2}\,\mathrm{sr}^{-1}$[11]. At high energies the galactic diffuse γ-ray flux reaches the same order of magnitude as the diffuse electron flux and therefore can not be discounted. The galactic γ-ray flux comes from the galactic plane while electron and positrons are supposed to be isotropic. Therefore this analysis requires that the data used be taken with an offset of at least ten degrees of the galactic plane to avoid contamination from the galactic diffuse γ-ray flux.

At larger latitudes, a second component is observed isotropically above the sky, the EGRB. The current best understanding is that the diffuse γ-ray component mostly comes from unresolved sources. Indeed, it is believed that 86% of the flux above 50 GeV can be accounted for by just one class of unresolved sources: blazars[15]. Fermi-LAT measurement of the EGRB up to 800 GeV[6, 16] is shown in Fig. 1.5. The diffuse γ-ray flux is about two orders of magnitude lower than the one of electrons and positrons. So a separation of the diffuse γ and electrons and positrons is not needed. The contribution of the EGRB to the total flux will be in the low percentage and is well within the systematic uncertainties of the experimental setup detailed in chapter 5.

1.2. Propagation of electrons and positrons

As electrons and positrons are charged particles, they interact with the magnetic field inside our galaxy. Since this magnetic field is not homogeneous, particles are deflected and information about the origin of the particle is lost. All that can be studied is the diffuse flux of incoming electrons and positrons. The propagation of electrons and positrons in the galaxy can be described by a diffusion-loss equation. The propagation will be explained for electrons, it is the same for positrons. Electrons suffer strong energy losses due to synchrotron radiation. This energy loss, as well as the energy loss from inverse Compton scattering on photons, is proportional to E^2, whereas the losses of bremsstrahlung go with E as shown in Eq. 1.16[126]:

$$-\frac{dE}{dt} = A_1 \left(\ln \frac{E}{m_e c^2} + 19.8 \right) + A_2 E + A_3 E^2. \tag{1.16}$$

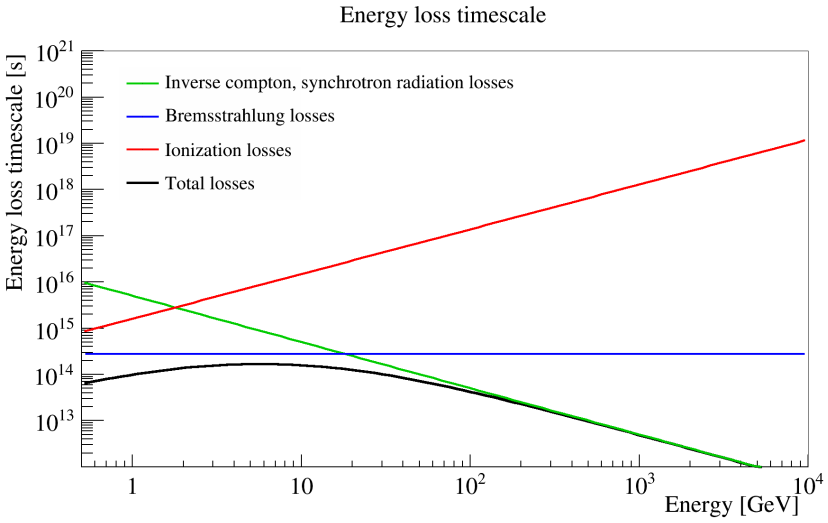

Figure 1.6: The timescale on which a particle looses its energy due to the different processes listed in Eq. 1.16

A_1 describes the energy losses due to ionization, A_2 the previously mentioned energy losses by bremsstrahlung and adiabatic losses and lastly A_3, which is the dominant contribution

at high energies coming from inverse Compton and synchrotron radiation. In Fig. 1.6, the inverse Compton and synchrotron losses dominate above a few GeV, while the adiabatic and ionization losses become negligible. Therefore in the GeV-regime (and higher) the lower order terms can be neglected and the energy loss rate can then be defined as the one of A_3:

$$\begin{aligned} \frac{dE}{dt} &= -bE^2 := b(E) \qquad \text{with} \\ b &= \frac{4\sigma_T c}{3\left(m_e c^2\right)^2}\left(\frac{B^2}{8\pi} + \omega_{ph}\right). \end{aligned} \tag{1.17}$$

E is the electron energy, m_e is the electron mass, σ_T is the Thomson cross section, c is the speed of light, B is the magnetic field strength in our galaxy and ω_{ph} is the density of the interstellar photons from star light and the cosmic microwave background for the inverse Compton scattering.

From this equation one can see that electrons will have lost their energy after $T = \frac{1}{bE}$. From [119] the energy-loss coefficient can be estimated to $b \approx 2 \times 10^{-16}\,\mathrm{GeV}^{-1}\,\mathrm{s}^{-1}$ for the TeV regime and therefore that the mean free time T, the average time between collisions with other particles, is $T \approx 2.5 \times 10^5\,\mathrm{years/E(TeV)}$. Assuming that the electron is traveling at the speed of light, the mean free path is of the order of a few kpc. The electrons reaching Earth must originate within the galaxy.

The theoretical model for the energy spectrum is governed by two terms: One describing losses, the other describing the injection of accelerated electrons. The possible sources will be described in the section 1.3. Positrons only contribute in the percent-regime to the total flux of electrons and positrons, even though their contribution is rising for high energy.

The change of the electron energy spectrum over time is then governed by a diffusion loss equation:

$$\frac{dN(E)}{dt} = D\nabla^2 N(E) + \frac{\partial}{\partial E}\left[b(E)\,N(E)\right] + Q(E). \tag{1.18}$$

$D\nabla^2 N(E)$ is the diffusion term describing the random scattering due to irregularities in the magnetic field. $\frac{\partial}{\partial E}\left[b(E)\,N(E)\right]$ are the energy losses described in 1.16 and $Q(E)$ is the source term.

The mean free time is short in comparison to the total age of our galaxy. It can therefore be assumed that the spectrum has reached a steady state under continuous injection from sources and the previously described energy losses. In this simplest approach, the diffusion term can be neglected as it will contribute very little and Eq. 1.18 can be simplified to:

$$\frac{d}{dE}\left[b(E)\,N(E)\right] = -Q(E). \tag{1.19}$$

Where $Q(E)$ is the injection spectrum of form κE^{-p} and the energy losses, as defined in Eq. 1.17, are $b(E) = -\frac{dE}{dt}$ for the energy range of this thesis. Setting the limit of $N(E) \to 0$ for $E \to \infty$, Eq. 1.19 can be integrated to give:

$$N(E) = \frac{\kappa E^{-(p-1)}}{(p-1)\,b(E)}. \tag{1.20}$$

Using $b(E) \propto E^2$ one can conclude from Eq. 1.17 that

$$N(E) \propto E^{-(p+1)}. \tag{1.21}$$

So the observed electron energy spectrum is one power of E steeper than the original injection spectrum. This is in line with the expected spectral index of ~ -2 for the flux of cosmic electrons emitted by SNR and the observed spectral index of ~ -3 on Earth.

1.2.1. Anisotropy

However, 1.18 is not a true equilibrium. As the range for the very-high-energy electrons and positrons is very limited, only a small subsample of galactic sources can possibly contribute to the TeV-flux observed at Earth.

This has several consequences: firstly, the individual sources will leave unique features in the energy density spectrum and, as their contribution decreases, the flux will return to that of secondary electrons and positrons due to the lack of very close-by accelerators. Secondly, the flux is not actually going to be homogeneous in time or space. The spectrum will change with time as close-by sources die out or a new ones appear. Currently, the temporal inhomogeneity is negligible as the time scales involved are much larger than the very young field of particle astrophysics and measurement of the cosmic electrons and positrons only go back about fifty years as detailed in section 1.1.5.

The spatial anisotropy could be measurable, as the individual sources are close enough to cause inhomogeneities. It can be quantified as follows[165]

$$\delta_i := \frac{I_{max} - I_{min}}{I_{max} + I_{min}}. \tag{1.22}$$

δ_i quantifies the anisotropy in the electron flux, I_{min} and I_{max} are the minimum and maximum intensity of electron emission of a source. It can also be expressed in function of the source contribution of electrons N_i:

$$\delta_i = \frac{3D}{c} \frac{\nabla N_i}{N_i} = \frac{3r_i}{2ct_i}. \tag{1.23}$$

$N_i(E, r_i, t_i)$ is a function of the energy, the distance r_i and the age of the source t_i and D is the diffusion coefficient, both are model-dependent characteristics of the source. Kobayashi showed, that for the most dominant source at TeV energies, Vela, the theoretical anisotropy is maximal at 13% with an assumed age of 11×10^3 yr and at a distance of 300 pc[119]. This fluctuation is lower than the total uncertainties affecting this analysis which will be given in chapter 5. Therefore the measured flux can be assumed to be homogeneous for this analysis and any observed difference must have a different origin.

Additionally, Fermi-LAT published a study of the electron flux anisotropy in 2012[23] limiting the anisotropy at 1 TeV to about 1%,. This puts some loose constraints onto local sources in the galaxy, in particular it supersedes the theoretical motivated maximal anisotropy of the previous paragraph. But the experimental result does not rule out any particular source due to the wide parameter space available in modeling the individual sources[55]. A similar study was performed by PAMELA for just the positrons from 10 GeV

to 200 GeV[31]. They find no indication of an anisotropy, but the upper limits are still above those predicted by astrophysical sources.

1.3. Origin of cosmic electrons and positrons

Recent measurements have revealed unexpected features atop of the expected spectrum of secondary electrons and positrons and primaries from SNR. The basic assumed flux consists of secondary electrons and positrons, modeled as the result of charged pions and kaons decays[172], as well as the primary electrons from SNR acceleration. The focus of this section will be the source-candidates explaining the unexpected excess over the secondary flux of electrons and positrons. The observed features in the all electron spectrum measured so far are ranging from a general overabundance of high-energetic electrons and positrons confirmed by many experiments[21, 30, 34] to a bump at 600 GeV only seen by ATIC[73]. They all disagree with the assumption of a flux consisting solely of primary electrons from SNR and secondary electrons and positrons.

The origins of these features are still under debate, the most accepted interpretations being either related to Dark Matter (DM) or astrophysical sources such as nearby pulsars or SNR[90]. DM theories explaining the electron surplus are heavily constrained by the positron and anti-proton ratio measurements of PAMELA and AMS-02[27, 28, 33], as DM would have to decay only leptonically to explain the raise in the positron ratio and the possible lack of a rise in the anti-proton ratio as mentioned in 1.1.6.

There are four possibilities for the origin of high energetic electrons and positrons in current literature:

- Acceleration in shocks and magnetic turbulences. High-energy electrons and positrons can either be accelerated directly, or other cosmic rays are accelerated and generate high-energy secondary electrons and positrons. The acceleration mechanism is the diffuse shock acceleration, discussed in 1.1.3.
- Annihilation of high energy γ-rays with background photons, which will be covered in section 1.3.1.
- Pair production in strong magnetic fields is covered in section 1.3.2.
- Annihilation or decay of DM particles will be addressed in the last section, 1.3.3.

The first part of this section will define the basic flux of secondary electrons and positrons. The secondary electrons and positrons, in addition to the primary electrons coming from the diffuse shock acceleration in SNR that was already discussed in section 1.1.3 form the background. The second and third part will then focus on the possible astrophysical and Dark Matter sources for the observed excess of very-high-energy electrons and positrons over the expected flux of secondaries.

1.3.1. Secondary electrons and positrons

In the previous section, 1.2, the energy losses of cosmic electrons and positrons were discussed in detail. This type of losses is not unique to electrons and positrons, they also

a ect all other cosmic rays. This in turn generates secondary electrons and positrons, in particular from spallation. However, due to the charge asymmetry of the cosmic ray, spallation generates primarily positrons[83, 118]:

$$\begin{aligned} p + p \to \pi^{\pm} X, \quad \pi^{\pm} \to \mu^{\pm} \overset{(-)}{\nu_e}, \quad \mu^{\pm} \to e^{\pm} \overset{(-)}{\nu_e} \overset{(-)}{\nu_\mu} \\ p + p \to \pi^{0} X, \quad \pi^{0} \to 2\gamma, \qquad \gamma \to e^{+}\, e^{-} \end{aligned} \tag{1.24}$$

The resulting e^+ and e^- secondaries from a proton flux with a spectral index of -2.7 with a cut o at 512 TeV can be seen in Fig. 1.7. The plot shows the simulated distribution of secondary electrons and positrons generated by pion decays from p-p collisions, illustrating that the secondary production will generate more positrons than electrons.

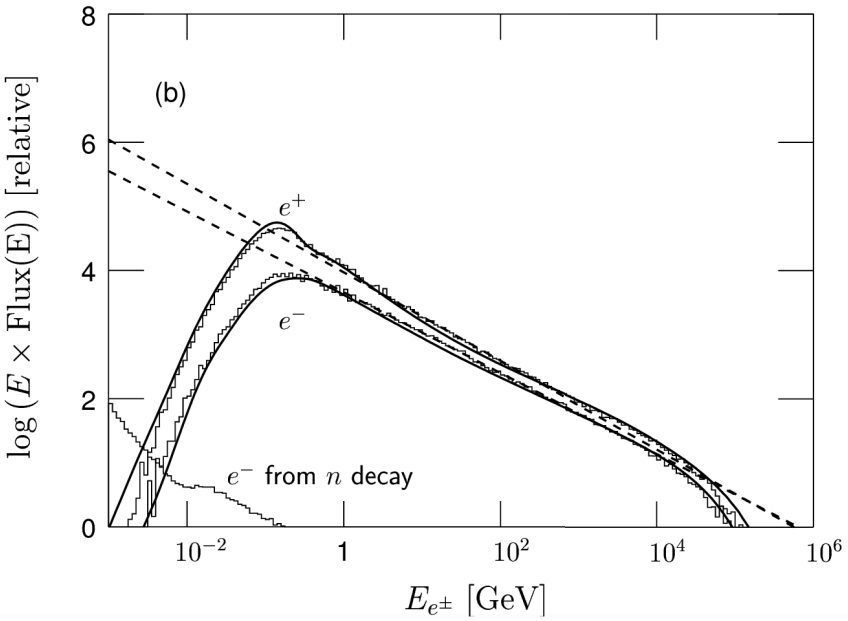

Figure 1.7: $e^{\pm}$ secondaries from an injected proton flux. Taken from[118]. More details in the text

These secondaries are truly homogeneous as the nucelonic cosmic rays reach Earth from much further away than electrons and positrons.The previously discussed constraints do not hold true here. The propagation and di usion equation can only rarely be solved analytically[51], in most cases numerical modeling is used. The best known code is GALactic PROPagation (GALPROP)[1] developed by Moskalenko and Strong[138, 171]. The injection spectrum and spatial distribution of the sources is used as input from which the fragmentation and energy losses of cosmic rays are calculated to finally produce the resulting cosmic ray spectra observed on Earth. For the electrons the primary source are assumed to be SNR. This, in addition to secondary production of electrons and positrons, is the model used in the GalProp simulation as the background of known electrons and positrons. The origin of the excess to this background will be discussed in the next part,

[1] http://galprop.stanford.edu

the flux of the different components of this background can be parameterized as follows[51]:

$$\frac{d\Phi}{dE}_{e^-,\text{prim}} = \frac{0.16\epsilon^{-1.1}}{1+11\epsilon^{0.9}+3.2\epsilon^{2.15}}\,\text{GeV}^{-1}\,\text{cm}^{-2}\,\text{s}^{-1}\,\text{sr}^{-1}, \tag{1.25}$$

$$\frac{d\Phi}{dE}_{e^-,\text{sec}} = \frac{0.7\epsilon^{0.7}}{1+110\epsilon^{1.9}+580\epsilon^{4.2}}\,\text{GeV}^{-1}\,\text{cm}^{-2}\,\text{s}^{-1}\,\text{sr}^{-1},$$

$$\frac{d\Phi}{dE}_{e^+,\text{sec}} = \frac{4.5\epsilon^{0.7}}{1+650\epsilon^{2.3}+1500\epsilon^{4.2}}\,\text{GeV}^{-1}\,\text{cm}^{-2}\,\text{s}^{-1}\,\text{sr}^{-1} \tag{1.26}$$

where $\epsilon = \frac{E}{1\,\text{GeV}}$. For $\epsilon \gg 1$ the dominant contribution are the primary electrons, this means that the ratio of positrons to electrons should decrease with increasing energies. However, this is not the case, as has been well documented[14, 17, 28].

1.3.2. Astrophysical sources

The majority of primary electrons are assumed to come from astrophysical sources, in particular super nova remnant (SNR). However, the current model is still very basic. It is possible that there are other effects not yet accounted for, which would allow SNR to also be candidates for explaining the excess of very-high-energy electrons and positrons. In addition a very promising candidate are pulsars, as will be shown in the second part.

Supernova Remnants

SNR are a canonical source of cosmic rays and are already considered to be among the main sources of cosmic electrons and positrons. But current modeling relies on an isotropic distribution of sources and could be overly simplified for the special case of electrons and positrons [21, 30, 34]..

Inhomogeneity: The distribution of SNRs is assumed to be homogeneous, which is valid for long range cosmic rays. However, electrons and positrons above 100 GeV can only originate from within a radius of ~ 1 kpc. Within that small radius the SNR distribution can be inhomogeneous, which would lead to an altered electrons and positrons spectrum by up to 10%[119].

Secondaries in SNR: In most scenarios, it is assumed that SNR are primary sources for electrons and protons, but positrons are only produced as secondaries.

Acceleration of secondary particles is usually neglected as the probability of an interaction at the source is an order of magnitude lower than an interaction while traveling through the diffusive halo. But allowing for secondary production in the same region where primary acceleration takes place, one can achieve growing secondary/primary ratios, compatible with current measurements of the positron fraction[164]. The collisions in the acceleration region are primarily proton-proton. The resulting $e^{\pm}$ are reaccelerated repeatedly as the region from which particles can return to the shock and get reaccelerated increases with energy. This allows, naturally, for an increasing positron ratio, which levels out at about 40-50%[63] explaining the positron fraction and the very-high-energy electrons and positrons excess.

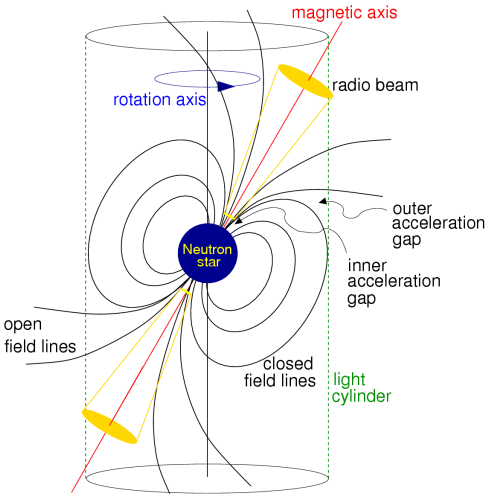

(a) Simple model of a pulsar showing the rotation axis and the magnetic axis taken from [128].

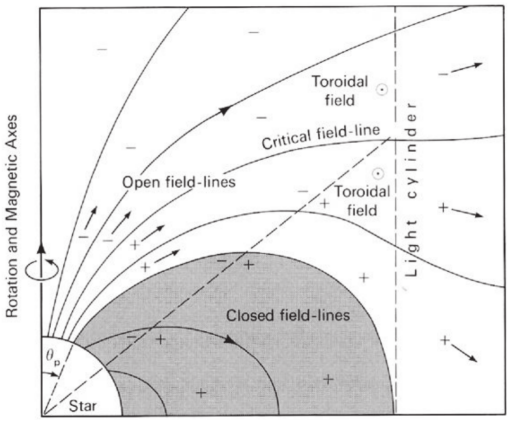

(b) Illustration of the magnetosphere and its charge distributions. Taken from [126].

Figure 1.8: Illustrations of a pulsar.

Pulsars

Pulsars are strongly magnetized, rapidly rotating neutron stars emitting broad-band pulsed electromagnetic radiation[150] created by the supernova of a massive star (1.5 $M_\odot$– 5 $M_\odot$). They can be considered as a rotating, non-aligned magnet with a strong magnetic dipole moment. They usually have very strong magnetic fields of the order of 10^{10} G to 10^{14} G. They are important accelerators and their emission covers almost the entire range of the electromagnetic spectrum from radio to VHE γ-rays[126].

Fig. 1.8a shows the basic built of a pulsar, with a rotating neutron star at the center, surrounded by the so-called magnetosphere. In the simplest approximation, the neutron star can be taken to be a perfectly conducting sphere with a magnetic dipole moment p_0, rotating at a frequency Ω in vacuum[100, 150].

However, Goldreich and Julian showed, that strong radial electric fields appear at the surface of the neutron star, of the order of:

$$E \approx \Omega R B_0 \approx 6 \times 10^{12} P^{-1}\,\mathrm{V\,m^{-1}}. \tag{1.27}$$

Where $B_0 = 10^8$ T is the magnetic flux density, R is the radius of the neutron star and P is the period of the pulsar in seconds[101]. This implies that the electromagnetic force exceeds the gravitational force which will generate a plasma of charged particles around the neutron star. This is known as the Goldreich-Julian magnetosphere.

A, possibly unique, feature of the magnetosphere is that it is a charge-separated plasma. The net field in the plasma is $\mathbf{E} + (\mathbf{v} \times \mathbf{B}) = 0$, as the induced electric field is neutralized by the flow of the charges in the plasma. This means the spacial distribution of particles

can be found from Maxwell's equation $\nabla \cdot E = \frac{\rho_e}{\epsilon_0}$, where ρ_e is the charge density[126]:

$$\rho_e = \epsilon_0 \nabla \cdot \mathbf{E} = \epsilon_0 B_0 \left(\frac{R^3}{r^3} \right) (1 - 3\cos^2\theta). \tag{1.28}$$

r is the distance to the neutron star and θ is the angle to the magnetic field line. This leads to the plasma being divided along the so-called "null surface"[175] where the charge density changes sign.

The plasma extends outwards up to the corotation radius, which is defined as $r_c = \frac{c}{\Omega}$, inside corotating particles have a speed smaller or equal to the speed of light. It is also called light-cylinder. Field lines contained within the light cylinder are closed and the particles corotate with the neutron star. Magnetic field lines cutting the light cylinder allow for escape of charged particles. The critical field line is, then, the field line at which the charge inversion for escaping particles takes place. Fig. 1.8b shows the charge distribution and inner workings of the magnetosphere.

All models for particle acceleration are based on electric fields which have a non-vanishing parallel component to the magnetic field: $\mathbf{E} \cdot \mathbf{B} \neq 0$. Normally the plasma would screen the electric field, such that $E_{||} \approx 0$. However, there are charge-depleted areas in which the plasma can not screen the electric field.

In these areas a charged particle will either be accelerated towards to, or away from, the neutron star. The particle accelerating away from the neutron star, will be sent on a curved line. Therefore emitting curvature radiation in form of very-high-energy γ-rays. This initiates an electro-magnetic cascade, creating many high energy electron-positron pairs capable of escaping the magnetosphere.

The three main regions of acceleration according to the literature are:

- The polar cap model[174], which has a charge depleted area at the polar cap, where the plasma escapes along the open field line. This creates a strong electric differential of up to 10^{13} V.

  The polar cap model is currently under a lot of investigation, as the observed pulsar very-high-energy γ-spectra are hard to reconcile with this model[8, 154]. It is particularly hard to describe behavior of young pulsars, such as the double-peak light curve observed in the Crab pulsar.

  It is, however, a model that accelerates particles very effectively, even if it may not be the dominant contribution of the observed γ-ray flux.

- The slot gap model[46, 141], which is an extension of the polar cap model. It extends the region in which the particles are accelerated further out in the magnetosphere, extending the vacuum up to the light cylinder. It has been shown that electrons and positrons can be accelerated up to Lorentz factors of $\gamma = 10^7$[141]. It was originally developed to explain the double-peaked nature of the Crab light curve. It has, however, other problems, in particular the justification of a constant $E_{||}$ at high latitudes seems not physically motivated[109].

- The outer gap model[76], which is the currently favored model for very-high-energy γ-ray emission, as it fits observational results for young pulsars, like Crab, the best.

It assumes a vacuum gap forming along the last open field line, in vicinity of the null charge surface. The density is assumed to be zero at the null surface, therefore a strong $E_{||}$ component is expected to exist, which will accelerate charged particles.

As with the previous models, there are some theoretical issues. In particular a large width of the gap has to be assumed to be able to reproduce the luminosity observed for the Crab pulsar.

Pulsar physics are still heavily under development and not a lot is known for sure. While currently favored model for the very-high-energy γ-ray emission is the outer gap, the polar cap is the favored location for particle acceleration, in particular $e^{\pm}$ pairs, as well as radio emission. Currently hybrid models suggesting emission from multiple regions for different energy bands are the preferred interpretation[155].

The γ-rays created in the gaps of a pulsar can interact with the background photon field and produce $e^{\pm}$ pairs which can be re-accelerated outside the magnetosphere by shocks from pulsar winds. Several calculations of the pulsar energy and the fraction of it emitted in radiation for nearby pulsars lead to results which are in general accordance with the $e^{\pm}$ excess flux[156, 157]. In addition this would give an increase in the positron ratio without doing the same for the anti-proton ratio, as the main production mechanism is based on pair-production of electron-positron pairs.

1.3.3. Dark Matter

Dark Matter has been a strongly debated topic over the last eighty years. It was first proposed by Fritz Zwicky[191] who inferred the mass of the Coma cluster both from the luminosity and from the dispersion velocities of the galaxies and found a significant mismatch between the two. The same observation has been made in galaxies. Especially the measurement of the rotational speed in galaxies is a core argument in favor of Dark Matter[161]. Today Dark Matter is part of the Standard cosmological model Λ-CDM and is expected to compose roughly 25% of all energy in the universe, about five times the amount baryonic matter does. However, little is known about Dark Matter itself and it has not yet been detected directly.

A Dark Matter candidate has to fulfill a number of criteria: it needs to be non-baryonic and not interact electro-magnetically. It has to interact gravitationally, it may also interact weakly. It must be stable or have a lifetime comparable to the age of the universe.

A popular Dark Matter candidate is the weakly interacting massive particle (WIMP). WIMPs are a thermal relic, meaning they were in equilibrium with the primordial plasma. When the temperature T dropped below the WIMP-mass m_χ their production ceased and the number of WIMPs started to decrease exponentially with $e^{-\frac{m_\chi}{T}}$. As the universe continued to expand, the gas of WIMPs became so diluted that they could no longer annihilate. The WIMP-density froze-out and asymptotically reached a constant density[58]:

$$\Omega_\chi h^2 \approx \frac{10^{-27}\,\mathrm{cm}^3\,\mathrm{s}^{-1}}{\langle \sigma_{ann} v \rangle}. \tag{1.29}$$

Ω_χ is the WIMP density parameter, h is the Hubble constant, $\langle \sigma_{ann} v \rangle$ refers to the thermally averaged product of the annihilation cross section and velocity.

Entering the expanding Dark Matter density in Eq. 1.29 returns an annihilation cross section $\sim 10^{-26}\,\mathrm{cm}^3\,\mathrm{s}^{-1}$, which is the scale of the weak interaction. The fact that the weak scale gives the right matter density is often referred to as the "WIMP miracle".

Interpreting the surplus of very-high-energy electrons and positrons in terms of Dark Matter is a popular field of study and many attempts have been made[50, 54, 67, 78, 91, 112]. It has become challenging and very constrained due to the measured increase in the positron ratio and the lack of increase in the anti-proton ratio as measured by PAMELA[27, 28] and AMS-02[1, 33], as well as the constraints on the annihilation cross-section from γ-ray observations of dwarf satellites[10, 24, 43, 44].

Finally, strong constraints come from implications of the CMB measurements[79, 97, 167] and, for high DM masses, from the IceCube observatory[2]. Dark Matter is mentioned here for completeness, but astrophysical sources are much favored as the source of the electron or positron excess.

Annihilating Dark Matter

In many DM models Dark Matter particles are their own anti-particles and can annihilate with each other. There are several possible annihilation scenarios:

- DM particles annihilate to particle pairs like gauge bosons, quarks or leptons, most of which would decay further. Direct annihilation into $e^{\pm}$ could account for the steep peak ATIC measured[78].
- DM particles annihilate via virtual internal bremsstrahlung. This would produce γ, e^+ and e^- in equal amounts[54].
- DM particles annihilate to pairs of new mediating particles. These mediating particle pairs would consequently decay into Standard Model particles. This scenario would allow to model a smooth increase in the $e^{\pm}$ flux whereas the other models would produce peak-like features.[50]

All DM models are heavily constrained by other measurements. For example a popular extension to the Standard Model is Supersymmetry. The minimal supersymmetric model contains four neutralinos, fermions which are electrically neutral. The lightest of these particles is stable and is a natural DM candidate. It can give rise to the positron excess. But it has a large hadronic annihilation fraction, so an increase in the anti-proton ratio should be observed, which has not been observed by experiments[27].

A possible scenario circumventing this would be to introduce an additional gauge singlet superfield. If the lightest neutralino has a significant singlet component, it can decouple from the Standard Model. As a DM candidate it could annihilate to a light singlet-like Higgs boson which then decays into $e^{\pm}$ or $\mu^{\pm}$[50]. The mass of this boson is lower than twice the mass of a b-quark, which suppresses the decay into non-leptonic end states.

Decaying Dark Matter

Theoretically, Dark Matter does not have to be stable, it only needs a lifetime longer than the age of the universe. Fermi-LAT constrained the life time to a lower limit of 10^{25}

seconds[112]. In models where DM is not stable, the decay products might explain the $e^{\pm}$ surplus. In order to account for the excess in the positron ratio without an increase of the anti-proton ratio, the decay would have to be mainly leptonic and hadronic branching ratios must be suppressed.

Some of the most common candidates for such a decaying DM particle would be gravitinos[75], hidden gauge bosons[74], or R-parity breaking scenarios where the hadronic decays are surpressed[75]. Many of these particles would, in addition, solve some of the other cosmological riddles, such as the observed abundance of primordial elements, the relic DM abundance or the baryon asymmetry. However, for a lot of these models more recent measurements are making an DM interpretation of the positron excess increasingly challenging. Some have been completely ruled out due to new constraints, such as the gravitino DM[71].

While the decay model is not as popular as the annihilation model, it has some advantages. For one, given the freedom of choosing the life time of the DM particle, no boost factor is needed. In addition it suffers much less constraints from gamma-ray and radio observations, as the decay flux of γ-rays is only proportional to the DM density in the halo ρ, not ρ^2[91]. Hence ,the lack of a signal from the center of our galaxy[9] poses less of a constraint on the decay models, since the expected signal here would be much weaker.

Dark Matter and astrophysical sources

All Dark Matter models are heavily constrained by measurements from γ-ray observations[127]. Indeed a recent scan of the parameter space for DM candidates explaining the positron ratio rise observed by AMS-02 found no viable model to explain the rise entirely with DM and still remain compatible with the restrictions from the upper limits on the cross sections from γ-ray observations[67]. At the same time, pulsars have been established as electron-positron emitters. Recently investigation of models comprising both astrophysical and DM sources became popular, especially since the indirect evidence for Dark Matter is continuously increasing. Indeed diMauro[131] showed that the fit of a mix of astrophysical sources and DM show a better match to the experimental data, than the pure astrophysical origin.

The interpretation and modeling of the electron spectrum remains a hotly debated topic and many different interpretations remain viable. Future high precision measurements will allow to tip the scale in favor of a specific model, which one this will be remains to be seen.

2. The imaging atmospheric Cherenkov technique

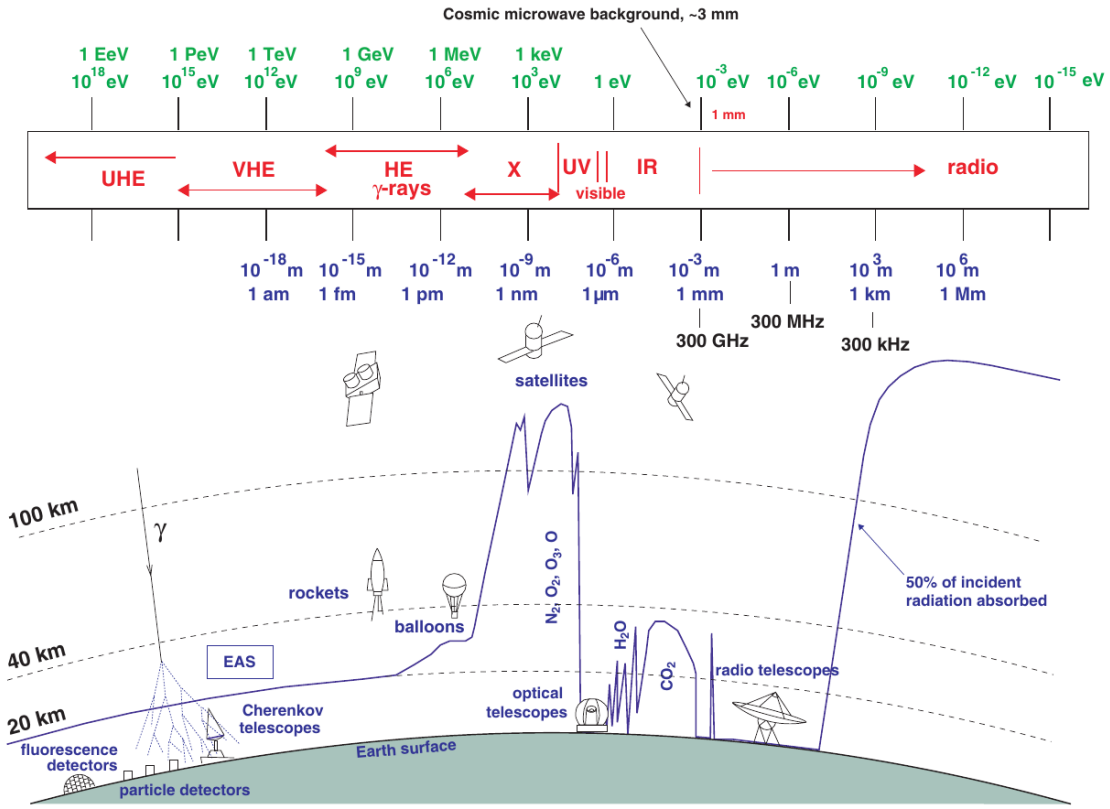

Figure 2.1: Atmospheric windows for the observation of the universe taken from [184]. The continuous line indicates the height at which half of the total incoming electromagnetic radiation is absorbed by the atmosphere.

The field of astroparticle physics is a relatively young field, focusing primarily on high-energy (>100 MeV) cosmic rays depicted in Fig. 2.1. Different energy bands are covered by different type of detectors from large radio telescopes to satellite. It faces a couple of challenges: The cosmic-ray flux follows a steep power law. At the same time, Earth's atmosphere becomes opaque to the incoming cosmic rays above 1 keV. Figure 2.1 illustrates this for the case of γ-rays. The blue line shows the height at which 50% of the γ-rays of said energy are absorbed.

As can be seen, the absorption varies with the energy. The atmosphere becomes opaque above a few GeV. This is true for all types of cosmic rays. When the atmosphere becomes

opaque, γ-rays can be detected from space using space-borne telescopes.However, due to their small effective areas, space-borne telescopes lack sensitivity for higher energies, where the gamma flux is much lower. The only remaining option is to use indirect measurements from the ground. The Imaging Atmospheric Cherenkov Technique (IACT) employed by MAGIC makes use of this opacity for very-high-energy particles by registering Cherenkov light. The light is generated from the extensive air shower (EAS) caused by the interaction of the incoming particle and the molecules of the atmosphere. In the first section of this chapter, 2.1, the physical processes involved in the development of an EAS will be summarized, and an overview of the IACT will be presented in 2.1.5.
In section 2.2, the MAGIC telescopes used for the work presented in this thesis, will be described. Followed by the data-taking procedure and analysis framework in 2.3 and 2.4. Finally the challenges of the diffuse analysis described in chapter 3 will be highlighted in section 2.5.

2.1. Extensive air showers

An EAS is a cascade of secondary particles initiated by a very-high-energy cosmic ray interacting with molecules in the upper atmosphere. The produced secondary particles have a speed greater than the speed of light in the atmosphere and therefore produce Cherenkov light, which is collected by the IACT. The primary particle strongly influences the characteristics and development of the shower. Therefore, collection of the Cherenkov light on the ground enables the IACT to reconstruct the characteristics of the shower and thereby characterize the primary particle. A brief qualitative description of the emission of Cherenkov light and the shower propagation will be given in this section, followed by the description of how the IACT uses emitted Cherenkov light to reconstruct the properties of the incoming cosmic ray.

2.1.1. The atmosphere as a detector

In the IACT the entire atmosphere is part of the detector. The cosmic ray penetrates into the atmosphere and interacts with the nuclei present in the upper layers. The Cherenkov light generated by particles in the atmosphere is the collected signal. A brief description of EAS in the atmosphere will be given here, for more detailed information see [88].

The atmosphere is usually characterized by its slant depth. This is a measure of the amount of matter a particle encounters on its path through the atmosphere, and is usually given in $\mathrm{g\,cm^{-2}}$ or $\mathrm{kg\,m^{-2}}$. If the path of the shower is vertical through the atmosphere the slant depth is the integral of the atmospheric density $\rho(h)$ along the height h:

$$X(h_0) = \int_{h_0}^{\inf} \rho(h)\mathrm{d}h. \tag{2.1}$$

The atmospheric density can be expressed using the barometric formula for an isothermal atmosphere $\rho(h) \approx \rho_0 \exp\left(-\frac{h}{h_0}\right)$. ρ_0 is the ground density $\approx 1.2\,\mathrm{kg\,m^{-3}}$ and h_0 is called

scale height and is roughly $\approx 8600\,\mathrm{m}$[65]. From this the slant depth can be approximated to $X(h) \approx 10300 \exp\left(-\frac{h}{h_0}\right) \mathrm{kg\,m^{-2}}$.

The refraction index can be approximated in the same way:

$$n(h) \approx 1 + \eta_0 \exp\left(-\frac{h}{h_0}\right), \tag{2.2}$$

where $\eta_0 + 1$ is the refraction index at sea level: 1.00029.

As discussed in section 2.1.4 any charged particle moving faster than the speed of light in the matter will emit Cherenkov light. The EAS consists of a primary particle inducing a cascade of new particles. These particles are still very energetic and emit Cherenkov as well. This creates layers of rings of Cherenkov light on the ground due to the varying Cherenkov angle with the height.

In general terms, EAS can be described with a set of coupled differential equations, for every particle species i[159]:

$$\frac{\mathrm{d}N_i(E,X)}{\mathrm{d}X} = -\left(\frac{1}{\lambda} + \frac{1}{d_i}\right) N_i(E,X) + \sum_j \int \frac{F_{ji}(E,E_j)}{E} \frac{N_j(E_j)}{\lambda_j} \mathrm{d}E_j \tag{2.3}$$

where:

- X is the slant depth.
- E is the particle energy.
- $N_i(E,X)$ is the number of particles of type i and energy E at a depth X.
- λ_i is the interaction length for particle type i.
- d_i is the decay length.
- $F_{ji}(E,E_j)$ the cross section for particle type i with energy E colliding and producing a particle of type j with energy E_j.

The right hand side consists of two terms: The first describes particle absorption and decay and the second particle creation. Further corrections such as the geomagnetic field, energy losses of secondary particles or light pollution are not taken into account in 2.3. If one tries to include those corrections, the limits of what is possible with analytical calculations is quickly reached. Therefore, most experiments resort to Monte Carlo (MC) simulations, which will be described in more detail in section 3.1.3.

For the IACT one differentiates between two types of showers in particular: Electromagnetic and hadronic showers, both are shown in Fig. 2.2.

2.1.2. Electromagnetic showers

When a γ-ray, electron or positron enters the Earth's atmosphere, an electromagnetic shower is initiated by the interaction with the atmospheric molecules. If the penetrating particle is a γ-ray, its first interaction will be an electron-positron pair created in the Coulomb field of a nucleus. If the primary particle is an electron or positron, its first

interaction will be the emission of a photon through bremsstrahlung also in the Coulomb field of an air nucleus. These are the only two major interactions taking place in an electromagnetic shower. Theoretically, the photon can also create pairs of other particles besides $e^{\pm}$, but in this context, it is negligible.
The radiation length X_0 defines the distance which a particle needs to travel to reduce its energy to $\frac{1}{e}$:

$$\frac{\mathrm{d}E}{\mathrm{d}x} = -\frac{E}{X_0}. \tag{2.4}$$

The radiation length of bremsstrahlung for electrons, X_0^e in air, depends on the molecules in the air and was calculated as $X_0^e = 36.664\,\mathrm{g\,cm^{-2}}$[179]. For pair creation the mean free path is somewhat larger, so the radiation length for a high-energetic γ is[116]:

$$X_0^\lambda = \frac{9}{7} X_0^e. \tag{2.5}$$

The difference between the two radiation lengths is also the only major difference between showers initiated by γ-rays and and $e^{\pm}$, making a differentiation impossible with the current experimental setups described in section 2.2.

The particles produced in the shower move with relativistic velocities and continuously interact either by bremsstrahlung or by pair production. During the development of the cascade the average energy of shower particles decreases exponentially until the critical energy $E_c \sim 80\,\mathrm{MeV}$ is reached. Below this energy other processes start to dominate, such as ionization of atoms[180] and no new particles are produced. The shower development stops.

A simplified scenario of such a shower is provided by the Heitler model[104], which assumes that the particles interact after one radiation length, labeled as $\lambda_e = X_0^e$, producing two secondary particles with energy $\frac{E}{2}$. Thus the number of particles at each level of the shower increases by a factor of two and the average energy of each particle is:

$$E_n = \frac{E_0}{2^n}. \tag{2.6}$$

n is the level of the shower as seen in Fig. 2.2 and E_0 is the energy of the incoming cosmic ray. This model allows for a simple estimation of the maximum penetration of the shower. The lowest level of the shower is reached when particles have an energy similar to E_c defined in Eq. 2.6:

$$n_c = \frac{\ln \frac{E_0}{E_c}}{\ln 2} \quad ; \quad X_{max} = \lambda_e n_c. \tag{2.7}$$

n_c is the number of levels in the shower. Heitler himself already noted the overly simplified character of his model. It will overestimate the amount of electrons and positrons with respect to the γ. Nevertheless, the prediction for the shower height is reasonable. More detailed analytical derivations exist, e.g. [160], which take into account the longitudinal development of the shower, describing the aging of the shower.

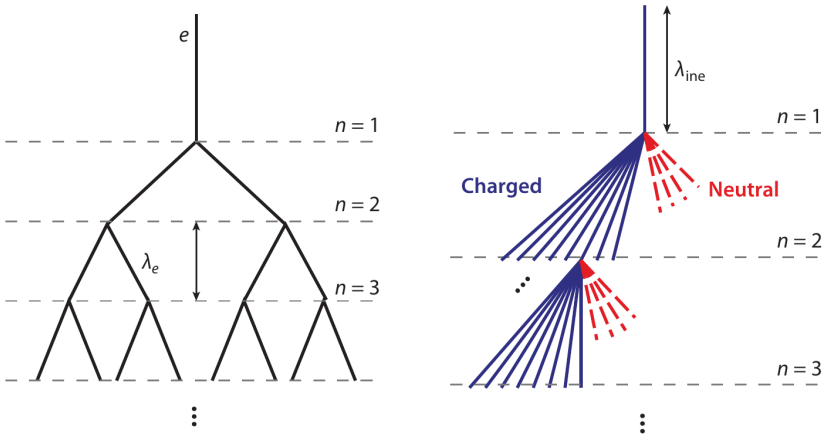

Figure 2.2: Simple model of an air shower. Left an electromagnetic shower. Right the hadronic component of a cosmic ray induced shower. Taken from [88].

2.1.3. Hadronic showers

Hadronic showers produce predominantly mesons in the first interaction, mostly pions, through inelastic scattering off air nuclei. The mean free path for inelastic scattering is roughly $80\,\mathrm{g\,cm^{-2}}$ and therefore larger than the radiation length of electromagnetic showers. Not only are hadronic cosmic rays penetrating deeper into the atmosphere before their first interaction. The full development of the shower maximum lies also deeper in the atmosphere.

In addition, weak and strong interactions in hadronic showers produce large transverse momenta, thereby cause a larger lateral extension of the shower and inducing electromagnetic and muonic sub showers[64]. The more complex processes taking place in hadronic showers cause a more irregular shape of the shower. A simplified picture of a hadronic shower is shown in Fig. 2.2. The aforementioned properties define the differences between hadronic and electromagnetic showers. It is, however, not always possible to clearly distinguish between the two. Electromagnetic subshowers created in a hadronic shower can not be distinguished from the electromagnetic showers initiated by a γ-ray.

2.1.4. Cherenkov light

If the speed of a charged particle in a medium is larger than the speed of light in the medium, Cherenkov light is emitted[77]. For photons with wavelength λ the speed of light in a medium depends on the refraction index $n(\lambda)$ and is given by: $c_m = \frac{c_{vac}}{n(\lambda)}$.

The Cherenkov effect is due to the passage of a charged particle through a dielectric medium. This polarizes the medium locally and it returns into the depolarized state shortly after. Only if the charged particle is traveling faster than the electromagnetic waves induced by the polarization a coherent wavefront is produced, which is known as Cherenkov light. This is illustrated in Fig. 2.4a, where one can see the created wavefront, respective to the moving charge, as well as the cone of emitted Cherenkov light, moving with the speed of light in the medium c_m. One can derive the minimum velocity and

Figure 2.3: Cherenkov light emission and transmission

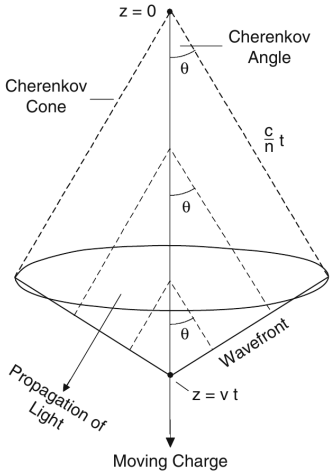

(a) Basic geometry of Cherenkov radiation phenomenon. Shown are the Cherenkov emission angle, θ, of a charged, relativistic particle moving along the z-axis, the instantaneous position of the wavefront and the direction of propagation of the Cherenkov photons. Taken from [103].

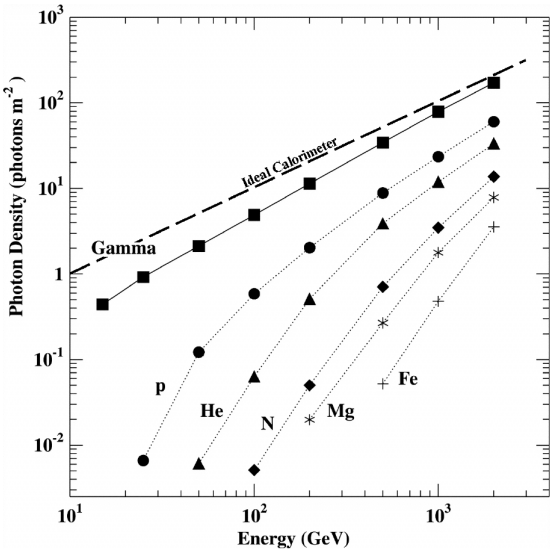

(b) Cherenkov photon density inside the light pool for different particle species integrated over the wavelength range from 300 nm to 550 nm as a function of the energy of the primary particle. For γ-rays the air acts almost like an ideal calorimeter (dashed line). Taken from [147].

minimum energy at which a particle of mass m starts emitting Cherenkov light:

$$\beta_{min}(\lambda) = \frac{1}{n(\lambda)} \quad \text{and} \quad E_{min}(\lambda) = \frac{mc^2}{\sqrt{1-\beta_{min}^2}}. \tag{2.8}$$

Eq. 2.8 shows that light particles are more likely to emit Cherenkov radiation than heavier ones, since their minimum energy is lower.
At sea level the refraction index for air is $n \approx 1.0003$. Using this value to calculate the minimum energy down to which an electron will still emit Cherenkov light, one reaches a value of $E_{min} \approx 21\,\text{MeV}$, For a muon, it is $E_{min} \approx 4.3\,\text{GeV}$[114]. This is already below the threshold at which the shower stops branching out and dies out. So the full shower development can be imaged through the emitted Cherenkov light. Cherenkov light is only produced in a small cone with opening angle θ surrounding the trajectory of the charged particle, see Fig. 2.4a. This angle, also known as Cherenkov angle, is defined by:

$$\cos(\theta(\lambda)) = \frac{1}{\beta n(\lambda)}. \tag{2.9}$$

Since the Cherenkov angle defined in Eq. 2.9 depends on the refraction index, it depends directly on the height as well. It varies from roughly $\sim 0.5°$ at 15 km height to $\sim 1.3°$ at sea level.

EAS were first discovered in 1934 by Cherenkov[77]. The theoretical, classical interpretation was developed by Frank and Tamm a few years later[93]. A more accurate quantum interpretation[98] followed some years later. However for the application of the IACT, the classical approximation yields good results. Using said approach, the number of Cherenkov photons emitted per path length x and wavelength λ by a particle of charge z is given by:

$$\frac{\mathrm{d}^2 N}{\mathrm{d}x\mathrm{d}\lambda} = \frac{2\pi\alpha z^2}{\lambda^2}\left(1 - \frac{1}{\beta^2 n^2}\right) \tag{2.10}$$

where α is the fine structure constant and β is $\frac{v}{c_{vac}}$ as defined in Eq .2.8[146]. The refraction index n is a function of the atmospheric depth as shown in Eq. 2.2, and of the wavelength. The dependency on the wavelength is very small, especially in characteristic wavelength range of atmospheric Cherenkov radiation (300 nm to 600 nm). Therefore, this dependency can be neglected. Eq. 2.10 then becomes directly proportional to the slant depth: $\frac{\mathrm{d}^2 N}{\mathrm{d}x\mathrm{d}\lambda} \propto X$, defined in Eq. 2.1. Integrating over it, one can determine the amount of Cherenkov photons generated in a shower. It follows that a single particle traversing the atmosphere produces about 10^5 Cherenkov photons[103]. However, not all these photons reach the detector. The Cherenkov photons are emitted at a small angle θ, as previously discussed in Eq. 2.9. The emitted photons form a cone, that, on the ground, creates the so called Cherenkov light pool and covers around $50\,000\,\mathrm{m}^2$ on average.

The Cherenkov light yield as a function of the energy of the primary particle is given for different particle types in Fig. 2.4b. For γ -rays, an almost constant fraction of the primary energy is converted into Cherenkov photons. Therefore, a measurement of the Cherenkov light intensity is a good quantifier of the primary γ-ray energy.

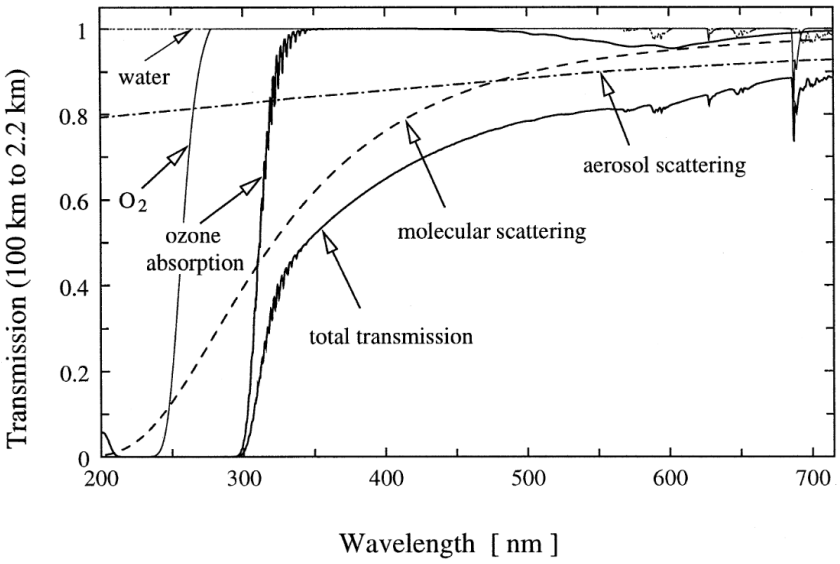

Figure 2.4: Absorption of Cherenkov light along a vertical path down to 2200 m above sea level (asl), the height of the MAGIC telescopes, due to different components of the atmosphere and the remaining transmission. Taken from [56].

Cherenkov photons continuously interact with the atmosphere. Their spectrum is therefore modified, as can be seen in Fig. 2.4: Rayleigh-scattering of air molecules, proportional to λ^{-4} , mainly affects the low end of the spectrum and is the dominant contribution during good atmospheric conditions. Mie-scattering of aerosols, such as desert sand or smoke; water droplets and dust occurs without a much weaker dependence on the photon wavelength (proportional to $\lambda^{-1 \text{ to } -1.5}$). In addition, light with a wavelength below 300 nm is strongly attenuated due to UV absorption by ozone molecules.

The original Cherenkov photon spectrum peaks towards low wavelengths, however, the absorption of smaller wavelengths by the above-mentioned scattering means the Cherenkov light collected on the ground actually peaks around 330 nm, where MAGIC is most sensitive.

2.1.5. Imaging atmospheric Cherenkov technique

The IACT has been used successfully for over 25 years. The forerunner experiment was the Whipple observatory, which detected the Crab Nebula in 1989[186], followed by the HEGRA telescopes[135]. Today, there is a new generation of telescopes using the IACT in operation: MAGIC, H.E.S.S.[35] and VERITAS[110]. With CTA[25], the fourth generation will soon be built.

Blackett was the first to point out that Cherenkov light from an EAS could be detected on the ground[61]. It was first measured in 1953 by Galbraith and Jelley[95]. These were the very first steps leading to the development of the IACT and, in 1989, to the discovery of the Crab Nebula by the Whipple collaboration[186].

In such an imaging Cherenkov telescope, the incoming Cherenkov light is bundled by a large reflector and focused onto the camera plane, which consists of many photo-multiplier tubes (PMTs). The angular distribution is conserved, which helps to distinguish the stage of the shower where the light originally came from, as the Cherenkov angle varies with the refraction index which in turn is a function of the height. This is shown in Fig. 2.5, the light emitted at the top of the shower is at the head of the ellipse. The longitudinal axis of the shower follows the temporal evolution of the shower and points towards its origin. The time gradient in the arrival time of the Cherenkov photons on the mirrors along the longitudinal axis of the ellipse can be used to determine the shower's head. This information is not automatically kept and depends on the layout of the telescope. The dish, reflecting the light towards the camera has to be parabolic to be isochronous. The signal in the PMTs is then used to reconstruct elliptical shower images, which are subsequently parameterized using the Hillas parametrization[106] and shown in Fig. 2.7a. Details on the parametrization will be given in section 2.3.2.

2.2. The MAGIC telescopes

2.2.1. The telescopes

The Major Atmospheric Gamma-Ray Imaging Cherenkov (MAGIC) telescopes are a stereoscopic system of two imaging atmospheric Cherenkov telescopes of 17 m diameter. They are located at the Observatory del Roque de los Muchachos at ~ 2200 m above sea level on the Canary island of La Palma. They were originally designed to have a very low energy threshold (down to ~ 30 GeV) and to reposition very quickly. The goal was to

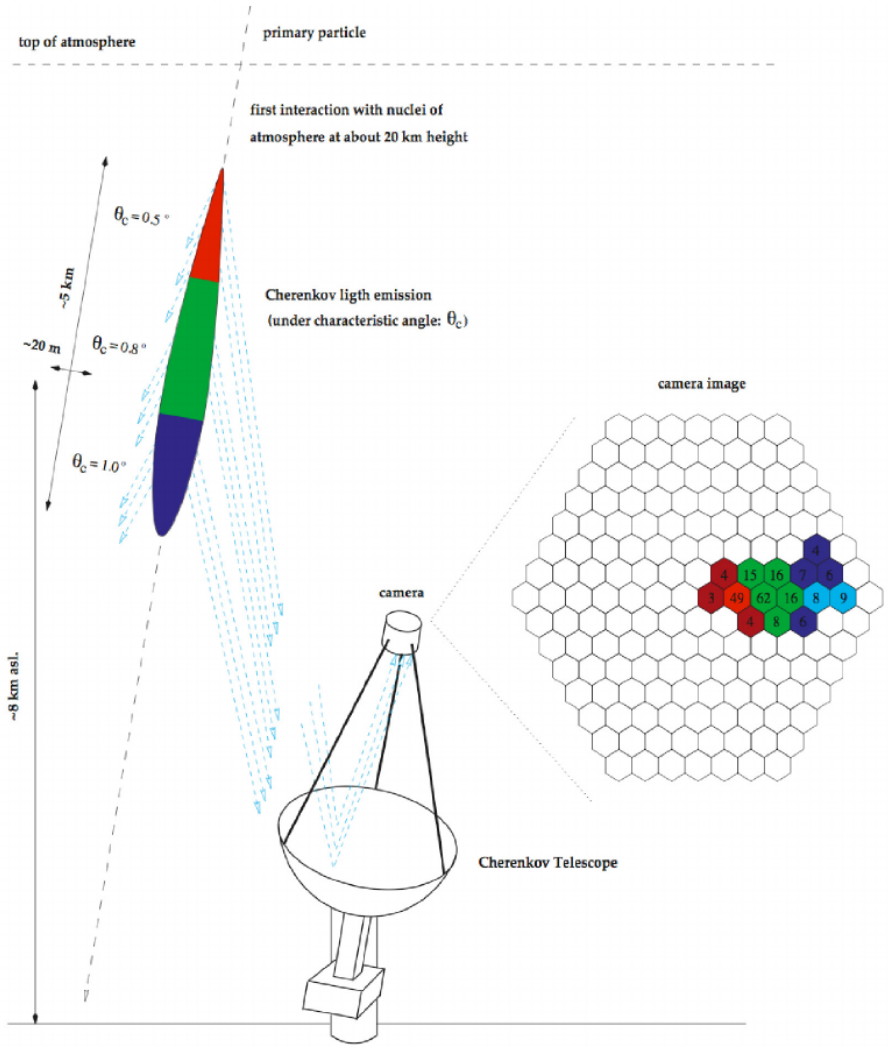

Figure 2.5: Schematic of the IACT: incoming particles initiate a shower. Along the path traveled the Cherenkov angle varies with the depth of the atmosphere. The different colors indicate the head (red), core (green) and tail (blue) of the shower in the atmosphere and the respective projection onto the camera plane. The numbers on the camera represent the number of photons hitting the PMTs. Taken from [183].

discover Gamma Ray Bursts (GRB)s at high energies. GRB last only from a few seconds to a few minutes. The highest γ-ray observed from a GRB so far has an energy of less than 100 GeV[20]. Originally, only one telescope was built in 2003 (referred to as Magic-1 or M1). In 2009 a second telescope, M2, was added. Since then the telescopes have been operating in stereo mode.

Each telescope consists of a lightweight frame structure, allowing quick repositioning, holding the dish and the camera. The dish consists of 247 individual mirrors, aligned as a large parabolic dish. It creates an isochronous surface, allowing conservation of the photon's arrival time on the camera plane. This reduces the time window in which a shower reaches the camera plane and, thereby, reduces background contamination and image reconstruction. The reflector is affected by several aberrations, in particular spherical aberration, which smear the point spread function. To minimize the effect, an active mirror control is in place, which allows to focus each mirror individually onto a corresponding PMT after each repositioning. The camera consists of PMTs with high quantum efficiency and a fast read-out system. Due to the experience gained during the operation of M1, several modifications were made to the design of M2. Thus from 2009 to 2011, which is the data-taking period of this thesis, the two telescope cameras, triggers and read-out systems where different, while the remaining subsystems were for all practical purposes identical.

M1

From 2003 to 2012, the camera of M1 consisted of 577 pixels of two different sizes forming a hexagonal shape[99]. The inner part of the camera was equipped with 396 PMTs with a Field of View (FoV) of 0.1° each, while the outer part consisted of 180 PMTs with a FoV of 0.2°. The total FoV of the camera was 3.5°, but not the entire region could be used to trigger the read-out system. The trigger region consisted of the inner part of the camera, with a diameter of about 1° and did not include the PMTs with the larger FoV. Due to the less precise outer ring of the camera, the analysis presented in this thesis will only be applied to events whose Center of Gravity (CoG) is in the inner part of the camera.

M2

The camera of M2 consists of 1039 pixels of 0.1° diameter set in a round shape, distributed uniformly over the entire camera plane, covering the same FoV as M1. The trigger region covers the entire camera plane, which is a significant difference to M1. In addition the PMTs used for M2 have a higher quantum efficiency than those used in M1.

2.2.2. Read-out system

The read-out system is located in a separate building, the counting house. For both telescopes the analogue signal of the PMTs reaches the readout system through fiber optic cables. The signal is then split into a digital trigger channel and an analogue readout channel. If the signal in a pixel exceeds a predefined threshold, a time window is opened for the L1, or level 1, trigger. The level 1 trigger uses temporal and spatial information to separate noise and Night Sky Background (NSB) events from signal events, by requiring that at least x connected pixels are triggered within a short time frame. For the analysis

presented in this thesis, data with a trigger of at least three connected pixels is used. This trigger operates for both telescopes individually. When a L1 trigger occurs, the read-out channel of the corresponding camera is sent to the L3-trigger, which is in charge of triggering stereoscopic events. For this, the data of the readout channel gets stored in a ring-sampler before being converted into digital signal. For more detail see [152, 153].

The read-out for M1 and M2 differ. The ring-sampler in M1, in addition to the delays in the fibre optics allows for a time window of 640 ns. An additional delay of 580 ns can be added to wait for the coincidence trigger and register the shower from the second telescope. It has a dead time of 25 µs in between events[99]. M2 offers an improved read-out with a lower dead time, 27 µs, as well as lower pedestal noise. For more details see [60].

These systems allow to store and delay the signal of an incoming shower, as it does not reach both telescopes at the same time. The coincidence trigger, also called L3-trigger, has a window of up to 200 ns between the triggers of the two telescopes, depending on the pointing positioning of the telescopes. This is due to the delay in the propagation of the Cherenkov photons from one telescope to the other.

In specific configurations, specifically when the telescopes are aligned in azimuth, the propagation delay of the photon (500 ns) can exceed the maximum delay in the system. This means that there is a so-called dead zone in which no coincidences can be triggered. Special care needs to be taken during observations, that no signal is lost due to this.

2.2.3. Data-taking

Standard data-taking includes a number of special runs taken to calibrate the system and to estimate the electronic noise. A pedestal run is taken at the beginning of each night and before every data run to calculate the pedestal offset, giving the absolute level of electronic noise in the readout system from. It is also used to calculate the RMS, quantifying the fluctuations in the pedestal. After the pedestal run, there is a calibration run with a laser shooting into the camera. This illuminates the camera evenly and allows to calculate the conversion factor between digital counts and Photo Electrons (PhE) as well as time-offsets between individual pixels. After these two runs, the data-taking starts. During the data-taking, interleaved pedestal and calibration events are recorded at a rate of 25 Hz. The pedestal events record only the background noise, while the calibration events record the triggered event from the calibration laser. Both type of events are used to correct potential gain changes during the data taking.

The data-taking itself is normally done in 20 min runs and in wobble-mode, in which the telescopes do not point directly at the source, but rather at an offset position of 0.4° to the source. After 20 min, the position is changed to the opposite side, again with 0.4° offset. This allows to define the anti-source position, that is opposite of the source position with respect to the camera center. The wobble positions are chosen, such that the anti-source is a dark region in the sky, where the background of the observation is being measured at the same time as the data on the intended source is being taken. This method allows to take a background measurement under the same weather and camera conditions and half the observation time needed, as background and signal are measured simultaneously. The term wobble comes from the back and forth movement (wobbling) of the camera around the true source position.

Data-taking takes place if the following conditions are met:

- Humidity $< 90\%$
- Wind Speed $< 40\,\mathrm{km\,h^{-1}}$
- Average PMT current $< 7\,\mu\mathrm{A}$
- Individual PMT current $< 20\,\mu\mathrm{A}$
- $1.5° <$ Zenith angle $<100°$

The PMT current is a direct function of the NSB. In case of single pixels reaching the threshold, they can be disabled individually. This is done, for example, when there is a star in the FoV. However when there is a lot of ambient light, the telescopes can not be operated, this is the case, for example, during full moon.
In total, this allows for about 1500 h of data taking per year, with moderate variation due to weather conditions.

2.2.4. Further subsystems

In order to ensure safe weather conditions for data-taking, a weather station is installed on site and continuously monitoring. In addition a pyrometer is used to measure the intensity of infra-red radiation in the FoV of the MAGIC telescopes. From this the sky-temperature is extracted assuming it is radiation of a perfect black body. The sky-temperature varies with the amount of clouds in the sky, as the clouds reflect the thermal radiation from the Earth back. This temperature is used to calculate empirically the so-called cloudiness, a value normalized to 100, which gives a rough estimate on the weather and cloud conditions in the observed part of the sky.

Since 2013, a LIDAR[94] is in place to measure the clouds in the FoV of MAGIC as well.

Information from these subsystems is stored with the data to allow for quality selection based on weather conditions at a later stage in the analysis.

2.3. Data processing with the MARS framework

This section shortly summarizes how MAGIC data is processed up to the highest level. It describes the standard settings used for the direction-dependent analysis.

The methods are the same as used for the analysis presented in this thesis up to the stereo reconstruction. The analysis is done within the MAGIC Analysis and Reconstruction Software (MARS)[136] which is written in C++ and based on the ROOT framework[69, 115]. The MARS package includes several dedicated programs that perform the different steps of the analysis. For the analysis of this thesis, a new program (electronflux) was developed, extracting the energy density spectrum for diffuse electrons. A simple chart of the processing is shown in Fig. 2.6.

The main analysis programs are:

callisto: Conversion of the digital counts into number of PhE for each pixel, subtraction of pedestal, removal of calibration and pedestal events. See 2.3.1.

Star: Image cleaning, parametrization of each image on the camera plane, calculation of the Hillas parameters. See 2.3.2.

SuperStar: Combining the data from both telescopes, 3D reconstruction of the shower parameters. See 2.3.3.

coach: Training of decision trees which help separate hadronic from electromagnetic showers (γ-hadron separation) and trees that will improve shower orientation reconstruction. Generation of look-up tables for the energy estimation. See 2.4.1.

melibea: Application of the aforementioned decision trees and look-up tables to the data, recalculation of the 3D shower parameters with improved orientation.

flute: (for point-like sources) Calculation of the effective area, effective time and excess events in order to compute the energy spectrum and light curves. See 2.4.

Unfolding: Correction of the energy spectrum by unfolding the spectrum based on the migration matrix of the energy. See 2.4.3.

In addition, the programs **Odie** and **Caspar** are dedicated tools to find the significance of an excess from a source and create sky maps respectively, but they are not used for the diffuse analysis.

2.3.1. Signal reconstruction and calibration

Raw data is processed directly on site. The data acquisition system stores information for each pixel individually as digital counts. In particular, it stores the intensity registered in the pixel and the arrival time of the Cherenkov light. The timing information is preserved, as the dish was constructed to be isochronous. Information, such as the time of the peak maximum and the rising edge of the pulse in each pixel is reconstructed by a program called callisto[37].

It first subtracts the pedestal and corrects for irregularities, using both the nightly and the interleaved calibration events. As the MAGIC PMTs do not resolve photons individually, the conversion from counts into the number of PhE is done by means of the so-called F-Factor method[134]. The initial calibration run is used to calibrate all PMTs relative to each other, by homogenizing the response of individual pixels to the laser pulses. The interleaved calibration runs are then used to compute the conversion factor of digital counts into PhE using the F-Factor method.

For this method, the short light pulses of the calibration laser are assumed to generate a Poisson-like distributed number of events. The distribution can then be parameterized by the mean value N of calibration events in the pixel and the RMS of this value $\sqrt{N}$. The mean charge registered by the PMT, $\langle Q \rangle$, and its RMS σ can be characterized in the same way. The F-Factor is then the ratio between the expected, ideal Poisson distribution and the actual measured distribution for each PMT. It was determined experimentally in the laboratory and is defined as:

$$F \frac{1}{\sqrt{N}} = \frac{\sigma}{\langle Q \rangle} \tag{2.11}$$

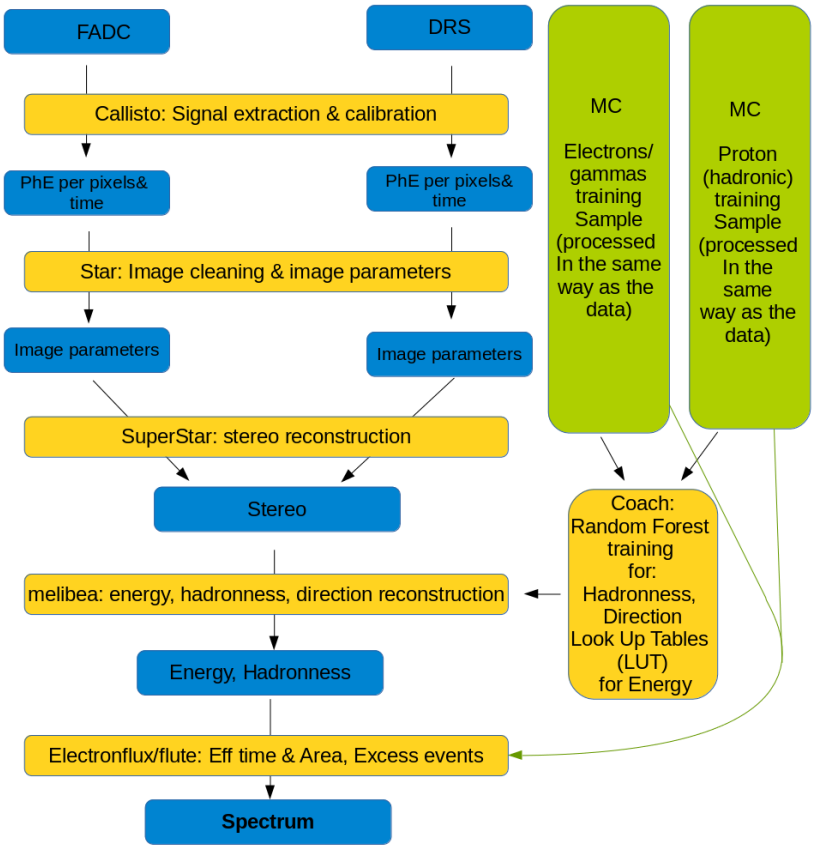

Figure 2.6: the MARS Stereo analysis chain from raw data to spectrum determination. The MC samples are processed up to SuperStar level and used for the training of the decision trees.

The conversion factor between digital counts and PhE then uses the interleaved calibration events to take into account variation in the response of the PMTs:

$$C = \frac{N}{\langle Q \rangle} = F^2 \frac{\langle Q \rangle}{\sigma^2}. \tag{2.12}$$

N is the mean number of calibration events and $\langle Q \rangle$ is the mean charge. This is used to convert the digital count to PhE for triggered events.

2.3.2. Image cleaning and Hillas Parameters

The next step is the image cleaning and the parametrization of the recorded shower on the camera plane. The dedicated program for this task is called Star.

Image cleaning

At this level the data consists of the number of PhE with its arrival time for each pixel of the camera. Since the Cherenkov light fades towards the border of the image, special care needs to be taken not to lose important information when the image is parameterized. This section contains a short description of the standard image cleaning, a more detailed summary of the different cleanings tested and used for the analysis of the diffuse electrons will be given in the chapter 3.1.

The standard image cleaning uses two thresholds: one for the core of the image and one for the boundary pixels to take into account the aforementioned weakening of the Cherenkov light towards the border. In addition, a time cleaning is used, since Cherenkov flashes only last a few nanoseconds. Setting a clear cut on the timing allows to reject more background noise and lower the overall thresholds.

The steps are implemented as follows in the MARS framework: First, the image core is identified as all connected pixels exceeding the core threshold. In a second step, isolated pixels, meaning pixels with no neighbors, are set to unused. This includes both spatial isolation, as well as temporal, usually meaning pixels exceeding a time difference of 4.5 ns. In a third step, all pixels surrounding used pixels are checked against the boundary threshold and set to use if they exceed it and are within the requested time window.

The thresholds are determined empirically. Between 2009 and 2011, the settings of M1 were 6PhE for the core and 3PhE for the boundary, while M2 operated with 9PhE and 4.5PhE. These numbers can be varied depending on the NSB and light conditions, as well as optimizing the cleaning for special energy ranges or analyses.

Image parametrization

To calculate the image parameters, each pixel is given a relative position x_i, y_i on the camera plane and a weight $w_i = \frac{N_i}{\sum_k N_k}$, where N_i is the number of PhE in the pixel. The

correlation between the pixels is then defined as follows[187]:

$$\begin{aligned} c_{xx} &= \overline{(x-\overline{x})^2} = \overline{x^2} - \overline{x}^2, \\ c_{yy} &= \overline{(y-\overline{y})^2} = \overline{y^2} - \overline{y}^2, \\ c_{xy} &= \overline{(x-\overline{x})(y-\overline{y})} = \overline{xy} - \overline{x}\cdot\overline{y}, \end{aligned} \tag{2.13}$$

where the moments are:

$$\begin{aligned} \overline{x} &= \sum_i w_i \cdot x_i, \qquad \overline{y} = \sum_i w_i \cdot y_i, \\ \overline{x^2} &= \sum_i w_i \cdot x_i^2, \qquad \overline{y^2} = \sum_i w_i \cdot y_i^2, \qquad \overline{xy} = \sum_i w_i \cdot x_i \cdot y_i. \end{aligned} \tag{2.14}$$

From this one can define a correlation matrix:

$$C_{orig} = \begin{bmatrix} c_{xx} & c_{xy} \\ c_{yx} & c_{yy} \end{bmatrix}. \tag{2.15}$$

C_{orig} is invariant under rotations, therefore it is rotated by an angle δ, such that the matrix is diagonalized using the condition:

$$\begin{aligned} c_{x'y'} &= (\cos\delta \sin\delta) \begin{bmatrix} c_{xx} & c_{xy} \\ c_{yx} & c_{yy} \end{bmatrix} \begin{bmatrix} -\sin\delta \\ \cos\delta \end{bmatrix} \\ &= -\frac{1}{2}\sin(2\delta)\cdot(c_{xx} - c_{yy}) + \cos(2\delta)\cdot c_{xy} = 0. \end{aligned} \tag{2.16}$$

A detailed description of how the rotation is performed can be found in [187]. The angle can then be calculated to be:

$$\tan\delta = \frac{(c_{yy} - c_{xx}) \pm \sqrt{(c_{yy} - cxx)^2 + 4c_{xy}^2}}{2c_{xy}}. \tag{2.17}$$

The x-axis in the new system is then aligned with the main axis of the shower. In the new system $c_{x'x'}$ and $c_{y'y'}$ define the length and width of the ellipse respectively:

$$\text{Length}^2 = \frac{c_{xx} + 2\tan\delta c_{xy} + \tan^2\delta c_{yy}}{1 + \tan^2\delta} \tag{2.18}$$

$$\text{Width}^2 = \frac{\tan^2\delta c_{xx} - 2\tan\delta c_{xy} + c_{yy}}{1 + \tan^2\delta}. \tag{2.19}$$

The position $(\overline{x}, \overline{y})$ defines the position of the Center of Gravity of the shower. The Center of Gravity, as well as the width and length of the ellipse in a shower are illustrated in Fig. 2.7a.

The major axis is related to the temporal and longitudinal development of the shower and the minor axis is related to the lateral development. This parametrization was first introduced by Hillas[106] and yields the following parameters:

1. **size**: Total number of PhE in the image of shower after image cleaning.

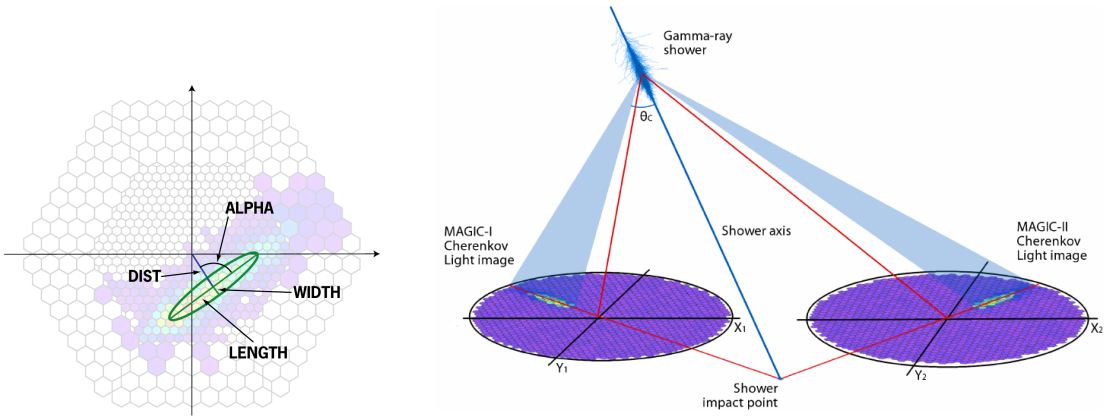

(a) Example of the Hillas parametrization of a shower image on the M1 camera. Taken from [40].

(b) Impact point and the distance between Impact point and telescopes, defined as the impact parameter. Taken from [96].

Figure 2.7: Reconstruction of Mono and Stereo parameters.

2. **length**: Half the length of the major axis of the ellipse.
3. **width**: Half the length of the minor axis of the ellipse.
4. **Center of Gravity (CoG)**: Center of gravity of the charge distribution in the image.
5. **alpha**: Angle between the major axis of the image and the line connecting the CoG to the source position in the camera plane.
6. **distance**: Angular distance between the CoG and the assumed position of the source on the camera plane.
7. **conc**(n): Short for concentration. Fraction of the image size contained in the n brightest pixels.
8. **leakage**: Fraction of the image size contained in the outermost ring of the camera. The leakage of the two outermost rings is called leakage2.
9. **islands**: Number of separate groups of pixels which survived the image cleaning.
10. **m3long**: Third moment of the image along its major axis.

In addition to these classical parameters, MAGIC also uses timing information, such as the variation of the arrival time along the major axis and the spread of the arrival times after image cleaning (which imposes a certain time window).

2.3.3. Stereo Reconstruction: Combining data from the two telescopes

Once the images are parameterized for both telescopes the data can be combined to get a 3D reconstruction of the shower. Further information about the shower can thus be gained:

1. **Shower direction:** The direction of the shower is calculated by superimposing the images of both telescopes onto one camera plane and calculating the crossing of the two major axes.

2. **Impact point**: The impact point on the ground is reconstructed by calculating the crossing of the major axes of the two images, but taking into account the telescope positions. See Fig. 2.7b.

3. **Impact parameter**: The impact parameter is the distance between the shower axis (calculated from the shower direction and the impact point) and the telescopes pointing direction.

4. **MaxHeight**: The maximum height is the height of the shower core. It is calculated by minimizing the circumference of the triangle, parallel to the ground, defined by points on each of the three lines: From impact point to shower core, from M1 to shower core and from M2 to shower core. Ideally these lines should intersect in one point in which case the circumference is 0. As the reconstruction is not perfect, the height of the plane on which the circumference is minimal is chosen as plane of intersection from which the height is then calculated. See Fig. 2.8.

5. **Cherenkov radius**: The radius of the Cherenkov light pool on the ground. It is calculated by assuming the emission of a single electron with critical energy at the previously calculated MaxHeight.

6. **Cherenkov photon density**: The density of Cherenkov photons on the ground, calculated in the same way as the Cherenkov radius.

7. **Theta2**: (also θ^2) The square of the angular distance between the shower direction and the expected position of the source. This parameters is not used in the diffuse analysis.

The MaxHeight is essential, as it is the most effective parameter for the γ-hadron separation which is at the center of the diffuse analysis. The parameter also exhibits an azimuth dependence which was not accounted for in the MC simulations. The dependence was identified and investigated as part of this thesis and is detailed in section 3.4.

2.3.4. Hadronness

The hadronness is a quantifier of the particle type of the incoming shower. It can differentiate electromagnetic Shower, such as γ-rays and $e^{\pm}$ from other cosmic rays, mostly protons. The particle type is quantified as a likelihood for an event to be hadronic, the "hadronness". The value is determined by a Random Forest (RF) method[38] based on the different shapes of the image on the camera plane[107]. The RF is a set of decision trees, in this case a 100 trees. The selected cut parameter is chosen randomly for each node and optimized for the best separation between hadrons and electrons. The tree ends either when the (predefined) maximal length of the tree is reached or when a sample is pure in hadrons or electrons. In order to measure the cut performance and optimize the cut value for a given parameter the Gini index is used. The Gini index measures the purity of a sample, quantifying how

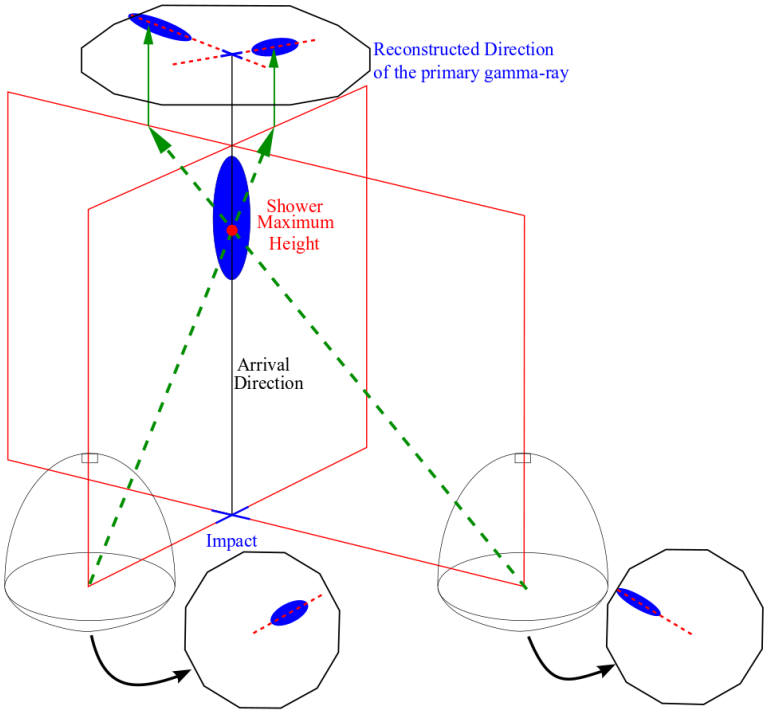

Figure 2.8: Visualization of an ideal reconstruction of the stereoscopic shower parameter Maximum Height[173]. The three lines meet in a single point from which the Maximum Height is identified.

well signal and background samples have been split, and has a value between 0 and 1. It is given by:

$$Q_{Gini} = 4\frac{N_e N_h}{N^2}, \tag{2.20}$$

where N_e is the number of signal, N_h is the number of background and N is the total number of events in a sample. When the sample is pure, either N_h or N_e is 0 and the Gini index is 0. The goodness of a cut is estimated by comparing the Gini index of the starting sample to the combined Gini index of the two successor nodes, which is defined as:

$$Q_{Gini} = 2\left(\frac{N_{e,left}N_{h,left}}{N_{left}^2} + \frac{N_{e,right}N_{h,right}}{N_{right}^2}\right). \tag{2.21}$$

The difference between Eq. 2.20 and Eq. 2.21 is maximized for the chosen parameter to find the best choice. The mean decrease in Gini index for each cut parameter can be seen on the left in Fig. 3.6.The best discriminator between electrons and protons is the shower height, MaxHeight.
The trained RF is then applied to all data to assign each event a hadronness value between 0 and 1, 0 being the least hadron-like and 1 being the most hadron-like.

2.4. The analysis chain for point-like sources

The default analysis chain for the MAGIC telescopes is the direction-dependent analysis for the point-like sources. It is a well-tested method and used as a benchmark for the diffuse analysis developed for this thesis.

For point-like sources, the direction reconstruction is essential whereas the γ-hadron separation plays a subordinated role. However the improved direction reconstruction plays an important role also for the stereoscopic shower parameters, mentioned in the previous chapter. They get recomputed with the improved direction reconstruction and are stored alongside the original stereoscopic parameters.

2.4.1. Energy and direction reconstruction

Direction reconstruction

The improved direction reconstruction uses the Distance between Image centroid and Source Position (DISP), the angular distance between assumed source position on the camera plane and the image centroid. The image centroid is the core of the shower, at which the shower is the brightest. The DISP is a parameter originally developed for single telescope observations and defines the distance between the image centroid (the center of gravity of the ellipse) and the source position (denoted by a star in Fig. 2.9a). The DISP then gives the two points on the longitudinal axis of the ellipse, at the same distance as the source is from the centroid. The distance is calculated for a single telescope, using the following equation[84]:

$$\text{DISP} = A(s) + B(s) \cdot \frac{w}{l + \eta(s) \cdot L_2}. \tag{2.22}$$

w is the width, l is the length and s is the size of the Hillas ellipse while L_2 is the leakage2. $A(s)$, $B(s)$ and $\eta(s)$ are polynomial functions of $\log(s)$. The coe cients of the functions are estimated from MC simulations using a machine learning algorithm called Random Forest (RF), for more detail on RF see the following chapter, in particular section 3.1.2. Once the DISP is known, there is a degeneracy problem, as there are two positions on the major axis of the Hillas ellipse which fit the DISP, see Fig. 2.9a. The preferred position is then identified using stereoscopic information. For this, the distance between all possible DISP positions is calculated. The pair (one per telescope) with the smallest angular separation is selected as shown in Fig. 2.9b. All events with a squared angular separation larger than $(0.05°)^2$ are rejected as the reconstructed events in M1 and M2 do not point to the same origin. The impact point is then calculated as the average of the two disp positions

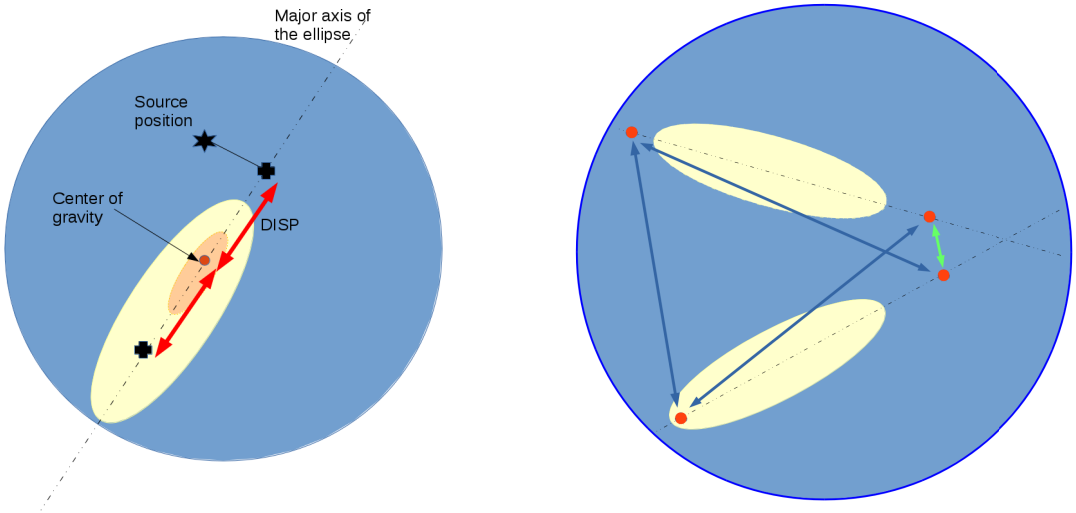

(a) DISP for a single camera **(b)** Stereoscopic DISP

Figure 2.9: Schematic illustrating the calculation of DISP for a single camera and for a stereoscopic system.

weighted with the size of the ellipses. The other parameters, depending on the impact point are also recalculated.

Energy estimation

The energy estimation is done by means of look-up tables (LUT)s, which are binned in size and in $\frac{p}{r_c}$, the impact parameter over the Cherenkov radius. The LUTs then contain the mean value of the true energy of γ MC and the RMS. The assigned energy for each event is then the mean of the LUTs value for each telescope, weighted with their RMS.

$$E_{\mathrm{EST}} = \frac{E_{\mathrm{M1}} \cdot \mathrm{RMS}_{\mathrm{M2}} + E_{\mathrm{M2}} \cdot \mathrm{RMS}_{\mathrm{M1}}}{\mathrm{RMS}_{\mathrm{M1}} + \mathrm{RMS}_{\mathrm{M2}}}. \tag{2.23}$$

In addition an empirical correction factor is applied which is a function of the cosine of the zenith angle and for the magnetic field. The energy resolution is about 15% and there

is no bias within the statistical uncertainties[41], the same study is done for the diffuse data in Fig. 3.5 and Fig. 3.4. There are no further steps in the data processing, the data is processed up to its highest level. The remaining task is to extract the physical information for the source.

2.4.2. Detection and Spectrum

The final step consists of extracting the information about the source from the data. Several possible steps can be taken. First one checks if there is a signal from the source. For this, the θ^2-distribution of the region containing the possible source is plotted against the θ^2-distribution of the background. γ-rays coming from the source should peak strongly at small values, while the background is expected to have a flat distribution. The signal region is then determined by a cut on θ^2 in addition to analysis specific cuts. Events passing these criteria are considered "ON" events. The number of background events is estimated by applying the same cuts on a data-sample containing no (known) source. The significance σ is calculated following Li and Ma[124]:

$$\sigma = \sqrt{2\left(N_{on}\ln\left[\frac{1+\alpha}{\alpha}\left(\frac{N_{on}}{N_{on}+N_{off}}\right)\right] + N_{off}\ln\left[(1+\alpha)\left(\frac{N_{off}}{N_{on}+N_{off}}\right)\right]\right)}. \quad (2.24)$$

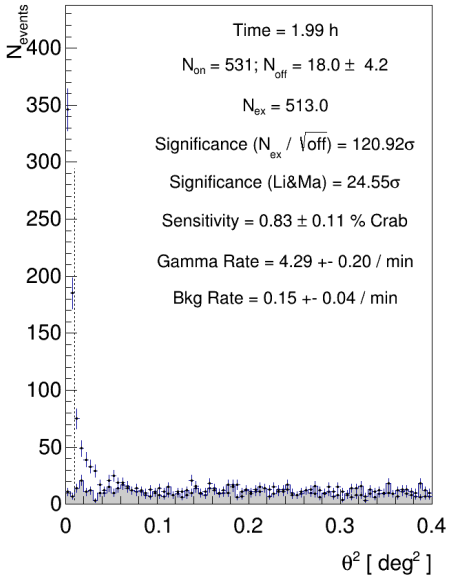

Figure 2.10: θ^2-distribution for 2 h of Crab Nebula.

α is the normalization factor between ON and OFF. This calculation is usually done by a software called Odie, a sample plot from Crab Nebula observations is shown in Fig. 2.10. It shows the excess coming from the pointed at position over the homogeneous background. The excess, the significance of the excess and the γ-rate coming from the source is also given.

For each selected source in the diffuse analysis, a reference analysis was performed with Odie to ensure that no point-like γ-ray source was seen in the data. An excess below 2σ for the point-source analysis was required.

2.4.3. Unfolding

If the analysis shows a significant excess, the next step is to compute the flux and the energy spectrum coming from the source. This is computed in bins of estimated energy. The finite energy resolution of the instrument (of the order of 15-25% for the MAGIC telescopes[39, 41]) and the indirect estimation of the energy causes distortions in the flux measurement. To correct for this the unfolding procedure has been developed: This is done by unfolding the spectrum using a migration matrix $\mathbf{M}$. It determines the probability of an event in the jth bin of true energy to be classified in the ith bin of estimated energy. It is determined from MC-simulated events: γ-rays for the point-source analysis, diffuse electrons for the diffuse flux measurement:

$$g_i = \sum M_{i,j} f_j \rightarrow \mathbf{g} = M \cdot f. \tag{2.25}$$

Index i runs over the estimated energy bins, the index j over true energy bins: f_j is the true flux in bin j. g_i is the measured flux in the estimated energy bin i. To find the true distribution of f, the equation needs to be inverted. Unfortunately ,the migration matrix is usually not invertible.The problem can not be solved analytically. The MAGIC software uses a numerically approach applying a least squared minimization method with an added regularization term[39]:

$$\chi^2 = \frac{\omega}{2}\chi_0 + Reg(\mathbf{f}). \tag{2.26}$$

Where ω is the regularization parameter determining the strength of the regularization.

$$\chi_0 = \sum_i \left(g_i - \sum_j M_{i,j} f_j \right)^2 \tag{2.27}$$

is the minimum of the least squared minimization method and Reg($\mathbf{f}$) is the regularization term. The MAGIC software has three algorithms implemented to solve the regularization, named after their authors: Tikhonov and Arsenin[177]; Bertero[57]; Schmelling[162]. The result of the unfolding depends on the migration matrix and the assumed spectral shape. They are specified independently of the value of the flux analyzed or the analysis method with which the flux was extracted. Therefore the same algorithms can be used for the point-source and the diffuse analysis.

2.5. Challenges for the diffuse analysis chain

Both the MAGIC telescopes and the MARS analysis framework are geared towards the analysis of point-like or small extended sources, which do not cover the full camera. Analyzing a diffuse flux is a challenge for several reasons.

First and foremost is the fact, that the main discriminator between background and signal, θ^2, can not be used in the diffuse analysis, making the separation of signal and background much harder.

The data cleaning and stereo reconstruction are optimized for the direction reconstruction and best signal-to-noise ratio for point-like sources, not for γ-hadron separation. Many of the parameter reconstructions, in particular the shower-parameters are optimized for γ-ray initiated showers. This leads to a wrong reconstruction of energy, impact and MaxHeight for the protons. This makes the differentiation between a correctly reconstructed γ-ray and wrongly reconstructed proton more difficult.

Contemporaneous data-taking for OFF and ON is impossible in the diffuse analysis, as the flux of diffuse electrons is homogeneous (within the uncertainties). This means that the entire background of hadronic cosmic rays needs to be simulated, and a very good matching between data and MC is needed.

The MC simulation is optimized for γ MC on the Crab Nebula, the standard candle for γ-ray astronomy. This is a single position in the sky and a galactic source, while the data analyzed for the diffuse flux is extragalactic. As was identified in the work for this thesis, the optimization is fine-tuned to the specific position of the standard candle and the matching is not equally good for all positions of the sky. This will be discussed in detail in section 3.4.

3. Developing the diffuse analysis chain

In this chapter, the analysis method developed and used for this thesis is described. The method identifies cosmic electrons and γ-rays independently from their incoming direction. This allows to estimate the diffuse flux of cosmic electrons and extract their energy spectrum. Emphasis is put on the differences between this method and the point-source method, described in the previous chapter, which is used for point-like sources.
The first part, section 3.1, will focus on the event reconstruction. The next section, 3.2, explains the event selection. In the last part, section 3.3, the method is applied to a known VHE standard candle as a proof of concept of the diffuse method. It also illustrates the calculation of the energy spectrum.

3.1. Adapting the analysis chain for the diffuse analysis

The data taking, calibration and signal extraction remain unchanged for the diffuse and the point-source analysis. Once the data has been selected, it needs to be processed specifically for the diffuse analysis chain. The following section describes in detail the modifications that need to be done at different levels of the analysis chain to allow for a successful estimation of the diffuse flux instead of the flux of a point-like source.

3.1.1. Event reconstruction and energy estimation

The selection and reconstruction criteria for events for the diffuse analysis differ from the default, point-source analysis. The diffuse analysis requires high quality events and only the most accurately reconstructed events are kept. This leads to several differences between the point-source and the diffuse analysis chain.
One is the selected image cleaning. Several image cleanings were tested, with a focus on signal to noise ratio, accuracy of image reconstruction and separation power between hadrons and electromagnetic showers and a good agreement between data and MC events.

1. **Standard image cleaning**:
   default image cleaning used in MAGIC, it was described in 2.3.2. It is used as a benchmark for testing other possible cleanings for improvements. The comparisons focus particularly on the data-MC agreement.

2. **"Moon cleaning"**:
   usually applied to data taken during moon time, which has more ambient light and thereby a higher night sky background. It uses the same basic rules as the standard image cleaning. However, the trigger thresholds are increased to reduce background noise to a level comparable to that of the standard cleaning. The thresholds are normally chosen based on the percentage of surviving pedestal events and the mean

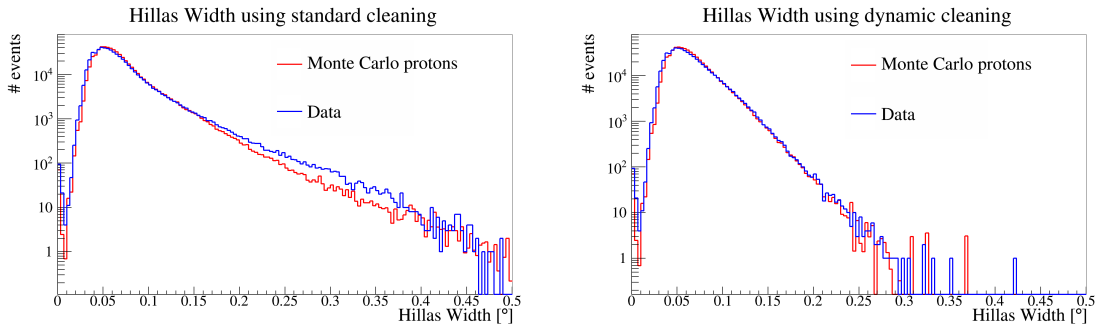

Figure 3.1: Data and MC protons distributions of the Hillas parameter Width for the first telescope, M1 at the final cleaning level. Cuts are applied to select protons in data and MC. Left: standard cleaning; Right: dynamic cleaning, for which the MC distribution matches the data distribution much better.

number of islands, since increased NSB will cause more islands generated by noise. It reduces the trigger efficiency, but the surviving sample contains better reconstructed events and less noise. This is an advantage for this analysis, since the available data set is large, making a small decrease in trigger efficiency affordable. Especially since the remaining data sample will consist of cleaner shower images, which make the separation of hadronic and electro-magnetic showers more efficient. However, the reconstructed parameters show the same mismatch as for the standard reconstruction illustrated in Fig. 3.1.

3. **Dynamic image cleaning**:
   developed to recover shower images at very low energies, which did not pass the cleaning threshold and to more accurately define large shower images for high energies. The dynamic image cleaning has two energy thresholds: One for the core pixels and one for the neighboring pixels. These thresholds scale with the total image size, thereby allowing very low thresholds for small images and higher ones for larger images. In addition to increasing the number of recovered events by about 5% in the range 100 GeV to 1000 GeV and about 10% above 1 TeV, the matching between MC and data also improves. This can be seen in Fig. 3.1, where a set of Monte Carlo protons is compared to a set of data selected to be predominantly hadronic. The Width of the Hillas ellipse, one of the main discriminators between γ-like and hadronic events, matches very well up to the largest widths for the dynamic cleaning, while the standard cleaned events show a mismatch at values above 75 mm. More details about the matching between MC and data can be found in section 5.4.
   As the threshold scales with the image size, the larger images are cleaned more aggressively. For energies above 5 TeV, the threshold becomes too aggressive and suppresses pixels that are part of the shower image. This leads to an apparent saturation effect, where all events with larger energies have roughly the same size. Normally the size (and in consequence the width and length of the ellipse) should scale with log(Energy). The saturation effect of the dynamic parameters are shown in Fig. 3.2, where the average dynamic Width and Length are plotted against the

true energy of the event. In particular, the average width becomes constant at high energies, above 4.5 TeV.

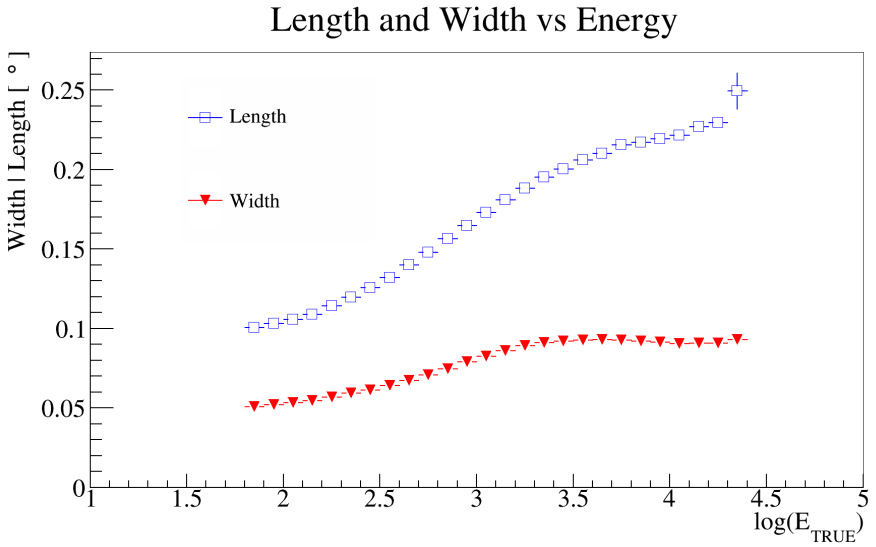

Figure 3.2: Average dynamical cleaned Width and Length of an event plotted against the standard cleaned size, showing the saturation effect due to the dynamical cleaning.

4. **Dynamic and standard image cleaning**:
   The standard and moon cleaning show mismatches for events with a size above >1000 PhE, this was not the case for the dynamic cleaning. However, the saturation effect of the dynamic cleaning impacts the analysis at high energies. Therefore, a hybrid cleaning relying on both standard and dynamical cleaning was applied to the data. Both cleanings were applied to the data and the resulting parameters for the reconstructed shower were stored for both cleanings. Events surviving the dynamic cleaning were kept. As such, this cleaning will be referred to as dynamical cleaning from now on. As the size in the standard cleaning scales roughly with energy, the standard size is used for the energy reconstruction and also for the γ-hadron separation. However, since the dynamic Width and Length show a better agreement in MC and data, they are used in the analysis.

The use of the dynamic cleaning leads to a larger signal region, which can be seen in Fig. 3.3. The plot on the left shows the hadronness cut used for the signal region versus the energy for the three different cleanings: The dynamical cleaning, the 'standard' cleaning and the so-called Moon cleaning. The signal region spans from 0 to the hadronness cut. It is determined by setting the percentage (65% in the plot) of the signal MC that should have hadronness smaller or equal to the cut. The plot on the right shows the percentage of background contained within the signal region.

As can be seen, the dynamical cleaning performs equally well as the other cleanings at low energies, while the signal region needs to be about twice as large at high energies. This means, there are more background events inside the signal region for the dynamical cleaning. Due to the limited statistics available from the MC, this is actually a desired

effect, as it allows for more MC events to be present in the signal region from which one can calculate the normalized background. This is increased by the fact that more events are successfully reconstructed with the dynamical cleaning than with the standard cleaning. The MC simulations also match the data better, in particular for large events. The less strict signal cut is not a draw back as the increase in background is correctly subtracted in the signal region. This can not be guaranteed for the standard cleaning, as the reconstructed MC events do not have the same parameter distribution as the data.

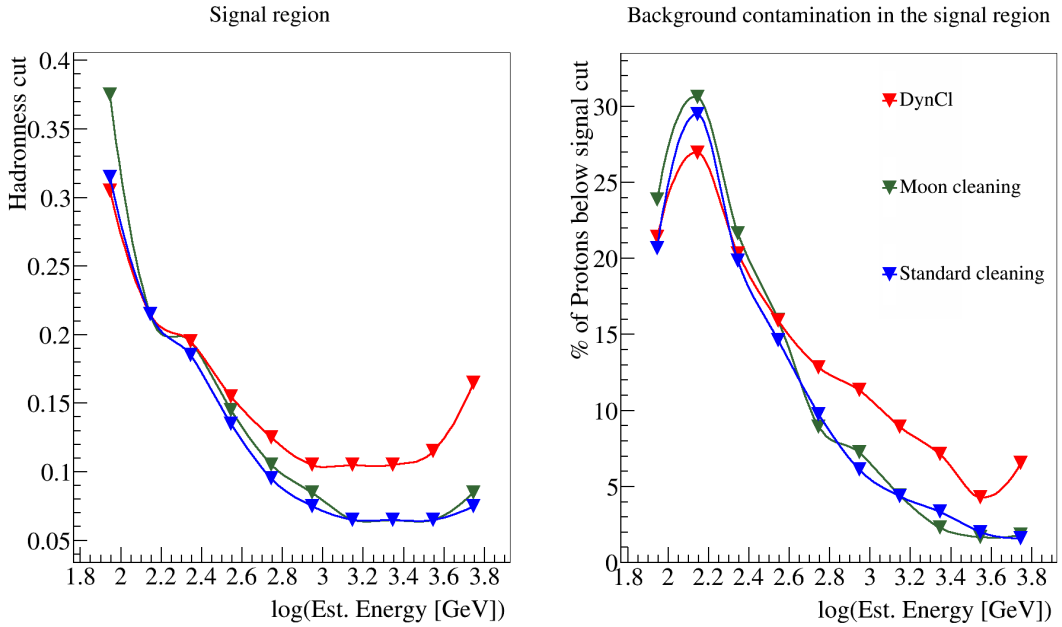

Figure 3.3: The left plot shows the upper hadronness cut containing 65% of the MC electrons as a function of energy while applying different cleanings: dynamical cleaning, standard cleaning and moon cleaning. The right plot shows the resulting amount of MC protons contained in the signal region defined by the cut from the plot on the left.

Stereo parameters

Once the images are reconstructed in the individual cameras of M1 and M2, the next step is to derive the stereo parameters, based on information from both telescopes. The methods are described in section 2.3.3. Uncertainties are given in chapter 5. The uncertainty is dominant on one parameter: the MaxHeight, the height at which the shower has its maximum development.

Energy and direction reconstruction

The energy bias is estimated compatible with zero as can be seen in Fig. 3.4. The resulting energy resolution is about 15% as can be seen in Fig. 3.5 and comparable to the one for the point-source analysis[41]. The energy resolution is given as the 68% confidence level of the energy reconstruction.

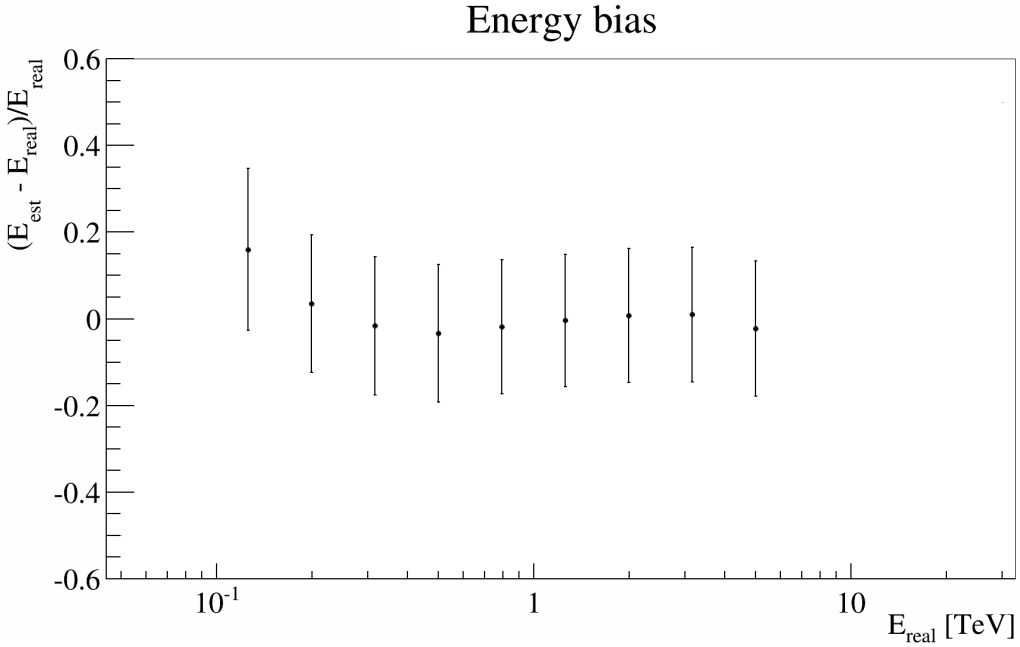

Figure 3.4: Energy bias of the energy reconstruction through look-up tables.

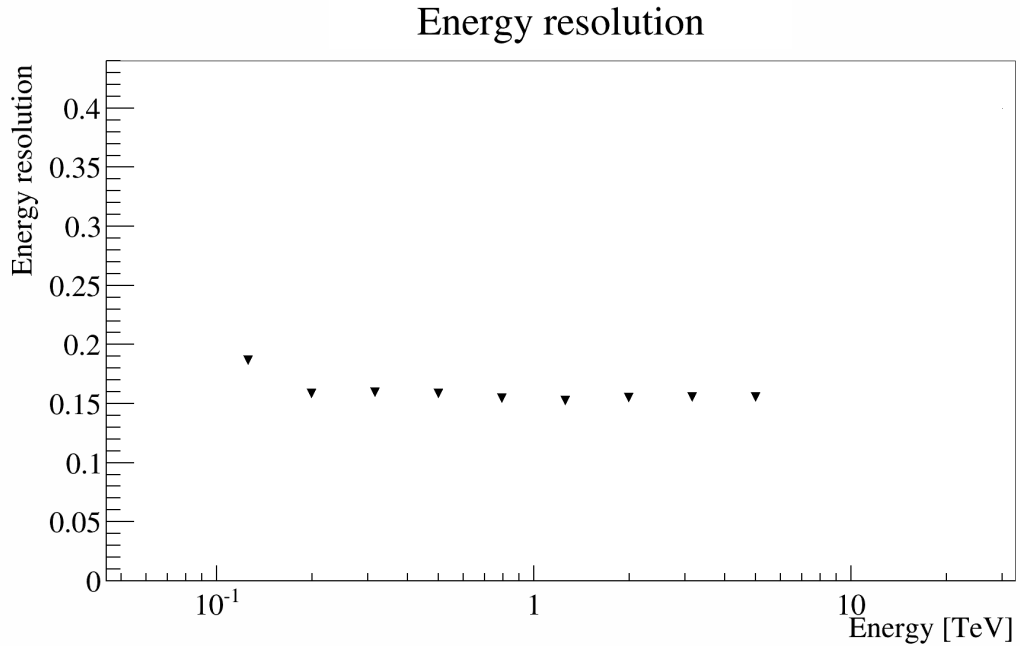

Figure 3.5: Energy resolution of the energy reconstruction through look-up tables.

3.1.2. Background rejection: γ-hadron separation

The background rejection strongly relies on the γ-hadron separation as there is no other background discriminator and no signal-free region is available to estimate the background. Contrary to the point-source analysis, one can not use angular cuts for background rejection. Instead, the particle type is used to differentiate the signal-like events such as γ-rays and $e^{\pm}$ from other cosmic rays, mostly protons. The particle type is quantified using the hadronness, which is the likelihood for an event to be hadronic. The value is determined by a Random Forest (RF) method[38]. Contrary to the point-source analysis, where the RF is trained on data as background and a point-source γ-ray MC as signal, the RF for the diffuse analysis is trained on two MC samples of pure diffuse MC electron sample as signal and a pure MC proton sample as background as there are no signal free regions. The following parameters are used for the training:

- Dynamic Width and Length, standard size of the image in each telescope.
- Point of impact as reconstructed for each telescope.
- MaxHeight, the height of the maximum intensity of the shower.
- Time gradient along the major axis of the image for each telescope.

To avoid a strong dependence on the zenith angle, the training and the data samples used have been restricted to the zenith range of 0–32 degrees. The azimuth region of the training samples has not been restricted, as the MC do not show a variation in azimuth that will affect the result. As previously mentioned, the main discriminator between electrons and protons will be the height at which the incoming cosmic ray dies out, the position at which the shower is brightest.

The protons will penetrate deeper into the atmosphere, resulting in a smaller MaxHeight of the shower. The protons are also expected to have more irregular shapes than the electrons and be more circular, whereas the image of an incoming electron should form an ellipse. The time variation in the image is expected to be smaller for incoming electrons than for incoming protons. The time variation and the impact point are also used to define the major axis of the ellipse, allowing for better differentiation between the Length and the Width of the image. The distribution of hadronness for a sample of diffuse MC electrons and protons can be seen on the right in Fig. 3.6.

3.1.3. Background estimation: Monte Carlo productions

In addition to playing a crucial role in the training of the Random Forest, the MC protons are used for the background estimation. This is necessary, since the flux is diffuse and no “electron-free” background measurement can be performed. Therefore, the background needs to be simulated and have very good agreement with data in the hadronness and by extension in the parameters involved in the training of the hadronness. For this, detailed studies have been performed to confirm the matching and regions where data and MC did not match are excluded from the analysis. More details can be found in section 5.4.

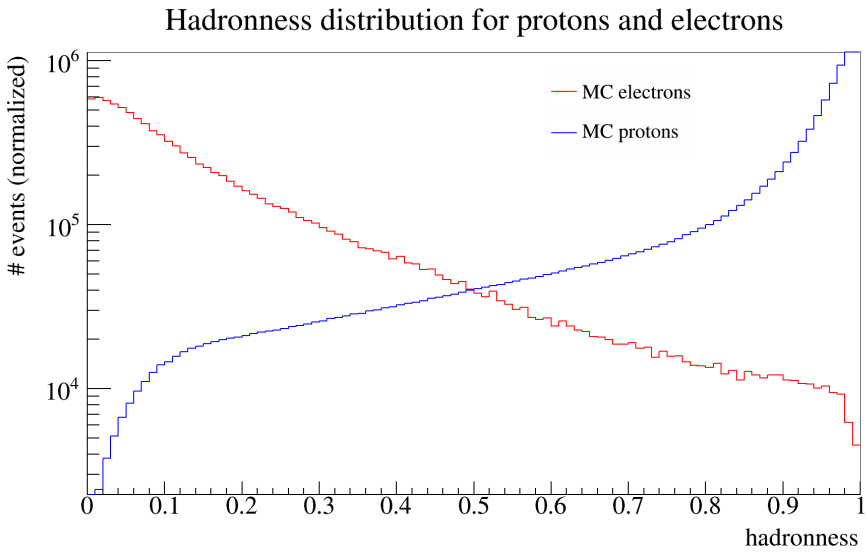

Figure 3.6: Hadronness distribution for MC electrons and protons.

Spectral Index Correction

In order to reduce computation time and still produce a sufficient amount of events at high energies, the MC productions are produced with a simulated spectral index of $\alpha = -2$. The true spectrum of cosmic protons has really a spectral index $\beta_1 = -2.7$ and the cosmic electrons have a spectral index of $\beta_2 = -3.2$. Therefore, for all comparisons and calculations the energy spectrum of the MC needs to be re-weighted. The weight is defined as $\left(\frac{E_{TRUE}}{1\,GeV}\right)^{\alpha-\beta_i}$ where E_{TRUE} is the energy at which the shower was simulated, not the reconstructed energy.

3.2. Event selection

The event selection is performed in several steps along the data processing chain. At the early stages the default loose cuts were kept (e.g. minimum size ≤ 30 PhE). Those cuts could be modified, but this was not needed. Much stronger cuts are applied at the final level due to the fact that this analysis relies on stable data and a very good matching between data and MC. The cuts can be split into three separate groups:

- Cuts removing events that are badly reconstructed due to the detector limitations (in this case the telescopes and the atmosphere are considered as the detector).
- Cuts removing events with large uncertainty in their reconstruction.
- Cuts removing regions of the parameter space in which MC and data do not match well.

3.2.1. Detector based preliminary cuts

The first set of cuts are mostly standard cuts related to the atmospheric conditions. This includes cuts on the cloudiness and the humidity which will directly affect the shower propagation in the atmosphere and the data taking rates. The following cuts were applied:

- Zenith lower than 32 degrees
- Humidity below 80%
- Cloudiness below 40
- Rates less than 15% above or below the average rate
- Same data-taking period for all the data, meaning comparable telescope conditions for all observations.

The zenith cut is chosen to keep the shower propagation distance in the atmosphere comparable for all showers: larger zenith angles lead to a longer path traveled through the atmosphere. This is accounted for in the standard point-source analysis by zenith dependent energy reconstruction, as well as high zenith MC simulation for the effective area. However, since this study relies on a large quantity of MC simulation as background, only a limited range of zenith could be covered due to CPU time and storage constraints. The largest zenith range with negligible zenith dependence was chosen. It coincides with the shortest distance traveled through the atmosphere.

In addition to the standard cuts, further cuts were developed to remove events which are incompletely imaged or lie in the less efficient part of the M1 camera. As mentioned in section 2.2, the camera of M1 consists of two different types of PMTs. The outer ring consisting of larger PMTs not included in the trigger region. The reconstruction and parametrization of events is harder and less accurate in that range. Therefore, a cut requiring that the center of the event be within 1.22 degrees from the camera center was added. The cut includes the entire trigger region, while excluding the outer layer of less precise PMTs. Additionally, a cut on both telescopes requiring that the Leakage of the event be less than 0.2 for M1 and 0.15 for M2 was added. This ensures that the events that are kept can be well reconstructed as only a small part of the ellipse lies outside of the camera.

3.2.2. Badly reconstructed events

The additional cuts developed in this section are unique to this analysis for two reasons: firstly the point-source analysis relies primarily on the reconstructed direction to discriminate between signal and background. Badly reconstructed events have a low chance of having the correct incoming direction. Secondly this analysis, as mentioned several times before, relies on the categorization of events as hadron-like, therefore a sub sample of very well reconstructed events is used to increase the accuracy of the γ-hadron separation. Several cuts were investigated, in particular for the shower parameters, but not all proved useful.

An obvious choice, such as the uncertainty attributed to the hadronness by the Random Forest, did not work out, as the training is done for discrete numbers. Therefore, the error

is very small for very low and very high hadronness values. But it will be large in the intermediate region, where the normalization of data and MC is done. There is no way to decorrelate the uncertainty and the hadronness value. So, cutting on the uncertainty is also cutting on the hadronness, which is used to determine signal and background regions and not as a preliminary cut. Therefore, this variable was discarded.

In a similar fashion, the uncertainty assigned to the reconstructed direction using the DISP method did not improve the event selection. However, the difference between the directions as reconstructed in the two telescopes proved a good quantifier of reconstruction quality. The reconstruction should be identical for both telescopes as they are observing the same shower coming from a single direction. If this is not the case, one or both telescopes are badly reconstructing the event. So, a strong cut was applied to the square of the angular distance between the two reconstructed directions called DispDiff2.

As already alluded elsewhere, the reconstruction of MaxHeight has proven to be problematic. In addition, the MaxHeight is reconstructed analytically from the position of the telescopes and the center of gravity of the shower. This means that there is no uncertainty associated to the reconstruction. Therefore, a new variable was introduced, quantifying the goodness of the reconstruction based on the circumference of the surface between the three reconstructed lines.

If the reconstruction is perfect, the three lines defining the MaxHeight should meet in a single point and the circumference of the surface should be zero. In reality, the reconstruction is obviously not perfect and a circumference of about $\approx 2000\,\text{cm}$ is considered a well-reconstructed event, while anything above 6000 cm is discarded as badly reconstructed.

Fig. 3.7 shows the circumference with respect to the reconstructed height. It can be seen that very high values for the circumference are primarily associated with very low MaxHeight outside the range for a normal air shower. The very low values of MaxHeight can probably be attributed to muon events, which will be mostly removed by this cut. This is, in fact, desirable, as they are not present in the proton simulations. The surviving muons have, normally, a very high hadronness value due to their low MaxHeight and do not enter into the analysis. The average circumference is minimal in the region in which the MaxHeight of an air shower is expected to be, around 10 km of height, and slowly increases again at higher values. Therefore, it was concluded that the circumference could give an estimate of the goodness of the reconstruction. A direct comparison to the true MaxHeight using MC is impossible due to the fact that this value is not stored in the MC. This differs from the true energy, for example, which is stored and allows for a direct estimate of the goodness of the reconstruction.

3.2.3. Parts of the parameter space where MC and data do not match

A more detailed study of data-MC matching is done in 5.4. The main cuts applied here are a size cut of at least 100 PhE, as well as a size cut requiring events to have a Size smaller than 10.000 PhE. This is done to limit the data to the range in which the background is simulated. The MC simulation for the background is generated for the energy range 70 GeV to 20 TeV. The signal used to calculate the effective area and migration matrix (used to correlate the estimated and true energy of events), is simulated between 70 GeV

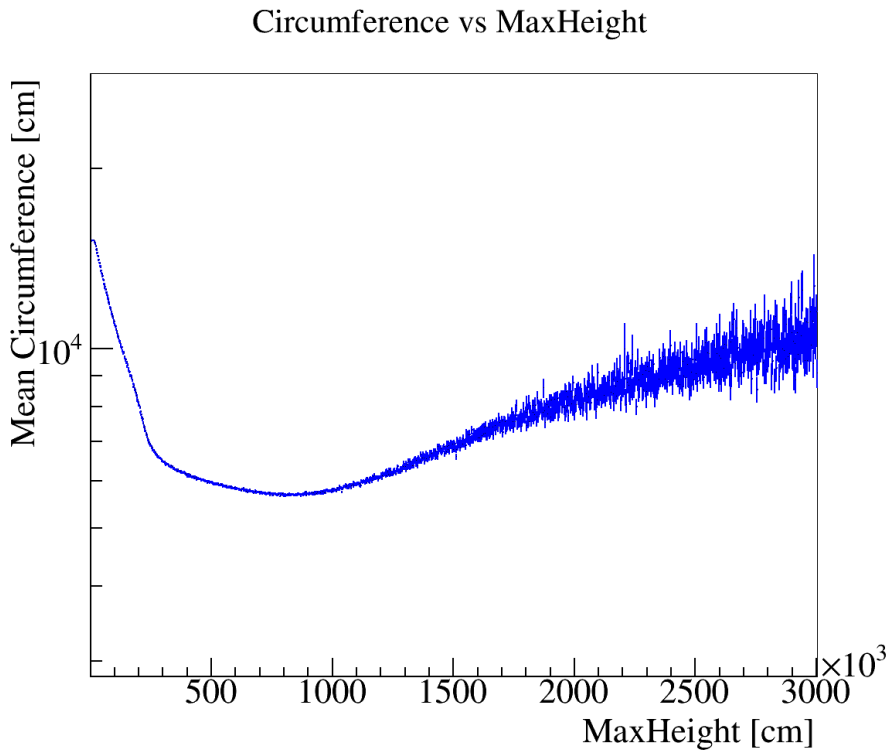

Figure 3.7: The circumference of the triangle used to pinpoint the MaxHeight vs the MaxHeight itself in cm.

and 7 TeV. Estimated energy cuts limiting the spectrum to between 100 GeV and 5 TeV are applied as well. Finally, a cut on the MaxHeight is applied to remove events which have a MaxHeight of less than 500 m. This is done to remove the remaining muons triggering the telescopes, as these are also not present in the MC protons.

3.3. A test case: applying the method to a point-like source

As a test case two well-known point-sources, Mrk501 in the north and Crab Nebula in the south, are selected to illustrate that the method correctly reconstructs the flux in southern sky, but not the northern sky. As Mrk501 is a highly variable source, only two nights were chosen, where the spectrum was available for cross check[59].

The selected data is listed in Tab. 3.1.

In a first step, the point-source analysis chain was used to determine the energy spectrum of the sources, as described in chapter 2.4. The spectrum for the Crab Nebula can be seen in Fig. 3.8a, the spectra for Mrk501 are shown on a night by night basis in Fig. 3.8b, 3.8c, 3.8d due to its highly variable flux. After that the diffuse analysis chain was applied to the same data sample, to compare the resulting spectrum with the one obtained by the point-source method.

Using the Crab Nebula spectrum as an example, the calculation of the flux will be detailed in the next section.

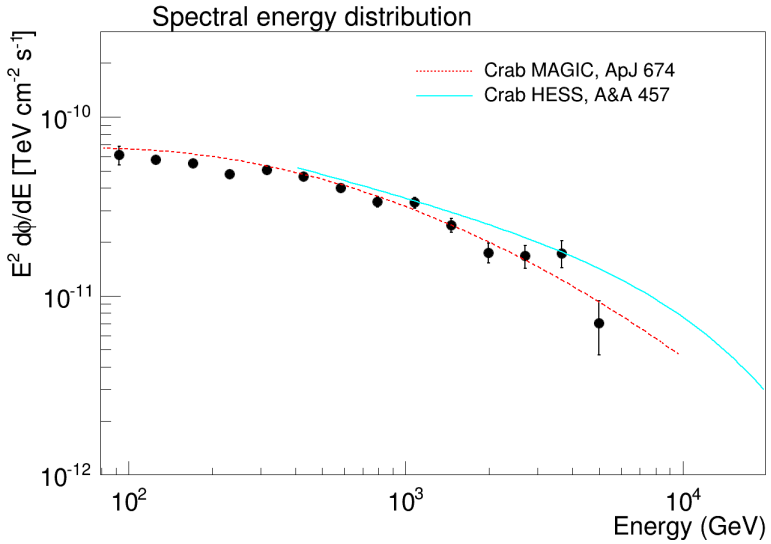

(a) Crab Nebula

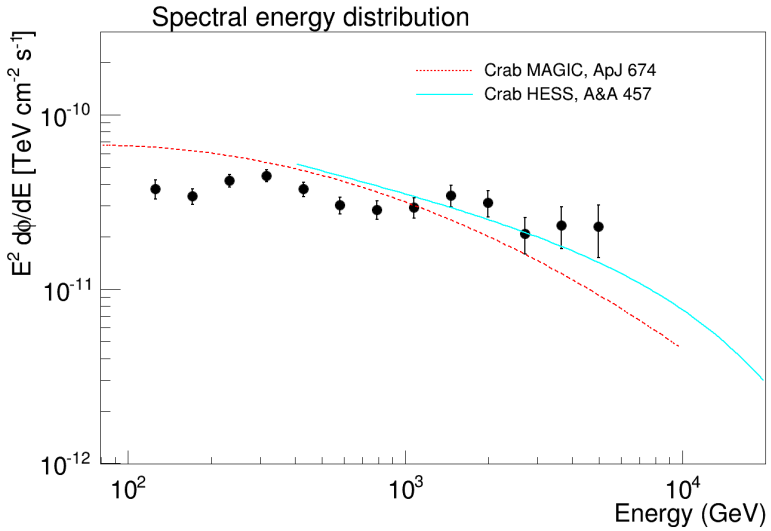

(b) Mrk501 on the night of 08.05.2011

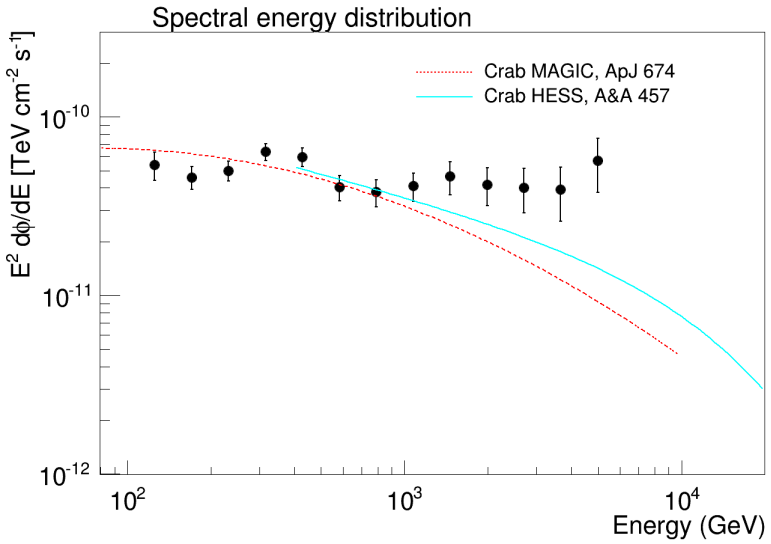

(c) Mrk501 on the night of 14.05.2011

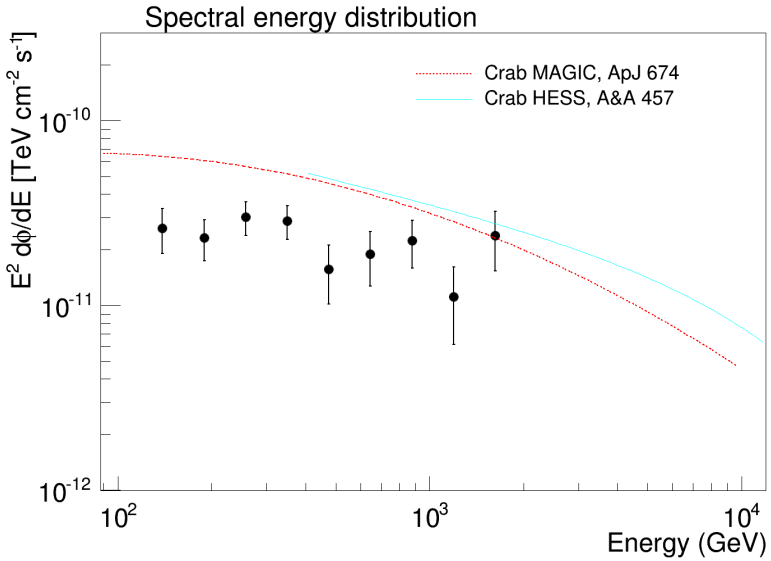

(d) Mrk501 on the night of 29.05.2011

Figure 3.8: Resulting energy density spectra for Crab Nebula and Mrk501 using the point-source analysis chain for point-like sources.

date	source	obs. length	zenith	azimuth
2010/11/08-14	Crab	225 min	20° to 32°	248° to 268°
2011/01/01-04	Crab	169 min	5° to 35°	150° to 270°
2011/02/01-07	Crab	116 min	20° to 30°	95° to 105°
				253° to 268°
2010/05/08	Mrk501	80 min	16° to 28°	40° to 60°
2010/05/14	Mrk501	56 min	23° to 30°	298° to 316°

Table 3.1: The data set for the two test cases.

3.3.1. Excess determination and flux calculation

The final step is to calculate the differential energy spectrum of incoming leptons, which is given by:

$$\phi\left(E\right) = \frac{dN_e}{dE \cdot dA_{eff} \cdot dt_{eff} d\Omega} \tag{3.1}$$

where N_e is the number of excess events (defined in Eq. 3.8), A_{eff} is the effective area (defined in Eq. 3.2), t_{eff} is the effective time (defined in Eq. 3.5) and Ω is the solid angle.

Effective area and acceptance The effective area is the area in which a shower could trigger the telescopes ideally, multiplied by the trigger-efficiency. It depends on the energy of the incoming showers and, above $\sim 35°$, on the zenith angle. It is computed from the MC electrons as a function of true energy in fine bins for zenith and azimuth. As an example the variation in the effective area computed for different zenith angles is shown in Fig. 3.9 as a function of true energy. A sample effective area calculated at 21° zenith is shown, as well as the averaged effective area used for computing the energy spectrum. The spread is small, in particular in the energy range of interest from 200 GeV to 1500 GeV. The final flux computation is therefore done using the averaged effective area for azimuth and zenith the same way as for the point-source method:

$$A_{eff} = A_{sim} \cdot \epsilon_e = A_{sim} \cdot \frac{N_{aftercuts}}{N_{tot}}, \tag{3.2}$$

where A_{sim} is the area in which the simulated incoming electrons are distributed, N_{tot} is the total number of events before trigger, $N_{aftercuts}$ is the number of events surviving the analysis cuts. For the case of the diffuse analysis, the fact that the particles arrive from multiple directions is taken into account by multiplying A_{sim} with the simulated solid angle Ω. Therefore, A_{eff} is sometimes referred to as the acceptance rather than the effective area.

Effective observation time The effective time is not identical to the elapsed time as there may be gaps in the data-taking. There is a dead time after recording an event in which the telescope can not be triggered. It can be estimated based on the distribution of the time delays between consecutive events.

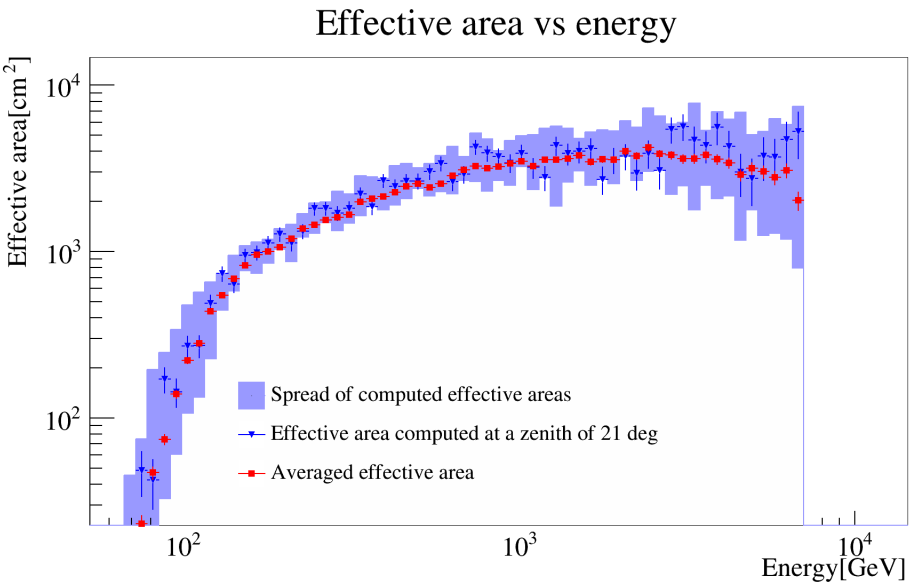

Figure 3.9: Spread of the effective area computed at different zenith below 30°. Red shows the averaged effective area for the entire zenith range. Blue shows a sample effective area calculated at a zenith of 21°.

The delay between incoming cosmic events follows a Poisson distribution:

$$\frac{dP\left(t_{next}=t\right)}{dt} = \lambda e^{(-\lambda t)}, \tag{3.3}$$

where t is the time and λ is the event rate. As the cameras have a fixed dead time, the total number of events is reduced and the delay gets shifted to higher values:

$$\frac{dN_{obs}}{dt} = \begin{cases} 0 \text{ for } t < t_{dead} \\ N_{obs}\lambda e^{-\lambda(t-t_{dead})} \text{ for } t > t_{dead}. \end{cases} \tag{3.4}$$

The slope of the exponential fall off remains unchanged,if $t > t_{dead}$, so it can be fitted as shown in Fig. 3.10 and the effective time then becomes:

$$t_{eff} = \frac{N_{obs}}{\lambda}. \tag{3.5}$$

This is identical to the calculation done in the point-source method.

Excess events The number of excess events is computed per energy bin, much like the effective area, though the binning for the effective area is much finer. The main background in the data are cosmic ray protons, which are expected to exceed the number of diffuse electrons by about two orders of magnitude. Therefore, the hadronness distribution of the data is expected to closely follow the hadronness distribution of MC protons, except for low values of hadronness, where an excess is expected due to the diffuse electrons and at values close to 1, due to heavier elements, such as Helium. The hadronness distribution of the data

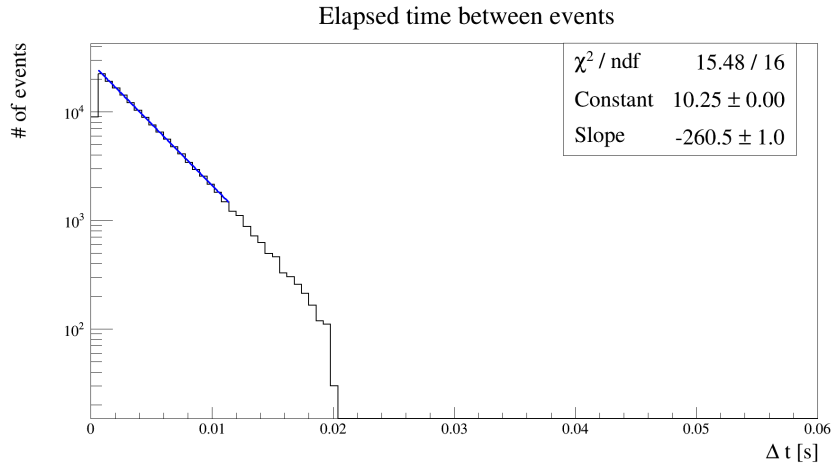

Figure 3.10: Time elapsed between two succeeding events (black) and the fit (blue) used to determine the rate. The first bin is underpopulated due to the dead time in which no event is registered. The cut off at 0.02 is due to the interleaved calibration and pedestal events taken at a rate of 50 Hz.

is normalized to the one of the MC protons used as background in the hadronness region between 0.4 – 0.8 where the data is expected to be dominated by protons. However, MC electrons may contribute a non-negligible amount of events, in particular at low energies, and therefore are taken into account in the normalization. The signal region is defined by an efficiency cut in hadronness on MC electrons. This cut is determined by selecting the lowest hadronness value containing at least 65% of all electrons. The efficiency can be varied as needed to avoid overlapping of signal and normalization region or too small statistics in the signal region.

After applying the cut, the number of signal and background events in both the signal and the background region is computed using Cramer's rule for the following system of linear equations:

$$\begin{aligned} N_{\text{sig,tot}} &= x_1 \cdot N_{\text{sig,MCe}} + x_2 \cdot N_{\text{sig,MCp}} \\ N_{\text{norm,tot}} &= x_1 \cdot N_{\text{norm,MCe}} + x_2 \cdot N_{\text{norm,MCp}}. \end{aligned} \tag{3.6}$$

sig and norm reference the signal and normalization region in the hadronness distribution respectively. So $N_{\text{sig,tot}}$ describes the number of total events in the data, $N_{\text{sig,MCe}}$ the number of events in the signal region for the MC electron signal simulation and $N_{\text{sig,MCp}}$ the simulated background proton events in the defined signal region. N_{norm} accordingly stands for the number of events in the normalization region. The variables x_1, x_2 are the normalization factor for the MC used for the signal and the background respectively. This

yields the normalization factors for the background as:

$$\begin{aligned} \text{NormProtons} &= \frac{N_{\text{norm,tot}} \cdot N_{\text{sig,MCe}} - N_{\text{sig,tot}} \cdot N_{\text{norm,MCe}}}{N_{\text{norm,MCp}} \cdot N_{\text{sig,MCe}} - N_{\text{sig,MCp}} \cdot N_{\text{norm,MCe}}} \\ \text{NormElectrons} &= \frac{N_{\text{norm,MCp}} \cdot N_{\text{sig,tot}} - N_{\text{sig,MCp}} \cdot N_{\text{norm,tot}}}{N_{\text{norm,MCp}} \cdot N_{\text{sig,MCe}} - N_{\text{sig,MCp}} \cdot N_{\text{norm,MCe}}}, \end{aligned} \tag{3.7}$$

where $N_{\text{norm,MCp}} \cdot N_{\text{sig,MCe}} - N_{\text{sig,MCp}} \cdot N_{\text{norm,MCe}}$ is the determinant of the system in Eq. 3.6 . The NormProtons is then used to renormalize the simulated background to the total data while accounting for the electron signal. Finally, the number of excess events is calculated as:

$$N_{excess} = N_{\text{sig,tot}} - N_{\text{sig, MCp}} \tag{3.8}$$

where $N_{\text{sig,tot}}$ is the number of data events and $N_{\text{sig,MCp}}$ is the scaled number of MC proton events in the selected area of the hadronness histogram. This value is computed for each energy bin individually.

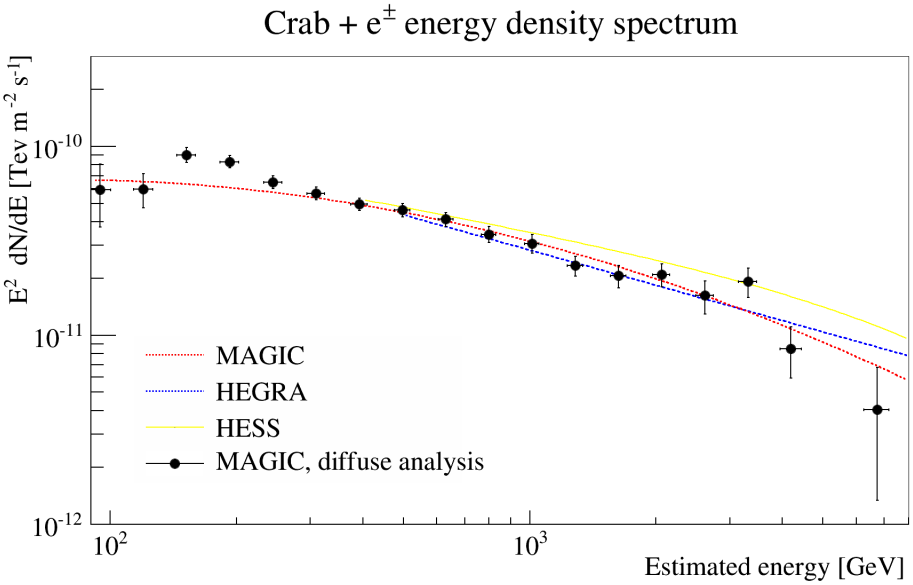

Figure 3.11: Resulting spectrum of the point-like source Crab Nebula using the diffuse analysis. This shows the reliability of the method, as the excess collected over the entire camera plane is dominated by the strong contribution from the Crab Nebula, especially at high energies.

3.3.2. The diffuse Crab Nebula spectrum

Fig. 3.11 shows the resulting Crab Nebula spectrum for the diffuse analysis chain using the same quality cuts as for the point-source analysis:

- Size $>$ 100 PhE
- Leakage $<$ 0.2
- Islands $\leq$ 1

and three additional cuts which are selecting well reconstructed events:

- MaxHeight circumference $< 4500\,\mathrm{cm}$
- Difference in the reconstructed DISP between M1 and M2 $< (0.02°)^2$
- Squared distance of the shower center from the camera center for M1 $< (\ 1°)^2$

An excess over the Crab Nebula spectrum measured by MAGIC[40] at low energies is present; this is to be expected since the measured electron flux[30][21] at those energies, integrated over the plane of the camera is roughly equal to the Crab Nebula flux. The expected number of excess events from diffuse electrons and the expected number of signal events from Crab Nebula are given in Tab. 3.2 and compared to the actual number of excess events measured with the diffuse method. The excess observed at low energies is due to the combined detection of diffuse electrons and point-like γ-rays from the Crab Nebula. Indeed, it can be seen that the excess at low energies drops off, if a cut is added to reduce the area on the camera plane to a circle containing only the expected source position at an offset of 0.4 degrees. This is illustrated in Fig. 3.12.

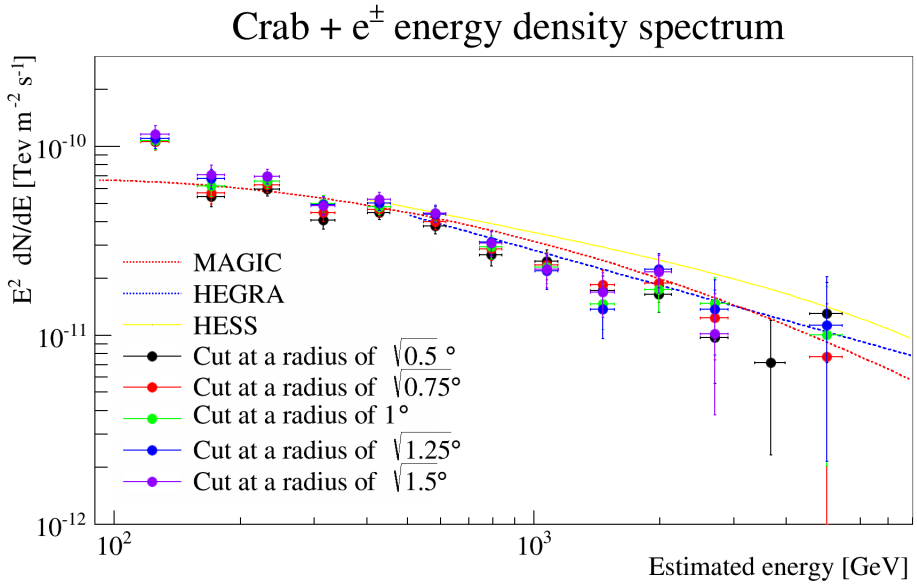

Figure 3.12: Effect of the size of the camera plane region on the measured Crab Nebula spectrum. The selected surface is a circle with different radii centered on the camera center. An event is selected if its center of gravity is inside the circle. The smaller the surface is, the fewer diffuse electrons are collected. The γ-rays arriving from Crab Nebula are unaffected as they are contained even in the smallest region.

3.3.3. Mrk501

As already mentioned in the previous section, the diffuse analysis is affected by a number of systematic uncertainties. The most significant one is the azimuth dependence of the hadronness in the data, that is not reproduced in the MC. This will be described in more

Table 3.2: Expected and measured excess events from Crab Nebula and diffuse electrons in five hours of Crab Nebula observations. The expected diffuse electron flux is taken from[32], the expected Crab flux is taken from [40].

Mean energy	Diff. flux (Fermi-LAT)	Diffuse $e^{\pm}$	Crab (MAGIC)	Expected γ	Measured excess	Deviation
GeV	$\mathrm{GeV}^{-1}\mathrm{m}^{-2}\mathrm{s}^{-1}$	# events	$\mathrm{TeV}^{-1}\mathrm{cm}^{-2}\mathrm{s}^{-1}$	# events	# events	%
173	$2.07 \cdot 10^{-9}$	654	$2.80 \cdot 10^{-5}$	492	1118	-2.5%
235	$1.05 \cdot 10^{-9}$	493	$1.10 \cdot 10^{-5}$	469	908	-5.5%
319	$5.20 \cdot 10^{-10}$	293	$3.45 \cdot 10^{-6}$	395	736	6.9%
434	$2.52 \cdot 10^{-10}$	205	$1.45 \cdot 10^{-6}$	297	467	-6.77%
590	$1.20 \cdot 10^{-10}$	147	$5.89 \cdot 10^{-7}$	212	327	-9%
802	$5.55 \cdot 10^{-11}$	79	$1.90 \cdot 10^{-7}$	136	181	-15.7%

detail in section 3.4. To shortly illustrate this effect, a second point-like source, Mrk501, was selected and a diffuse spectrum was produced. The azimuth range of the two sources are roughly opposite to each other while the zenith range used here is comparable. The resulting spectra are shown in Fig. 3.13, the calculated diffuse flux is about half of what the point like analysis shows.

Due to the azimuth dependence, the reconstructed MaxHeight in the data is significantly smaller in the northern sky than it is in the southern sky while it is constant for the MC. A small value of MaxHeight means that the shower penetrated more deeply into the atmosphere. This makes it look more like a hadronic shower. The Random Forest assigning the hadronness value will therefore give the northern sky events, on average, a higher hadronness value, than the southern sky events. Since the hadronness distributions are normalized in the intermediate region and the excess at low hadronness value is calculated to determine the flux, the flux is severely underestimated. Numerous attempts to understand or parameterize this behavior were undertaken. Unfortunately no viable solution was found and it was decided to limit the analysis to a range in the sky where the MC reproduces the data correctly.

3.3.4. Performance of the method compared to the point-source method

As illustrated in this chapter, the diffuse analysis method can reproduce a point-like source spectrum in the southern sky. However, it yields a lower sensitivity than the point-source analysis. As can be seen in Fig. 3.14 the sensitivity of the telescopes, using the point-source analysis method, is a factor 5 better than using the diffuse analysis method. This is mainly due to the fact that the strongest discriminator between signal and background, the incoming direction of cosmic rays, can not be used for the diffuse method. The results of this method for the diffuse electron and positron flux will be shown in the next chapter.

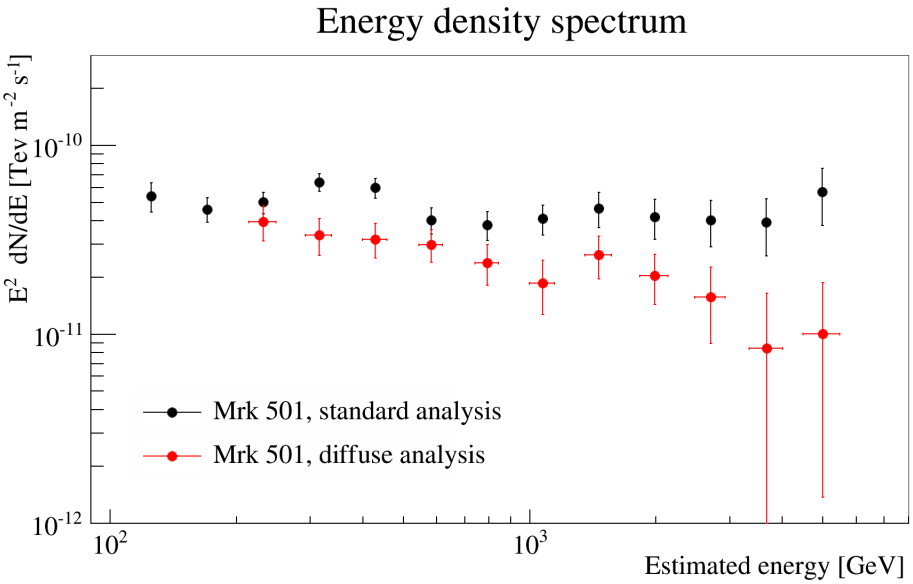

Figure 3.13: Results for the point-source and diffuse analysis of the same Mrk501 data. The plot shows the mismatch in calculated flux due to the azimuth dependence. It also illustrates that this issue only affects the diffuse analysis, not the point-source analysis.

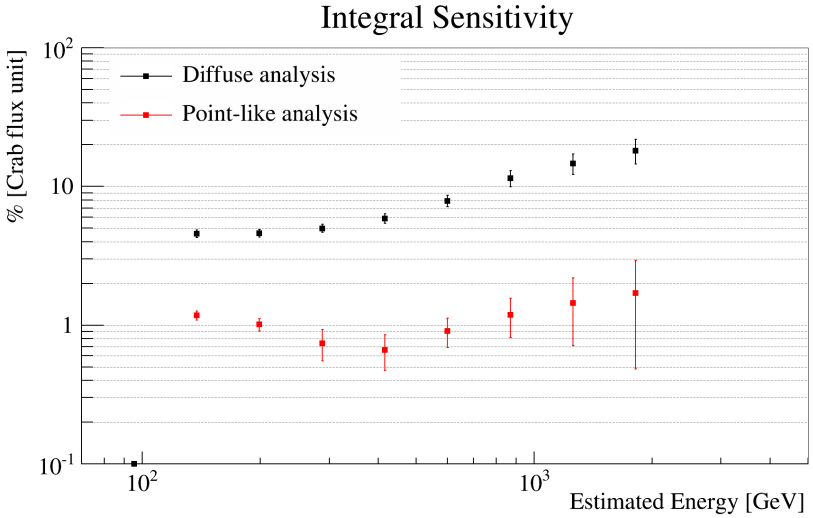

Figure 3.14: Sensitivity of the telescopes using the diffuse and the point-source analysis. The two lines show the flux that could be detected at a 5σ level within 50 h using a simple definition of significance as $\frac{\text{Excess}}{\sqrt{\text{Bkg}}}$.

3.4. Investigating the azimuth dependence

As previously mentioned, the diffuse analysis did not reproduce the spectrum of northern sources correctly. Upon investigation, an azimuth dependence in the data was noticed, which was not reproduced in the MC simulations. It affected most notably the shower parameters such as MaxHeight and Impact. Several explanations for this discrepancy were investigated, such as the geomagnetic field, an inconsistency between the actual and simulated telescope positions and an error in the MaxHeight reconstruction. Neither can fully explain the effects observed.

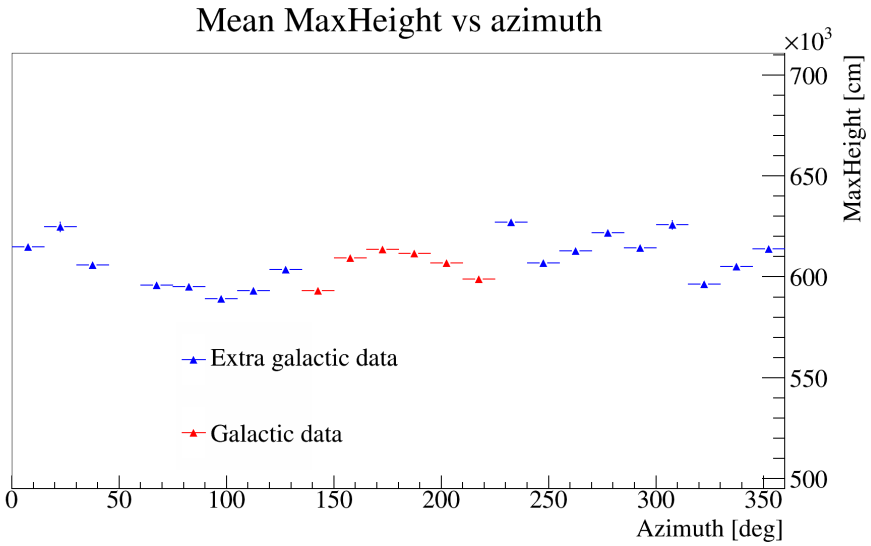

Figure 3.15: The average MaxHeight versus the azimuth direction of the telescope. The zenith range was limited to 25–35 degrees in zenith to minimize effects of the zenith in the data. The data was taken in 2013.

As can be seen in Fig. 3.15 the average MaxHeight of the extragalactic data is showing a wave shape peaked at 30 degree and 330 degree in azimuth. The galactic data is added for completeness to see the dependence over the full azimuth range. All sources used are non-detected sources, so called dark patches, so the registered cosmic rays should have the same distribution. This is not the data used for the measurement of the electron spectrum, even though that follows the same behavior. The sample selected here covers a larger range in azimuth and has a slightly higher zenith of (25° to 35°) than the data used for the electron spectrum analysis.

3.4.1. Decorrelating azimuth, zenith and time dependent variations

Due to the pointing of the telescope to a fixed point in the sky (while the Earth is rotating), zenith and azimuth are closely correlated in all data taken. To disentangle said correlation a dedicated study for the azimuth was performed. Data was taken at twelve fixed positions in the sky, with a zenith angle of 30 degree and varying the azimuth angle from 0 degree to 360 degree in 30 degree steps. Each position was observed for eight minutes only, to

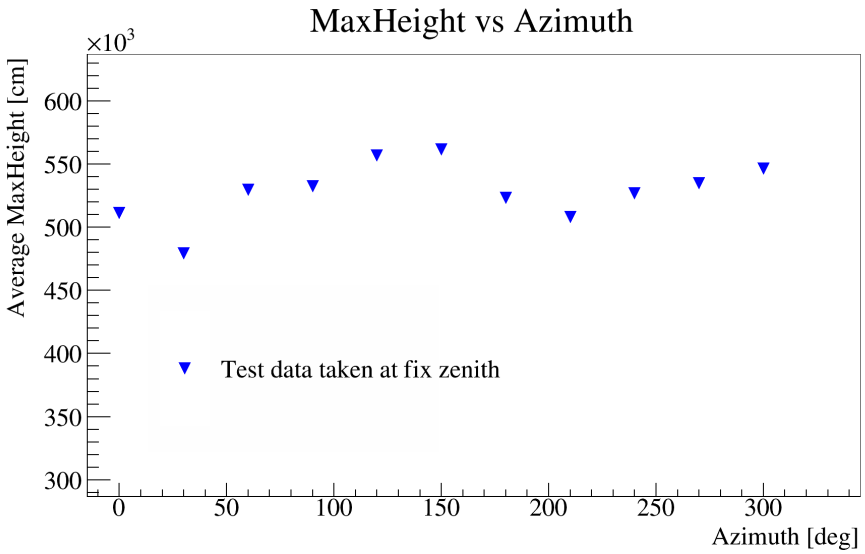

Figure 3.16: Average MaxHeight of all events surviving quality cuts for each of the twelve fixed positions used in the technical study of the azimuth dependence.

allow for the entire data of the study to be taken in a single night with very good weather conditions. Thereby removing variation related to weather changes and seasonal changes (as much as possible).

Figure 3.16 shows the resulting average MaxHeight for each of the observed locations. The variation between the mean MaxHeight is significant, up to 100 m. The data has a similar form of sinusoidal dependence on the azimuth in the MaxHeight. It does have a minimum in the average MaxHeight at 30 degree in azimuth and at 210 degree, which is what would be expected from a height difference between the two telescopes. As was discussed in section 2.3.3 the MaxHeight is reconstructed from the incoming shower using an analytic method: for each camera a line is defined from the location of the center of gravity of the shower image on the camera plane to the center of gravity of the shower.

An additional line is defined from the impact location to the center of gravity of the shower. Ideally, the three lines should cross in one point, but due to the uncertainties in the reconstruction this is not the case. Therefore a plane, parallel to the ground is defined and the three points where the lines cut the plane define a triangle on the plane, whose circumference is minimized. The height at which the three lines are closest, so where the circumference is smallest, is then taken as the MaxHeight of the shower.

A height difference between the two telescopes introduces a skewed plane in the MaxHeight reconstruction. The plane on which the circumference of the triangle is minimized is no longer parallel to the ground, causing the MaxHeight to be on average lower if it points in the direction of the plane inclination and higher if it is pointing in the opposite direction.

It has to be kept in mind though that each position observed contained only about a 1000 events surviving all cuts and the results have low statistics. Due to the constraints on weather quality and the need to perform this study in short time frames to keep weather conditions consistent, it was not possible to extend the study to investigate this further. While the study was not able to confirm that the problem stems (solely) from a height

difference between the two telescopes, it did confirm that there is an azimuth dependence in the data that needed to be investigated further.

3.4.2. Geomagnetic field

It has long been known that the geomagnetic field affects the development of air showers[80]. The transverse, meaning perpendicular to the shower development axis, component of the geomagnetic field acts on electrons and positrons pushing them further apart as the Lorentz force deflects them in opposite directions. This has a broadening effect on air showers, in particular for the electromagnetic showers[72]. This effect is expected to be more dominant in electromagnetic showers than in hadronic showers, as the deflection by Lorentz force is negligible compared to the lateral spread caused by hadronic interactions.

The effect of the geomagnetic field does not depend on the total strength of the magnetic field, but only on its transverse component. The MAGIC site was already selected based on its relatively low transverse magnetic field component as can be seen in Fig. 3.17 the transverse component is below 50 µT. In the range relevant for the diffuse analysis, the component is even below 40 µT. The effects were studied in detail in[81, 82], the effect is expected to be weakest for showers from the south and strongest for showers from the north, as can be seen in Fig. 3.17. In effect the transverse magnetic field component affecting

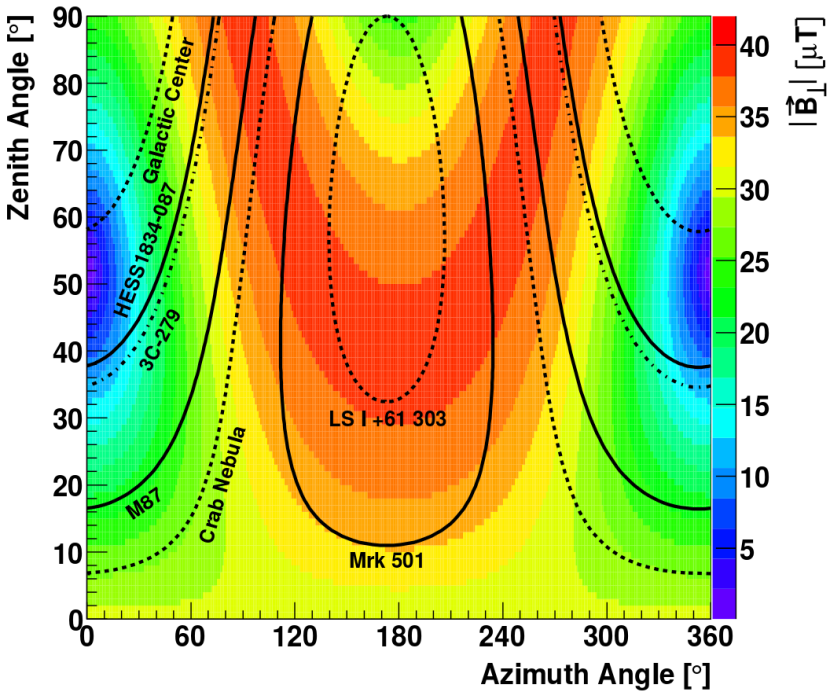

Figure 3.17: The transverse component of the magnetic field at the MAGIC site in La Palma for different azimuth and zenith angles. The azimuth, here, is defined in the same way as it is used in the MC simulation: it refers to the momentum of the incoming γ-ray and is counted counterclockwise from the positive x-axis towards west. Taken from [82]

data taken from Crab Nebula is about half as strong as for Mrk501 and could be a viable

origin of the mismatch between data and MC. But the effects of the magnetic field were studied in detail in [82] and the MC simulation does take into account the effect of the magnetic field while propagating the particles through the atmosphere.

In addition to checking that the MC does account for the magnetic field and shows no such azimuth dependence, an independent cross check was performed on the data. The deflection by the geomagnetic field is inversely proportional to the momentum of the particles. Therefore azimuth dependence should be most pronounced at low energies and gradually disappear at higher energies. Figure 3.18 shows the energy binned azimuth dependence in the data for the MaxHeight. It is visible that the variation in the data remains the same at all energies, which further contradicts the assumption that the effect is caused by the magnetic field. The magnetic field was ruled out as a cause.

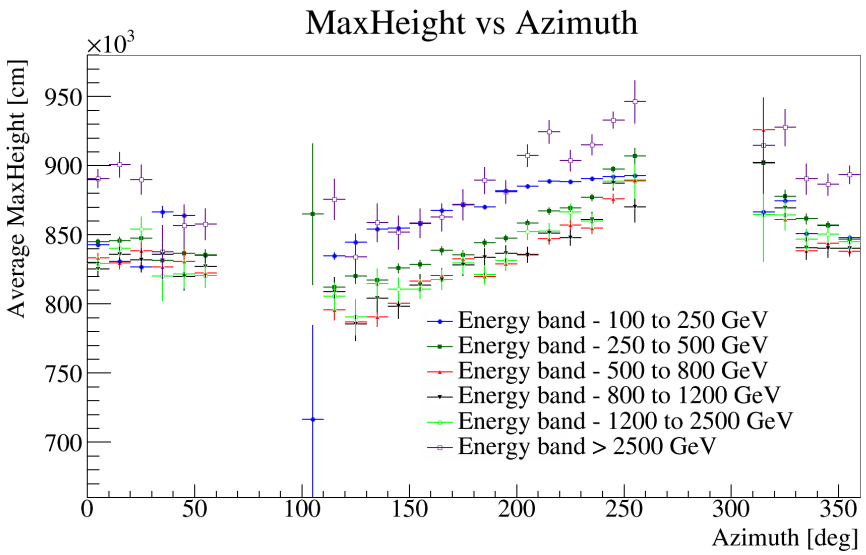

Figure 3.18: The mean MaxHeight versus azimuth for several energy bins. If the parameter were affected by the magnetic field, one would expect the effect to be strongest in low energy ranges and non-existing in high energy ones. In this case all energy bands exhibit roughly the same behavior.

3.4.3. Incorrect telescope position in the MC simulation

The next possible origin of the mismatch investigated was a possible inaccurate position of the telescopes in the MC simulation. Indeed the telescope positions had last been measured during the construction phase of the second MAGIC telescope and only accounted for the distance on the ground between the two telescopes, but not a possible difference in height. Several studies were performed to see how varying the telescope position would affect the reconstruction of the stereo parameters. As expected increasing or decreasing the distance between the telescopes did not add an azimuth dependence. It did, however, cause an absolute shift in the MaxHeight values. This does not significantly affect the training of the random forests much as the height for electrons and protons is shifted by the same number and the training looks for differences between the two.

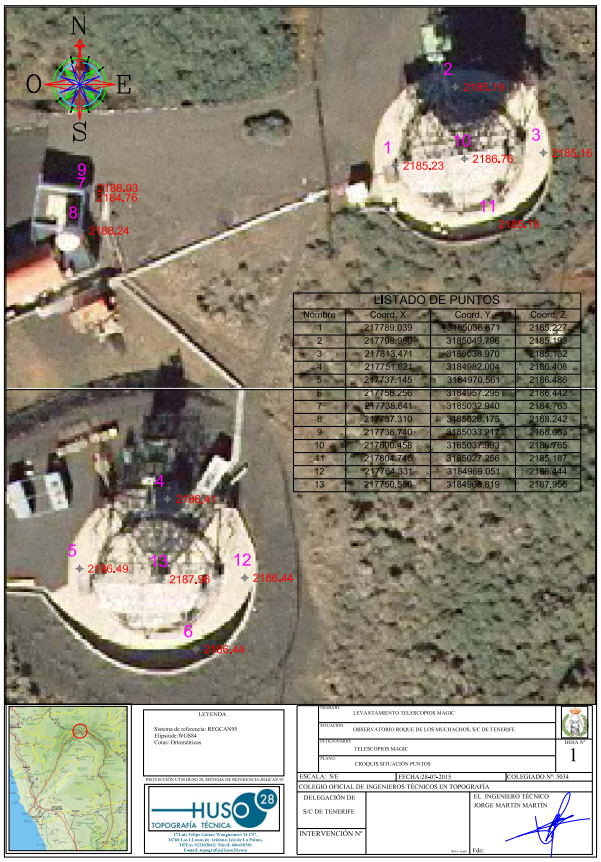

The parameters of the fit are given in the plot.

Figure 3.19: GPS based measurement of the position and height of the two MAGIC telescopes by Huso 28 Topografía Técnica

Id	X	Y	Z
1	217789.031	3185036.860	2185.197
2	217798.980	3185049.796	2185.193
3	217813.471	3185038.970	2185.162
4	217751.621	3184982.004	2186.408
5	217737.145	3184970.561	2186.486
6	217756.256	3184957.295	2186.442
7	217738.641	3185032.940	2184.763
8	217737.310	3185026.175	2188.242
9	217738.740	3185033.217	2188.033
10	217800.478	3185038.018	2186.764
11	217804.746	3185027.256	2185.187
12	217764.331	3184969.051	2186.444
13	217750.586	3184968.819	2187.956

Table 3.3: Absolute positions of the MAGIC telescopes and several other reference points as measured by Huso 28 Topografía Técnica.

.

For the next step, the data processing was adapted, so that a height difference between two telescopes could be taken into account. A few preliminary simulations showed that a height difference of a meter could already cause a visible effect in the data, see Fig. 3.20. The figure shows the average MaxHeight against the azimuth. The black line is the default MC simulation, the green shows the same simulation, with a difference of two meters in height between the two telescopes. The red shows the distribution with a height difference of 10 m. The latter is roughly the height needed to account for the azimuth dependence seen in the data in blue. The difference in average height between data and MC can be explained by the contribution of muons which have very low MaxHeight and therefore lower the average MaxHeight of the data. The muons are not present in the MC simulations.

To test this hypothesis, the position of the telescopes was measured by an external company: Huso 28 Topografía Técnica. Their measurement showed that the telescope position did indeed differ from the one assumed in the MC (and data reconstruction). The results can be seen in Fig. 3.19 and in Tab. 3.3. The figure shows the relative positions of the different measuring points, while the table gives the positions using the Universal

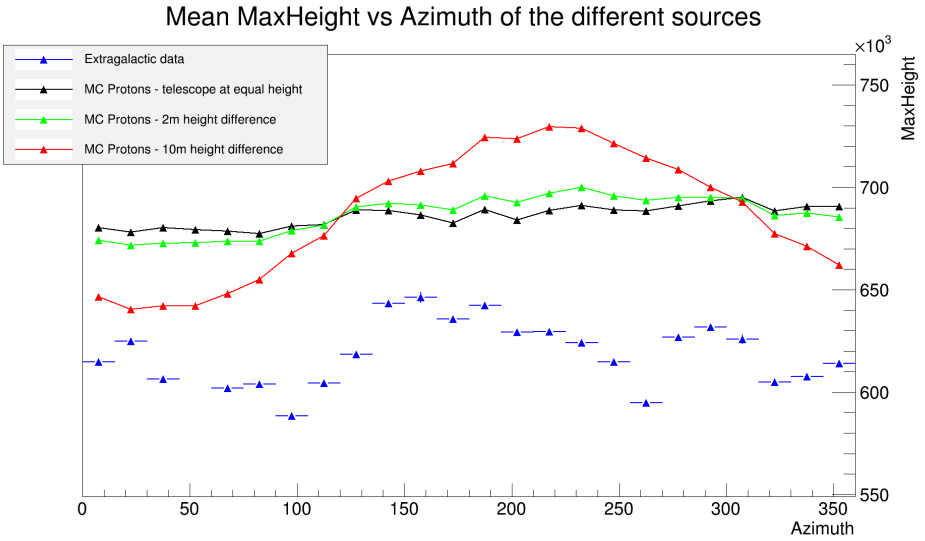

Figure 3.20: Effect of a height difference between the telescopes on the MaxHeight distribution with respect to the azimuth. Three simulations are shown for 0 m, 2 m and 10 m height difference. The azimuth dependence of the data is shown in blue.

Transverse Mercator (UTM) projection for the x and y axis, and the height above sea level as z.

The measurement has an uncertainty of about 5 cm for the height and allows for two important conclusions. First the telescopes themselves are each on a level surface. The z-values for the measured points 4, 5, 6, 12 for telescope M1 and 1, 2, 3 and 11 for M2 are compatible within error bars. The absolute height difference for the points is less than 8 cm. This means that there is no tilt in the camera plane. In addition the measurement also confirms that there is a height difference between the two telescopes of roughly 1.2 m which was previously unaccounted for. As could be seen in Fig. 3.20 a height of about 10 m would be needed to explain the fluctuation seen. The height difference of the telescopes causes less than a 5% variation in the average MaxHeight, it is therefore a minor contribution to the observed fluctuation of 50%. In addition, the telescopes are roughly half a meter further apart than previously thought. As a comparison, the previously used position in the MC simulation and the new positions are given in Tab. 3.4. The positions are given with respect to the center of the telescope system in centimeters. The x-axis is pointing towards the geographic north, the y-axis is pointing west. As can be seen from Fig. 3.20

	x cm	y cm	z cm	dist m	relative angle deg
Original MC settings	$\pm$3500	$\mp$2400	0	84.88	34.44
Professional measurement	$\pm$3459	$\mp$2494	$\mp$60	85.28	35.79

Table 3.4: Original and improved telescope positions used in the MC simulation. The position is relative to the center of the two telescopes, with the positive x axis pointing north, the positive y axis pointing west.

the height difference alone is not enough to explain the oscillation seen in the data, even if it contributes to it.

To take into account the height difference discovered during this analysis for the diffuse analysis the height difference is added to the MC simulation at the time when the shower parameters are calculated, rather than rerun the full simulation. This means that there still will be a small effect, as the shower simulation and subsequent processing is done for two telescopes at the same height, but the losses should be negligible. This solution was chosen due to time constraints regarding the large MC simulations needed for the background. A reprocessing of the data using the corrected telescope position to account for the height difference showed small shifts in the average MaxHeight which did not quantifiably affect the resulting hadronness distribution. So while this particular investigation led to a more correct implementation of both the data processing and the MC simulation, it did not prove to be the full origin of the azimuth dependence observed in the data.

3.4.4. Alternative MaxHeight implementations

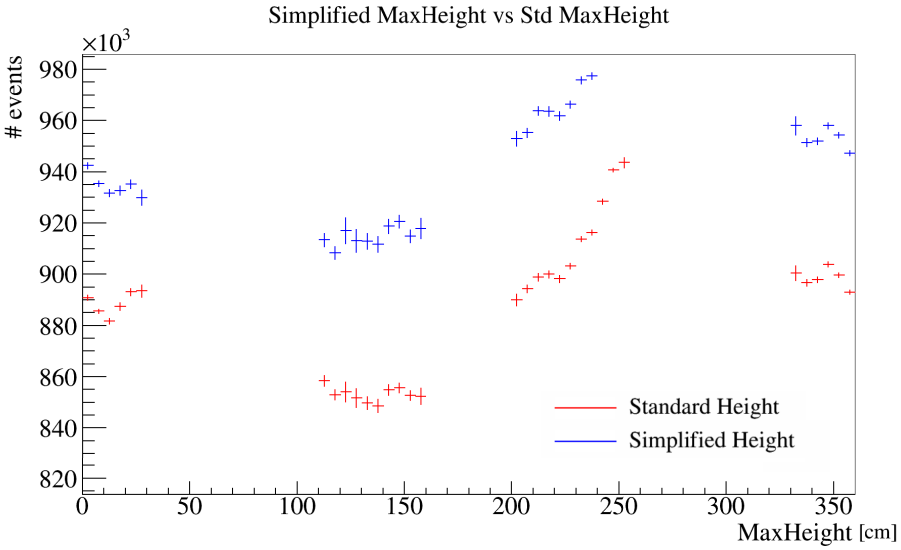

Figure 3.21: Distribution of the average MaxHeight for the standard calculation and the newly implemented simplified calculation. It can be seen that there is an offset between the two heights, but they follow the same azimuth dependence.

The MaxHeight is calculated as the intersection of three lines: the line from the first telescope to the center of gravity of the shower, the line from the second telescope to the center of gravity and the line from the reconstructed impact position to the center of gravity. A simplified reconstruction of the MaxHeight using only the two telescopes as points of origins was implemented to see if the azimuth dependence would be reduced. A comparison of the two implementations can be seen in Fig. 3.21. As can be seen the distribution of the MaxHeight match quite well, making a software issue unlikely.

3.4.5. Smearing data

A final attempt to homogenize the data was made by smearing the data. This was done for two reasons: a) to see if a smeared MaxHeight leads to a consistent result in the flux over time and b) to quantify the mismatch. Several of the data-processing programs (SuperStar, coach, melibea) were modified to add a Gaussian smearing to the hadronness parameter, as well as to the input parameters of the training of the random forest. As an example the results for the MaxHeight will be detailed here, since this is the parameter with the strongest influence on the hadronness.

A Gaussian smearing was added by multiplying the calculated value with a random number taken from a Gaussian distribution centered at one. The half-width was varied in steps of 0.05 until the resulting MaxHeight distributions matched for different data-taking periods. An example of this can be seen in Fig. 3.22. The right hand side shows the original MaxHeight distribution for the three months in which data was taken for the source Segue. The azimuth and zenith range are comparable for these months. Nevertheless the distribution for the data taken in February (blue) is visibly peaked at lower values than the two other months (March and April, green and red). The left hand side shows the smeared MaxHeight for all months. The three months now show a reasonable agreement, even if the February data still has a slightly lower average MaxHeight value. The plots shows a smearing of about 30%. The resulting, homogeneous, height was then used to

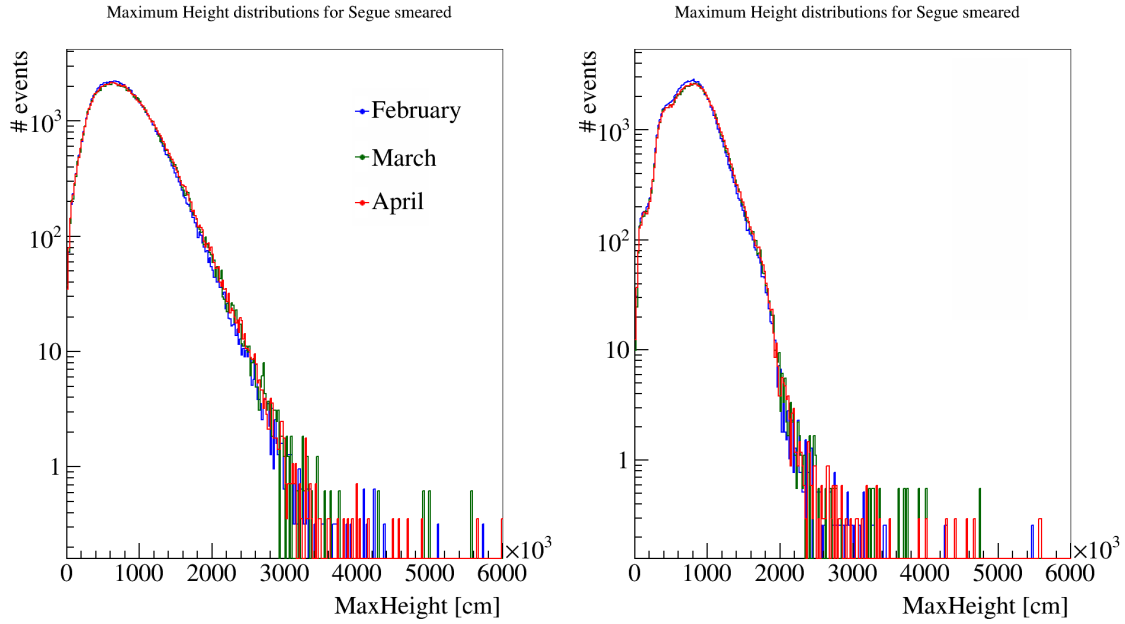

Figure 3.22: The right hand side shows the fluctuation in the average reconstructed MaxHeight in the data originally. The different colors represent different months of data-taking for the same source.The left hand side shows the smeared height with the distributions matching for the different months.

train the RF and get the hadronness. As expected, the hadronness for all periods is then

compatible. However, the smearing of the parameter needed to reach this is so strong that the parameter loses most of its discrimination power for the hadronness training.

The discrimination power can be quantified by the gini index, previously explained in section 3.1.2. Figure 3.6 shows the average variation in the gini index caused by each of the parameters in the training. The MaxHeight is the strongest discriminator, almost twice as strong as the second variable, the width of the Hillas ellipse. After smearing the roles are reversed: the strongest discriminator is now the width, followed by the MaxHeight, as can be seen in Fig. 3.23.

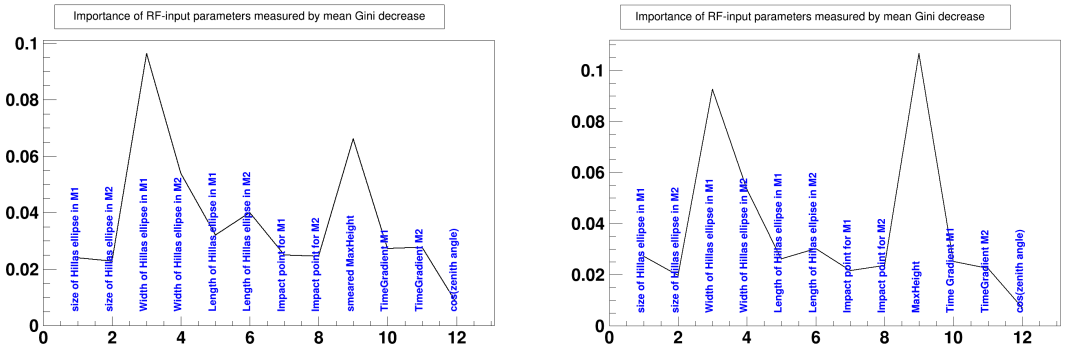

Figure 3.23: Average change in the gini coefficient for RF parameters numbered from 1 to 12 on the x-axis. The left hand side shows the training with a smeared MaxHeight and the right hand side shows a 'standard' training with the normal parameters.

As none of this proved to reduce the azimuth dependence, it was decided to reduce the data sample to the azimuth range in which the best agreement between MC and data was achieved, the so called south with an azimuth above 100 degrees and below 270.

4. The energy spectrum of diffuse cosmic electrons

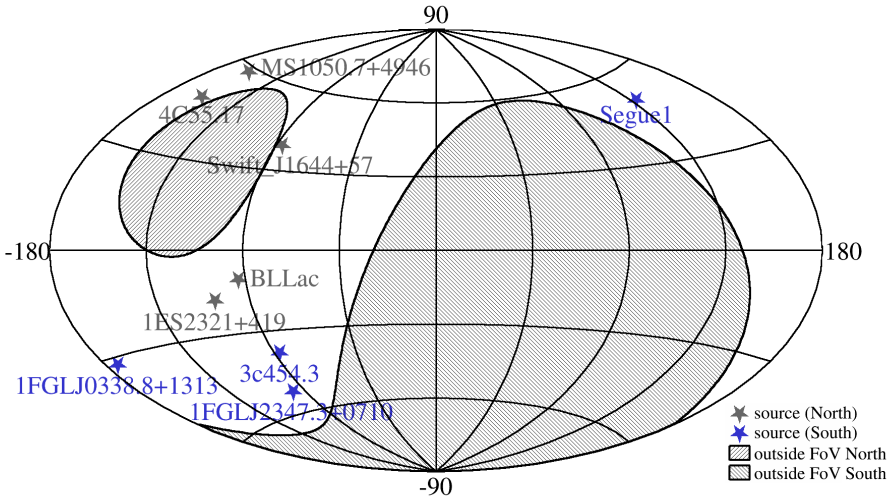

Figure 4.1: Sources used for the measurement of the diffuse electron spectrum with MAGIC

In this chapter the final energy density spectrum of the cosmic electrons and positrons as measured by MAGIC will be presented. The result is shown in section 4.1, including systematic uncertainties discussed in chapter 5. Section 4.2 will shortly cover possibly interpretations of the measured spectrum. Finally a short outlook onto possible extension will be given in section 4.3.

4.1. The Cosmic Electron Spectrum

The method described in chapter 3 will now be applied to data containing only diffuse cosmic rays and no visible, point-like γ-ray source.

4.1.1. Data selection

In a first step data that contains no detected γ-ray source was identified. The aim was to create the largest possible data set. The MC are tuned to different observation conditions. Therefore data was chosen from longest stable observation period to maximize the amount available. The period lasted from November 1st, 2009 to June 1st, 2011. For that period, all undetected targets below 32° zenith were identified. Additional requirements for the

data were that they had been taken using settings for extragalactic observations and with an offset of at least 10° from the galactic plane in galactic coordinates. The observations are given in Tab. 4.1, the highlighted targets are in the southern hemisphere, the others are in the northern sky. Their distribution in the sky is shown in Fig. 4.1 using galactic coordinates. The greyed out regions describe the part where observation exceed a zenith angle of 32°. These regions can not currently be used for the diffuse method, as the Monte Carlo simulations needed for the background estimation do not exist for this zenith range.

From that all the sources in the northern hemisphere were removed, as was explained in section 3.4.

source	Ra Dec	redshift	obs. length	zenith	azimuth
1FGL J2347.3+0710	$23^h47^m19.9^s$ $7°10'26''$	n/a	8.8 h	21° to 30°	140° to 230°
1FGL J0338.8+1313	$3^h38^m52.9^s$ $13°13'53''$	n/a	10 h	20° to 30°	180° to 240°
Segue 1	$10^h7^m4^s$ $16°4'55''$	n/a	28 h	13° to 32°	110° to 240°
3c454.3	$22^h53^m58^s$ $16°8'54''$	0.859	4 h	13° to 31°	200° to 250°
BLlac	$22^h0^m39.4^s$ $42°2'8''$	0.068	2 h	20° to 31°	30° to 60°
4c55.17	$9^h57^m38^s$ $55°22'57''$	0.899	29 h	26° to 32°	330° to 30°
Swift J1644+57	$16^h44^m50^s$ $57°34'59''$	0.35	14 h	29° to 32°	330° to 30°
1ES 2321+419	$23^h23^m52^s$ $42°10'58''$	0.05	3 h	12° to 32°	0° to 80°
MS1050.7+4946	$10^h53^m43^s$ $49°30'19''$	0.14	5 h	20° to 30°	300° to 360°

Table 4.1: Sources considered for the diffuse analysis, the highlighted section was eventually selected, while the rest was dismissed due to strong systematic effects in the northern sky.

The sources were analyzed using the standard point-source method to confirm that there is no signal seen from the observed position in the sky. This was done to avoid contamination from potential point-like γ-ray sources.

The resulting θ^2-plot for Segue 1 can be seen in Fig. 4.2a, and in appendix B for the remaining sources. Additionally sky maps were produced to ensure that the incoming cosmic rays were homogeneously distributed over the FoV and no part of the observed sky contributed significantly more than the rest. An example for Segue 1 can be seen in Fig. 4.2b, where the relative flux variation in the observed part of the sky is shown. It is worth noting that the relative flux variation scales with the total observation time. Therefore it is expected that sources with short observation time, such as 3c454.3 (Fig. B.3c), show more fluctuation than Segue 1 in Fig. 4.2b. Accordingly, it is also expected that

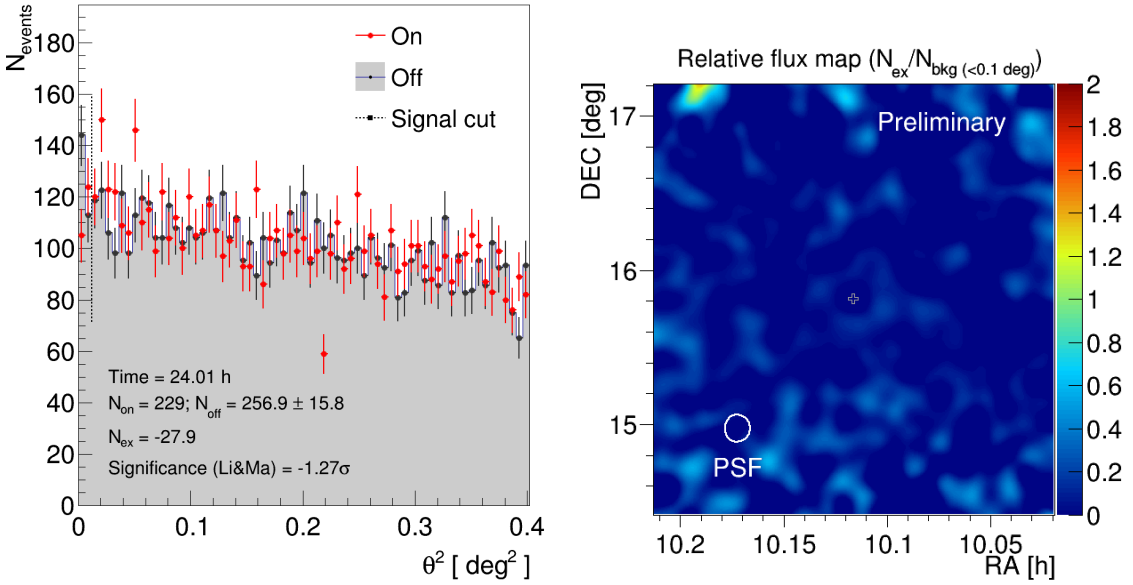

(a) Excess at the source position

(b) Sky map

Figure 4.2: θ^2 distribution and sky map of the Segue 1 observations

fluctuations occur mostly at the border of the field of view (and camera), as the total number of observed events is smaller. The fluctuations seen in the plots are negligible, incoming cosmic rays can be considered truly homogeneously distributed in the sky. The data can be used to calculate the diffuse electron spectrum.

The selected southern sources used for the diffuse spectrum are the ones highlighted in grey in Tab. 4.1. The reason for removing the northern sources is discussed in section 3.4. The applied quality cuts are the same as for the spectrum of the Crab Nebula and were given in section 3.3.2. They are listed here again for completeness:

- Zenith lower than 32°
- Humidity below 80%
- Cloudiness below 40
- Rates less than 15% above or below the average rate
- Size $>$ 100 PhE
- Leakage $<$ 0.2
- Islands $\leq$ 1
- MaxHeight circumference $<$ 4500 cm
- Difference in the reconstructed Disp between M1 and M2 $< (0.02°)^2$
- Squared distance of the shower center from the camera plane for M1 squared $< (1°)^2$

The background is estimated from MC proton simulations with a total of 11×10^6 events surviving at the final analysis level from 7×10^9 generated. The same cuts are applied to background and data.

4.1.2. Spectrum

The final spectrum was computed using 40 h of data and eleven million MC diffuse protons to simulate the background. The effective area was calculated using 200.000 MC diffuse electrons. The respective excess for each energy bin is given in Tab. 4.2.

<Energy> GeV	N_{on} #	N_{bg} #	Excess events #		significance σ
153.7	15152	11294	3857	±324	11.9
194.8	11163	8237.7	2925	±257	11.3
246.8	7947	4988.0	2958	±182	16.2
312.8	5573	3474.5	2098	±144	14.5
396.5	4231	2648.1	1582	±122	12.9
502.5	3074	1831.4	1242	±98	12.6
636.9	2322	1441.1	881	±84	10.5
807.2	1420	925.18	494	±63	7.86
1023	1112	926.75	185	±62	3.00
1296	811	592.66	218	±47	4.68
1643	502	386.81	115	±36	3.23
2082	366	274.68	91	±29	3.19
2639	275	227.07	48	±26	1.87
3345	158	135.51	22	±18	1.23

Table 4.2: Signal (N_{on}) and background events (N_{bg}) in the signal region for each energy bin in the analysis. As well as the number of excess events and the significance of the excess. The error of the excess stems from the uncertainty of the normalization defined in Eq. 3.7.

At the high-energy end the result is limited by the significance of the excess. Only points where the excess had a significance larger than 1 were kept. For low-energy the spectrum is limited by the energy threshold, determined by the user cuts applied. Without detector effects the surviving events should follow a power-law. There should be no peak in the distribution. However, in particular, the size cut affects low-energy events more strongly than high-energy events and causes for a much stronger suppression at low energies, creating a maximum. Above the threshold the cuts are expected to affect all energies equally. The fit of the true energy distribution is shown in Fig. 4.3. The resulting energy threshold is 131 GeV, meaning that any bins with energy lower than the first bin listed in Tab. 4.2 need to be discarded as well.

The data points of Tab. 4.2 are then used to unfold the spectrum, which will be done in the following section.

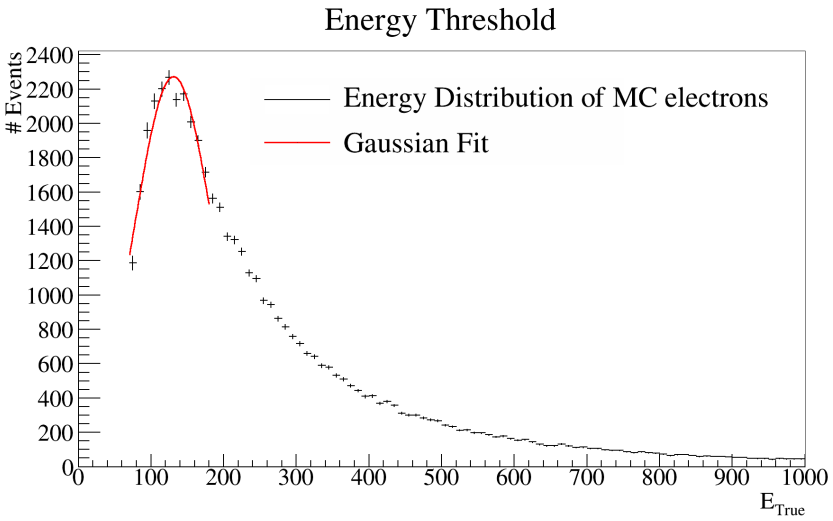

Figure 4.3: Distribution of the true energy of the MC electrons, the peak has been fitted with a Gaussian distribution to determine the energy threshold.

4.1.3. Unfolded spectrum

The spectrum was computed with the method presented in chapter 3. This spectrum is then unfolded to get the spectrum in bins of true energy and corrected for pile-up effects. The procedure was explained in section 2.4.3. The unfolding takes into account the assumed shape of the spectrum. Therefore several hypotheses were tested to compare the goodness of fit of the assumed spectral shape to the data. The spectral shapes were chosen based on prior knowledge from recently published spectra.

For the electron spectrum the two current interpretations are a broken power-law as seen by H.E.S.S.[34, 36] and VERITAS[169] or one can extrapolate the unbroken power-law seen by Fermi-LAT[21] and AMS-02[32] above 1 TeV.

The result obtained by MAGIC has been unfolded with several different regularization methods (as briefly explained in section 2.4.3). The resulting unfolded spectrum for the three main regularization methods using a simple power-law are shown in Fig. 4.4 with their resulting spectral index of the calculated fit. The resulting flux parametrizations are given below:

- $\frac{\mathrm{d}F}{\mathrm{d}E}_{\mathrm{Tik}} = (1.17 \pm 0.08_{\mathrm{stat}} \pm 0.47_{\mathrm{sys}}) \times 10^{-7} \times \left(\frac{E}{1\,\mathrm{TeV}}\right)^{-3.14 \pm 0.05_{\mathrm{stat}} \pm 0.5_{\mathrm{sys}}} \mathrm{GeV}^{-1}\,\mathrm{m}^{-2}\,\mathrm{s}^{-1}\,\mathrm{sr}^{-1}$
- $\frac{\mathrm{d}F}{\mathrm{d}E}_{\mathrm{Ber}} = (1.08 \pm 0.07_{\mathrm{stat}} \pm 0.43_{\mathrm{sys}}) \times 10^{-7} \times \left(\frac{E}{1\,\mathrm{TeV}}\right)^{-3.18 \pm 0.05_{\mathrm{stat}} \pm 0.5_{\mathrm{sys}}} \mathrm{GeV}^{-1}\,\mathrm{m}^{-2}\,\mathrm{s}^{-1}\,\mathrm{sr}^{-1}$
- $\frac{\mathrm{d}F}{\mathrm{d}E}_{\mathrm{Schmel}} = (1.17 \pm 0.08_{\mathrm{stat}} \pm 0.47_{\mathrm{sys}}) \times 10^{-7} \times \left(\frac{E}{1\,\mathrm{TeV}}\right)^{-3.14 \pm 0.05_{\mathrm{stat}} \pm 0.5_{\mathrm{sys}}} \mathrm{GeV}^{-1}\,\mathrm{m}^{-2}\,\mathrm{s}^{-1}\,\mathrm{sr}^{-1}.$

In a second step a broken power-law was fitted to the result with the same regularization methods. The formula for the broken power-law used is:

$$\frac{\mathrm{d}F}{\mathrm{d}E} = f_0 \times \left(\frac{E}{E_r}\right)^{\alpha_1} \left(1 + \frac{E}{E_0}^{\beta}\right)^{(\alpha_2 - \alpha_1)\beta} . \tag{4.1}$$

The parameters are the flux normalization f_0, the normalization energy at which the fit is normalized to the measured flux, E_r, the spectral index before the break, α_1, the energy of the break E_0, the spectral index after the break α_2 and the rigidity of the break β. The normalization energy E_r is not a free parameter, it was fixed to 500 GeV. The energy of the break was limited to the energy range which is covered by the measurement presented in this thesis: 150 GeV to 4500 GeV

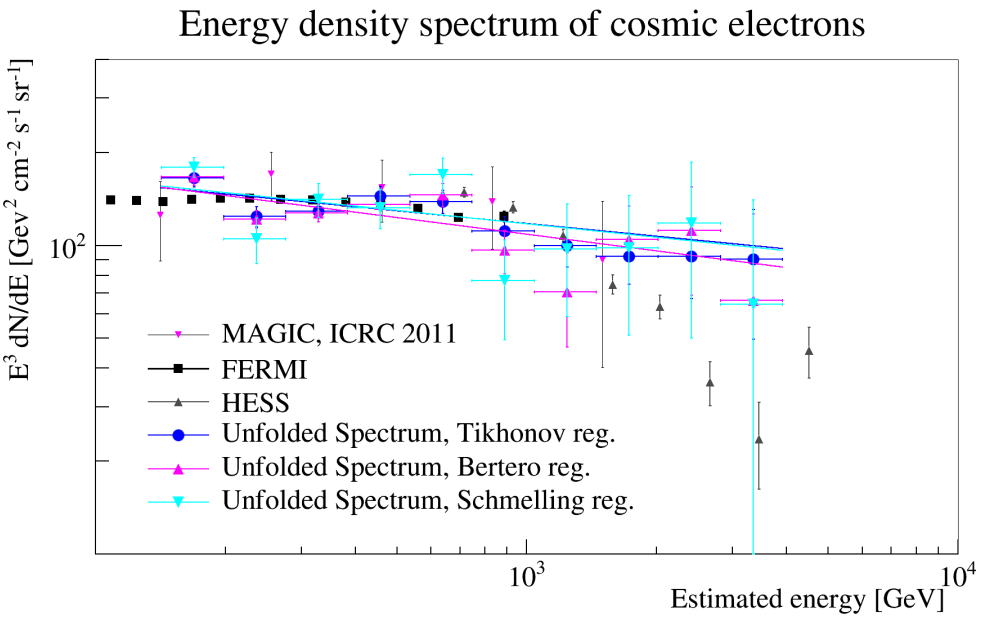

Figure 4.4: The unfolded energy density spectrum as measured by MAGIC, assuming a pure power-law.

The results are shown in Fig. 4.4, the resulting parameters of the different regularizations of the fit are given in Tab. 4.3:

Reg.	f_0 $\mathrm{cm}^{-2}\,\mathrm{s}^{-1}\,\mathrm{TeV}^{-1}$	β	E_0 TeV	α_1	α_2	$\frac{\chi^2}{\mathrm{dof}}$
Tikhonov	$(2.24 \pm 0.14) \times 10^{-9}$	9.4 ± 0.2	0.63 ± 0.20	-3.07 ± 0.08	-3.42 ± 0.26	$\frac{14.74}{5}$
Bertero	$(2.13 \pm 0.71) \times 10^{-9}$	3 ± 30	0.69 ± 0.59	-3.07 ± 0.19	-3.38 ± 0.63	$\frac{39.75}{5}$
Schmelling	$(2.25 \pm 0.15) \times 10^{-9}$	10.00 ± 0.02	0.63 ± 0.20	-3.06 ± 0.09	-3.42 ± 0.24	$\frac{14.70}{5}$

Table 4.3: Parameters of the broken power-law fit using different regularization methods.

The broken power-law fit shown in Fig. 4.5, over all, has a much worse reduced χ^2 ranging from almost 5 to 8. The reduced χ^2 of the pure power-law ranges from 0.99 to 2.1. The pure power-law is a better fit and preferred over the broken power-law for the spectrum measured in this thesis, contrary to the results presented by H.E.S.S.[34, 36] and VERITAS[169].

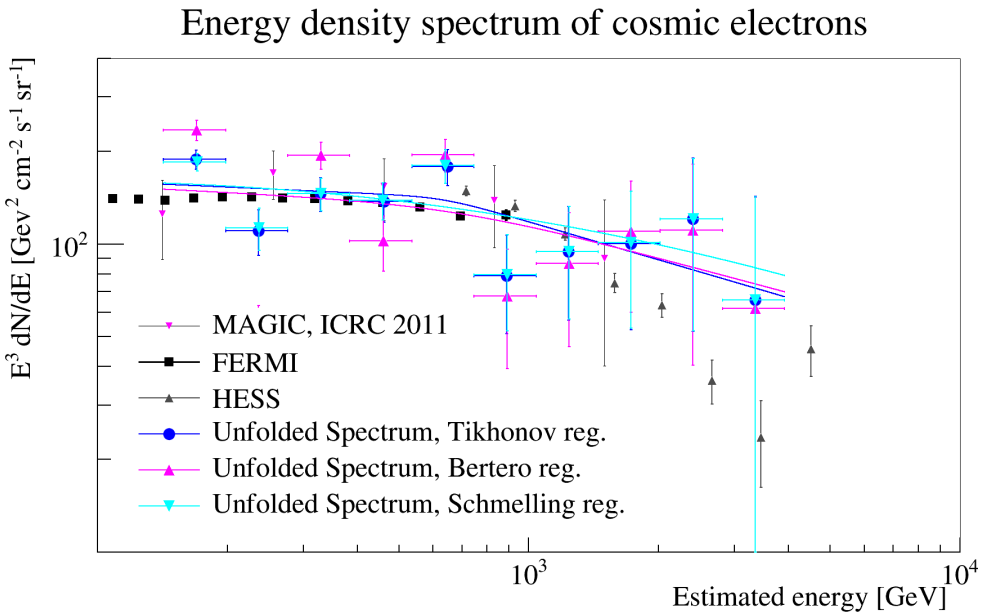

Figure 4.5: The unfolded energy density spectrum as measured by MAGIC, assuming a broken power-law.

4.1.4. The cosmic electron spectrum

The final spectrum is shown in Fig. 4.6. The arrow shows the systematic uncertainty of the flux normalization, quantified in chapter 5.

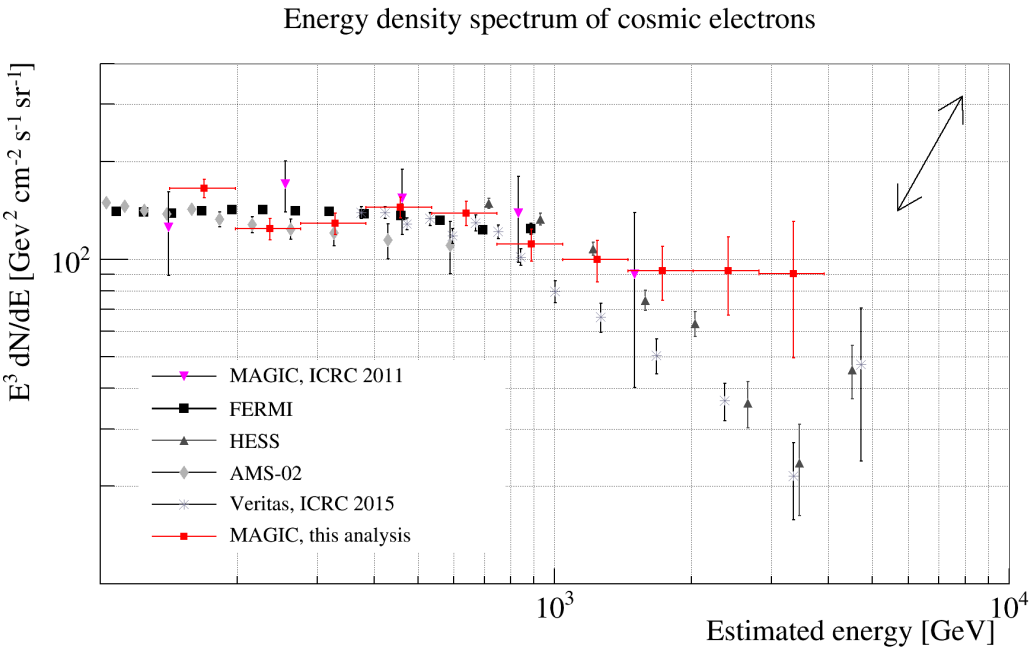

Figure 4.6: The electron spectrum as measured by MAGIC

4.2. Interpretation

The spectrum obtained in this thesis agrees well with a single power-law in the range from 130 GeV to 4000 GeV with a slightly steeper index than the ones previously determined by Fermi-LAT[21] and AMS-02[32]. With the larger data sample, the bump seen by MAGIC around 600 GeV[66] is reduced and there is no longer a feature in the spectrum. The MAGIC measurement shows no steep cutoff at high energies, contrary to the measurements published by VERITAS[169] and H.E.S.S.[34, 36]. The discrepancy is greatly reduced if one takes into account the systematic uncertainties, nevertheless some tension remains.

Due to the large uncertainties on the spectral index, no compelling argument can be made about the cutoff. However, the method shows a clear detection of electro-magnetic showers. Whether these showers stem from γ-rays or electrons can not be determined experimentally by this analysis method, but to the best current understanding the possible sources of γ-rays can be ruled out:

- The most obvious one, would be the γ-rays stemming from the observed source. As previously mentioned, a standard analysis was performed on the data and no excess coming from the source was detected. Several cuts were tested for the direction reconstruction, to rule out extended sources as well. It is unlikely that this is causing the excess measured by the diffuse analysis.
- Similarly the excess could come from an undetected source within the field of view observed. To rule this out, the sky maps were produced, showing no preferred origin of the γ-like signal. Additionally the flux observed below 1 TeV exceeds the flux of the Crab Nebula, as given in Tab. 3.2. A source of this magnitude would not go undetected in the standard analysis.
- The signal could also come from diffuse extragalactic γ-rays, but as shown in Fig. 1.5, the flux of diffuse extragalactic γ-rays can only account for about 1 – 10% of the total flux measured.

Therefore the signal observed, truly are cosmic electrons and MAGIC clearly confirms the excess of very-high-energy electrons over the expected flux of primary electrons from SNR and secondaries.

As discussed in section 1.3 the excess is likely coming from close-by sources such as SNR or pulsars. Possible contributions from specific pulsars were discussed in [119]. As can be seen in Fig. 4.7 the measurement presented in this thesis is in good agreement with one of the proposed models at high energies. The model assumes a diffusion coefficient of $D_0 = 2 \times 10^{29}\,\mathrm{cm^2\,s^{-1}}$ and an energy cutoff at 10 TeV. Kobayashi splits the electron and positron into two components: distance sources and nearby sources. The distant sources are all electrons and positrons reaching the Earth with an age over 10^5 yr or from a distance of more than 1 kpc, while the nearby pulsars are simulated individually.

4.3. Extending the spectrum in energy

With regards to the origin of the cosmic electrons, no conclusive evidence has been reached. H.E.S.S. sees indications for a second break at 12 TeV[36]. This would be considered a

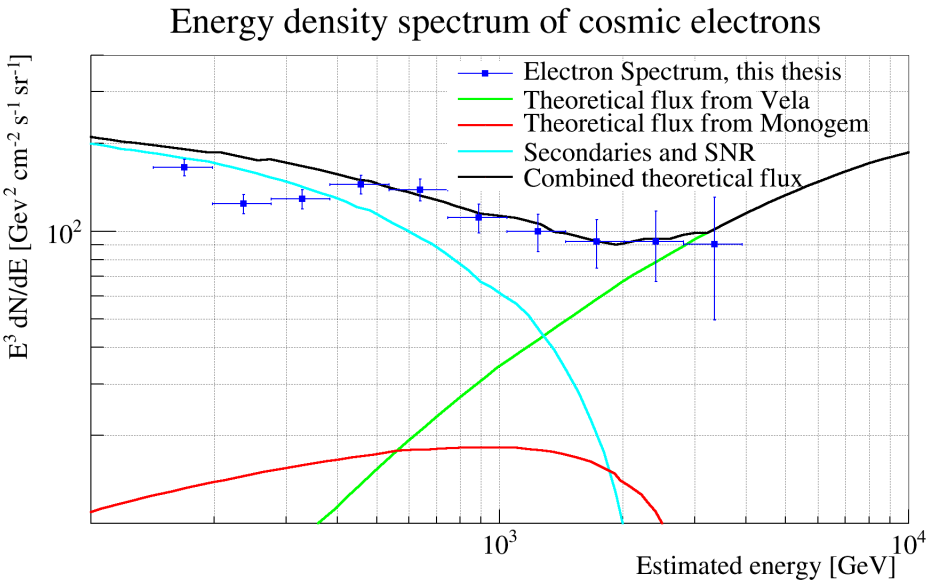

Figure 4.7: The measurement presented in this thesis compared to one theoretical model taken from [119], assuming a diffusion coefficient of $D_0 = 2 \times 10^{29}\,\mathrm{cm^2\,s^{-1}}$ and an energy cutoff at 10 TeV. The flux of secondaries also contains electrons and positrons reaching the Earth from distant sources with an age over 10^5 yr or from a distance of more than 1 kpc.

strong support of the pulsar theories, as it can easily account for several peaks caused by the different nearby pulsars. A double-peal would be much harder to explain in the context of DM.

4.3.1. High zenith analysis

A possible way to extend the current analysis and probe this energy range is to extend the analysis to larger zenith angles. By extending the analysis to larger zenith ranges, one collects events that are more absorbed by the atmosphere before reaching the telescopes.The effective area increases with the zenith angle, allowing also for higher energy events to be collected. On the down-side the energy threshold increases with energy and the reconstruction quality suffers. Last and not least, the computation of MC simulations for larger zenith angles is much more time and resource consuming.

As the method shown in this analysis already suffers from large systematic uncertainties, the analysis at large zenith angles was deemed unpromising and not performed, however, this is something that might be of interest to future studies of this type.

4.3.2. The IACT in the future: CTA

The next generation of Cherenkov telescopes is about to start operating. The ground-breaking ceremony for the CTA[1] north-array was celebrated in 2015 and the array is expected to be operational by 2020. The CTA will consist of a total of > 50 telescopes[25].

[1] www.ctaobservatory.org

The uncertainties in the analysis presented in this thesis largely stem from uncertainties in the reconstruction of the 3D shower parameters. They are believed to be caused by the asymmetry of the stereoscopic system. Adding more telescopes should reduce and even render irrelevant these uncertainties.

In addition CTA, covering a much larger effective area, is expected to have an energy range of up to 100 TeV[25]. This would mean that the next generation of Cherenkov telescopes can push the current measurements to even higher energies, well beyond the expected precision measurement of CALET. CALET hope to provide a precision measurement of the electron spectrum up to 20 TeV by 2020[178].

5. Systematic uncertainties

To complete the measurement of the diffuse flux, a detailed study of the systematic uncertainties was performed and the total uncertainty quantified. This takes into account, both the general uncertainties affecting data taking of the MAGIC telescopes already published[41] (where applicable) and specific uncertainties only affecting this particular analysis method. The study performed concentrated on the excess calculation since the uncertainty of the effective area, effective time and energy are essentially identical to the ones of the point-source analysis and are accounted for in [41]. The uncertainty in the excess calculation comes from three potential sources: a) fluctuations in the background simulated by MC, b) time or location depending variations in good-weather data and c) variations in the detector acceptance.

5.1. Background and background normalization

The tests described in this section were performed on a selection of good weather data taken on the Crab Nebula to avoid contributions from other effects, such as bad weather, to the uncertainties. The Crab Nebula is known as a standard candle, meaning that no fluctuation in flux or spectral index have been observed for the energy range of the imaging atmospheric Cherenkov telescopes.

The analysis was performed on the sub sample with a zenith angle lower than thirty-two degrees of the data used for the performance paper[41]. The full available MC sample was used for the studies. The MC sample from which the background is estimated, is much smaller than the data sample. To account for the difference, the background is scaled to the data in what is called the 'normalization region'.

Any variation observed will therefore be due to the analysis method or the background sample, allowing for a quantification of systematic shifts and uncertainties. The background estimation contains three potential sources of uncertainty: The MC sample used for the background, the normalization factor used to scale the MC to the data and last the signal region, which is the region in which the electron excess over the simulated MC proton background is calculated.

In this section several sources of uncertainties coming from the background and its normalization will be studied: statistical fluctuations in the generated MC protons, as the MC sample is much smaller than the data sample due to computing limitations. The effect of the scaling region chosen to determine the scaling factor defined in Eq. 3.7, the effect of the signal region chosen for the analysis.

5.1.1. Normalization region - Scaling

The normalization region is chosen in the region where protons are expected to dominate in the data. This excludes the region with very low hadronness, where the gamma-like events

are expected to pile up. It also excludes the hadronness values close to 1 as a significant contribution from muons and heavier elements is expected there. The contribution of electrons and muons to data between 0.4 and 0.8 in hadronness is expected below 10%. To estimate the effect of the normalization range chosen, two tests were performed: one reducing the width of the normalization region from almost 0.5 in hadronness to only 0.1, the other checking the position of the region from 0.4–0.75 up to 0.6–0.95 in hadronness. The calculation of the norm is explained in section 3.3.1, the error of the norm is calculated using error propagation and is simplified to:

$$\begin{aligned}\left(\frac{\sigma(\text{NormProtons})}{\text{NormProtons}}\right)^2 = &\left(\frac{\sigma_{N_{\text{norm,tot}}}}{N_{\text{norm,tot}}}\right)^2 \cdot \frac{N_{\text{sig, MCe}}}{N_{\text{sig,Mce}} + N_{\text{norm,MCe}}} \\ &+ \left(\frac{\sigma_{N_{\text{sig,tot}}}}{N_{\text{sig,tot}}}\right)^2 \cdot \frac{N_{\text{norm, MCe}}}{N_{\text{sig,MCe}} + N_{\text{norm,MCe}}} \\ &+ \left(\frac{\sigma_{N_{\text{sig,MCe}}}}{N_{\text{sig,Mce}}}\right)^2 + \left(\frac{\sigma_{N_{\text{norm,MCp}}}}{N_{\text{norm,MCp}}}\right)^2\end{aligned} \tag{5.1}$$

Where sig and norm reference the signal and normalization region in the hadronness distribution, respectively. So $N_{\text{sig,tot}}$ describes the number of total events in the data, $N_{\text{sig,MCe}}$ the number of MC electron signal events in the signal region, and $N_{\text{sig,MCp}}$ the simulated background proton events in the signal region. N_{norm} describes the number of events in the normalization region accordingly.

	mean E-bin [GeV]	127.1	172.7	234.8	319.2	433.9	589.8	801.8	1089	1481	2014	2737	3721
a)	Scale factor	24.48	26.27	27.91	29.25	28.44	32.86	36.48	37.55	37.89	35.47	38.56	41.85
	Error	0.48	0.57	0.70	0.86	0.97	1.24	1.50	1.69	1.92	2.00	2.42	2.97
b)	Scale factor	24.22	25.87	27.32	29.90	27.38	32.42	36.17	37.38	37.37	33.37	37.46	40.14
	Error	0.51	0.61	0.75	0.98	1.06	1.39	1.69	1.91	2.17	2.19	2.65	3.20
c)	Scale factor	23.71	25.18	26.83	29.61	27.26	32.28	35.47	37.34	37.03	32.31	37.50	42.13
	Error	0.54	0.65	0.84	1.11	1.21	1.59	1.89	2.21	2.46	2.46	3.00	3.73
d)	Scale factor	23.20	23.72	27.23	29.52	26.56	31.97	35.61	37.19	35.03	34.14	38.99	39.40
	Error	0.61	0.72	1.00	1.32	1.43	1.91	2.29	2.68	2.88	3.09	3.69	4.35
e)	Scale factor	23.08	23.01	27.56	29.78	26.49	30.74	38.84	37.64	33.39	31.60	34.84	47.70
	Error	0.85	0.99	1.45	1.96	2.11	2.77	3.57	3.98	4.21	4.35	5.05	7.26

Table 5.1: Norm factors and their statistical uncertainty for each energy bin from a set of different normalization regions: Sample a) was normalized in the range 0.4–0.9 in hadronness, b) in the range 0.45–0.85, c) in the range 0.5–0.8, d) in the range 0.55–0.75 and e) in the range 0.6–0.7.

Varying the width of the normalization region Reducing the normalization region leads to a larger error in the scaling factor, as is to be expected. The scaling factors and their error are given in Tab. 5.1 for five different normalization regions going from a range of 0.5

in hadronness to only 0.1. The first thing to note is that the smaller the normalization region, the larger the error on the scaling factor. For this reason, the smallest normalization regions are not a good choice. Otherwise, varying the width of the normalization region between 0.5 and 0.3 (cases a –c in Tab. 5.1) does not alter the normalization factor above 150 GeV within its error. Below 200 GeV the spread is getting more significant, in particular for the smallest normalization regions (cases d and e) and can cause a mismatch of up to 10% in the number of excess events. As the measurement of the electron flux does not extend to such low energies, however, this mismatch is not affecting the measurement. It should be kept in mind though, in case of future attempts to extend the measurement to even lower energies.

The error on the scaling factors starts to increase rapidly above 1 TeV. This can also be seen in Fig. 5.1, where the resulting spectra of the Crab Nebula for the cases a-e from Tab. 5.1 have been plotted. At 3 TeV a deviation from the published Crab Nebula spectrum of 20% for the smallest normalization ranges can be seen.

The normalization range should be kept larger than 0.3 ideally even if 0.25 is also acceptable. The error of the scaling factor is propagated to the error of the events in the off region and thereby also into the error of the excess calculation. This is also illustrated by the fact that the resulting spectra from the Crab Nebula match within the errors in Fig. 5.1 and that the error bars are larger for the spectra calculated with the smallest normalization region. This does not contribute significantly to systematic uncertainties in this analysis as the analysis is not sensitive to energies below 150 GeV, but would contribute to a systematic shift to higher flux levels at energies below 100 GeV to 150 GeV.

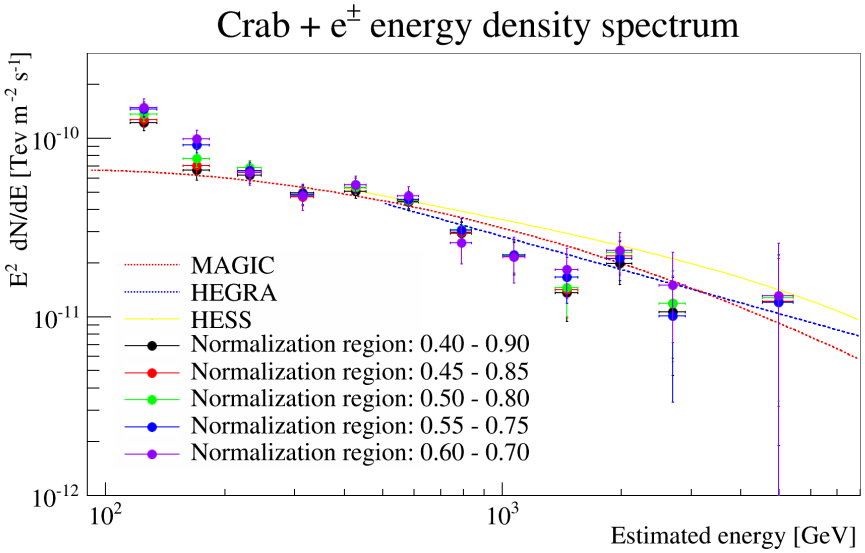

Figure 5.1: Effect of varying the size of the normalization region on the final Crab Nebula spectra from 0.1 to 0.5 in hadronness.

Position of the normalization region Varying the position of the normalization region over the range in which it is possible to normalize the data to the MC (roughly speaking 0.3–0.9) gives an estimate of how strongly the position of the normalization range affects

the final result. The width of the normalization region was chosen to be 0.35 which is well above the previously determined lower limit of 0.2 and then moved in steps of 0.05 from 0.35–0.7 to 0.5–0.85. The resulting scaling factor and their errors can be found in Tab. 5.2. The resulting scaling factors are consistent with each other within their errors above 150 GeV. A comparative plot of the Crab Nebula spectra calculated using different normalization ranges is shown in Fig. 5.2. The spectra match well above 150 GeV and show the same kind of mismatch at low energies as noted before. Therefore the same conclusion holds true as in the previous section and it can be said that the rescaling of the MC is not introducing any significant systematic uncertainties or shifts for the results presented in this thesis. Given the statistical errors on the high-energy points, the systematic uncertainty on the flux normalization were determined to be below 5% and the uncertainty on the spectral index less than 0.05.

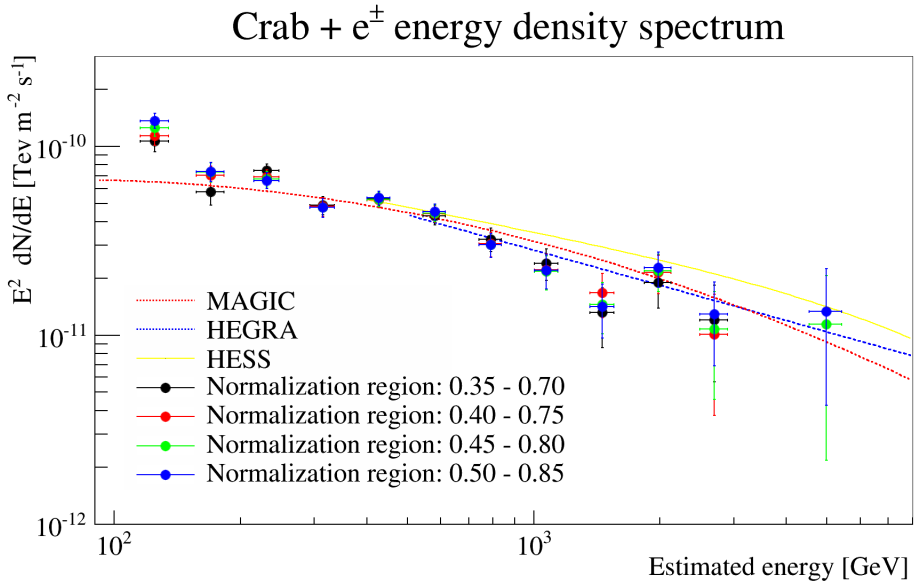

Figure 5.2: Effect of varying the normalization region over the range from 0.35 to 0.85 in hadronness on the final Crab Nebula spectra.

5.1.2. Fluctuation in the MC

To estimate the fluctuation and variation in the MC protons, the sample was split into three separate samples based on the "production sites". These samples were produced independently, by different people using similar, but distinct input cards. A comparative list of the input parameters can be found in Tab. 5.3, the two productions from Garching are grouped into a single production as their sample size is quite small. The differing parameters are the zenith range covered by the production, the maximum distance between the shower impact point and the telescopes as well as the maximum angle a shower can have with respect to the camera plane. They reflect the recommended parameters for MC production within the collaboration at the time of production.

	Mean E-bin	127.1	172.7	234.8	319.2	433.9	589.8	801.8	1089	1481	2014	2737	3721
a)	Scaling factor	25.32	25.96	25.94	29.00	28.01	32.55	35.51	35.82	36.65	34.75	36.58	39.71
	Error	0.55	0.62	0.73	1.02	1.17	1.57	1.90	2.12	2.45	2.58	3.02	3.71
b)	Scaling factor	24.91	25.88	26.72	29.59	27.75	32.72	35.64	37.17	34.93	33.79	39.00	38.86
	Error	0.54	0.63	0.77	1.05	1.17	1.56	1.87	2.15	2.33	2.50	3.06	3.55
c)	Scaling factor	24.30	25.58	27.01	29.76	27.50	32.59	35.86	37.48	37.00	33.38	38.43	40.04
	Error	0.52	0.62	0.77	1.03	1.12	1.49	1.79	2.05	2.30	2.35	2.88	3.40
d)	Scaling factor	23.69	25.55	27.21	29.79	27.15	32.14	35.87	37.25	37.44	32.50	36.57	41.91
	Error	0.52	0.64	0.81	1.05	1.13	1.47	1.78	2.03	2.29	2.26	2.73	3.45

Table 5.2: Norm factors and their uncertainty for each energy bin from a set of different normalization regions: Sample a) was normalized in the range 0.35–0.7, b) in the range 0.4–0.75, c) in the range 0.45–0.8 and d) in the range 0.5–0.85.

The resulting hadronness distributions are in very good agreement with each other. The biggest difference between the three productions is their sample size. This can also be seen in the comparison of the resulting Crab Nebula spectra from the three productions as shown in Fig. 5.3. The spectra all match in the main energy region, the smaller production (from Dortmund) does not have enough statistics to estimate the background in high energy bins. Therefore the third spectrum is less extended than the spectra with the other samples.

Production	Energy	Zenith	Maximum impact	view cone	# of events
Garching 1	70 GeV to 20 TeV	8° to 38°	1200 m	6°	7.4×10^5
Garching 2	70 GeV to 20 TeV	4° to 36°	700 m	6°	1.9×10^6
Dortmund	70 GeV to 20 TeV	4° to 36°	700 m	4°	1.1×10^6
Zeuthen	70 GeV to 20 TeV	5° to 35°	700 m	4°	9.9×10^6

Table 5.3: List of the key parameters changing in the different MC productions of protons.

To estimate the effect of the background on the final spectra, the MC sets were split into several sub-samples. For each subsample, an analysis of the fluctuation in the resulting hadronness distribution, as well as the resulting spectra of the Crab Nebula was performed. The resulting spectra were compatible within their statistical error bars allowing the conclusion that no systematic uncertainty needs to be attributed to the simulations. From the statistical errors of the flux parametrization, it was concluded that the systematic uncertainty of the flux normalization was below 2%.

5.1.3. Efficiency cut - Determining signal region

The signal region is defined separately for each energy bin as the hadronness region, $0 \leq h \leq h_{max}(x)$ in which x % of the MC electrons are contained. In the following x and $h_{max}(x)$ are referred to as efficiency cut. For low energy events, differentiating between

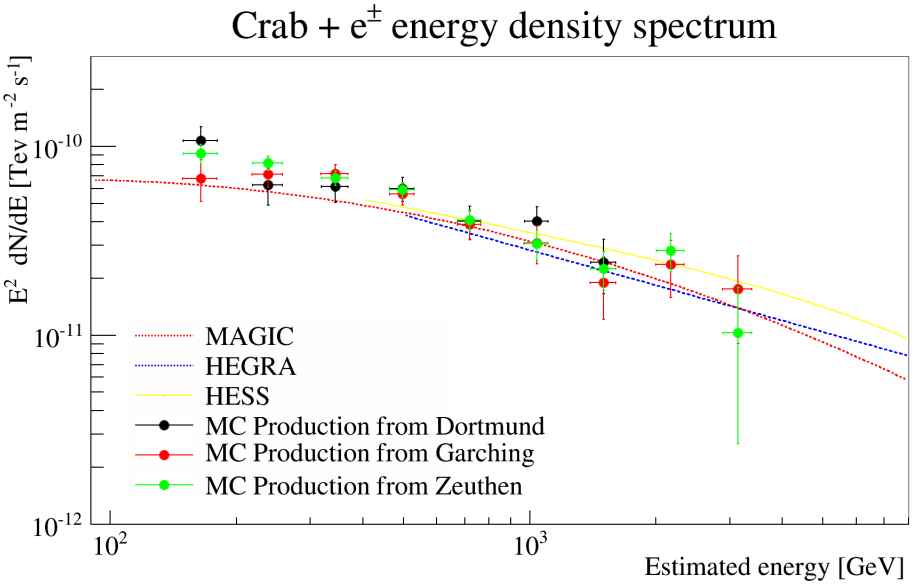

Figure 5.3: The different colors show the different MC productions used as background for the calculation of the flux. The different parameters used for the productions are summarized in Tab. 5.3.

protons and electrons is harder than for the range around 1 TeV. For low, and very high, energy bins the cut will often be around 0.3 in hadronness, while it is reaching 0.15 in the bins around 500 GeV to 1 TeV where the random forest is most effective. The signal region chosen may influence the final result and to understand in which way this affects the final result, the efficiency was varied from 60% to 90%. This realistically covers the entire possible range of cuts for the diffuse analysis as a minimum size of 0.15 is required in the analysis to allow for enough statistics to reliably calculate the excess and the maximum size of the signal region is limited by the size of the normalization region, as the two are not allowed to overlap. The normalization region was chosen to be 0.6 – 0.85. This allows for a potentially large signal region, needed to contain 90% of all MC electrons. The variation in the efficiency cut shows fluctuations, particularly at higher energies as can be seen in Fig. 5.4. The effect is roughly 2–3% below 1 TeV, but rapidly increases to 20% at 3 TeV. The fluctuations at high energies are not a systematic shift, so that the spectral index should not be biased. However, the fact that it only affects the high energy bins means that it affects the spectral index determination. The total effect is less than 0.05 in the power-law index and roughly 5% for the flux normalization.

All in all this leads to the overall uncertainty stemming from the background estimation being below 10%. This may sound surprising if one considers that the systematic uncertainty of the background is quoted at 1–2% for strong sources and up to 20% for weak sources in [42, 70]. However, the uncertainty of fluctuation in the diffuse flux of cosmic rays is quantified as a systematic uncertainty of the background in the point-source analysis. while it is considered as a systematic on the excess events for the diffuse analysis presented in this thesis, since the background is simulated. Therefore the fluctuations of the diffuse

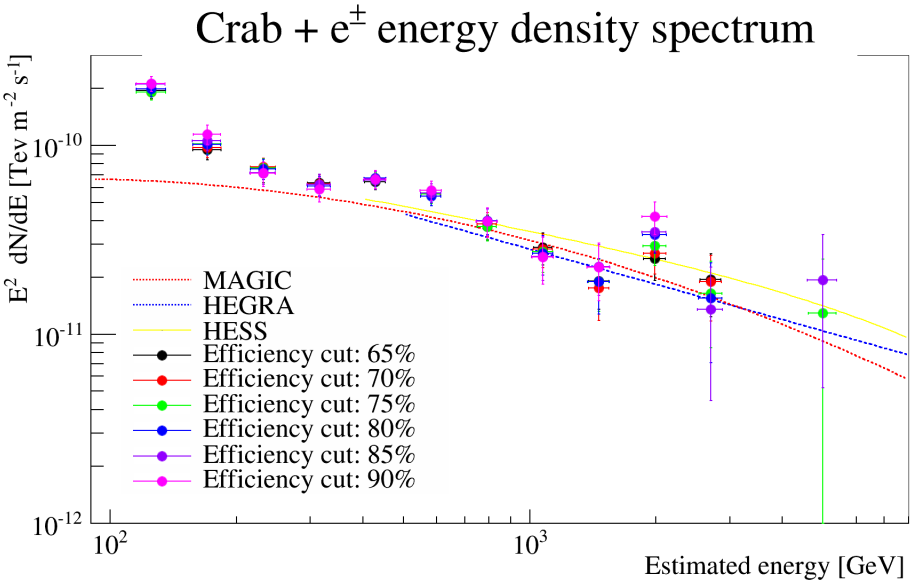

Figure 5.4: The effect of changes in the cut efficiency on the final spectra, this is used to determine the overall fluctuation due to the definition of the signal region.

cosmic rays will be accounted for in the uncertainties of fluctuations in the data, which will be quantified in section 5.2.

5.2. Systematic effects in the data

The largest uncertainties come from fluctuations in the data. A first attempt at minimizing fluctuations was already described in the previous chapters: by doing a careful selection of weather conditions and data quality, fluctuations were reduced as much as possible. However, strong fluctuations still remain. Some are related to the detector set up and others are possibly related to the observation conditions or unknown causes. A simple approach to quantify the uncertainty in the spectrum is to subdivide the data into random subsample and check how strongly the resulting spectrum varies. This can be seen in Fig. 5.5. The gray points are previous publications of the electron spectrum for reference. The blue points are the different subsamples of the data set used for calculating the electron spectrum. The flux normalization varies by almost a factor 2, the resulting spectral index varies by 0.3 if one assumes a pure power-law.

The uncertainty due to the hadronness fluctuation is quantified here, while the possible origin of the variation was evaluated in section 3.4. The MaxHeight is the strongest discriminator between hadronic and γ-like showers in the Random Forest. In a first attempt to reduce the uncertainty, the fluctuating parameter was removed from the hadronness training, to see if the resulting hadronness would be stable over time. For this, the spread of the hadronness was analyzed. The hadronness distribution from different nights were normalized and a mean number of events per hadronness bin was calculated. The deviation was then compared once for a hadronness trained on the MaxHeight and once for a hadronness trained without the MaxHeight. This can be seen in Fig. 5.6. The

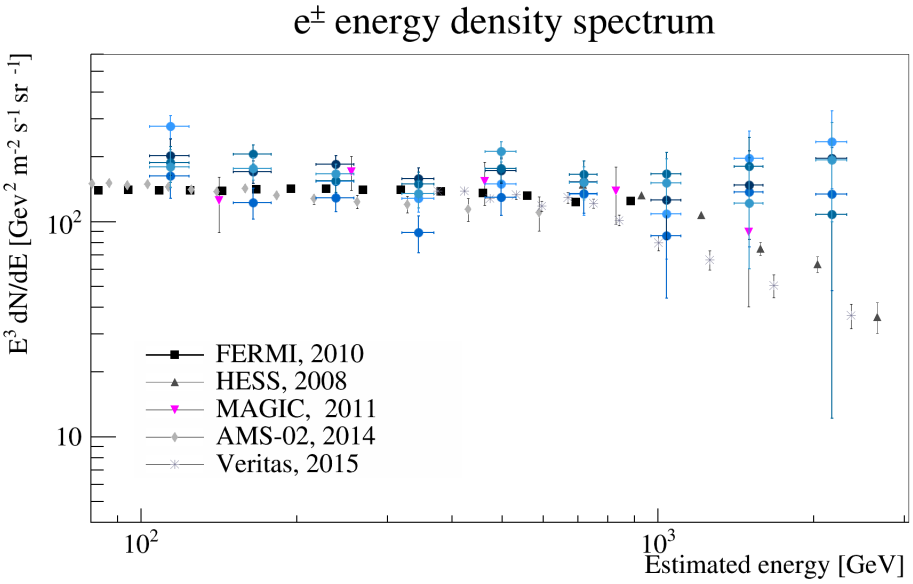

Figure 5.5: The resulting electron density spectra extracted from the data when divided into 5 subsamples.

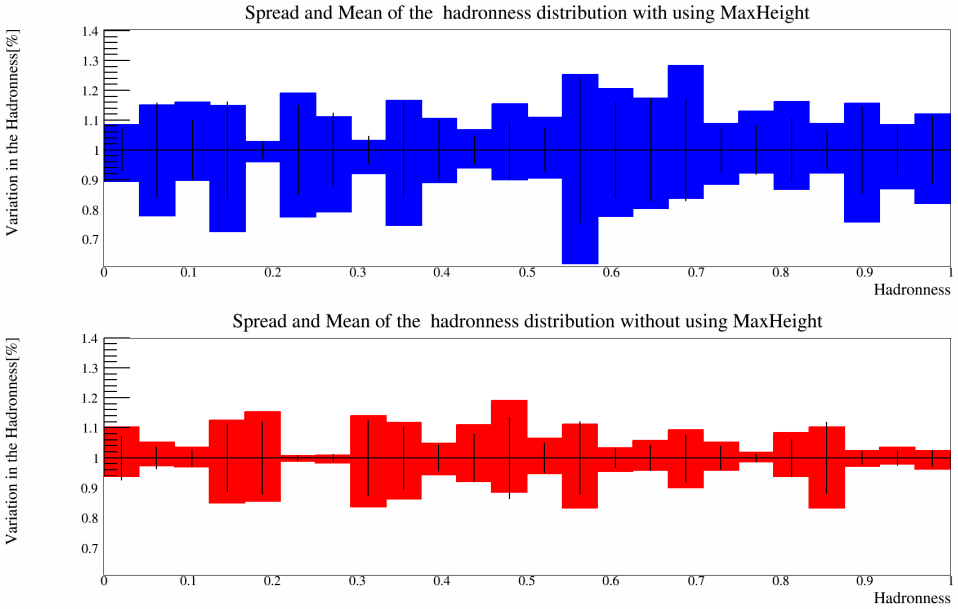

Figure 5.6: The spread in hadronness for different days in a single source. At the top using a training including the MaxHeight, at the bottom the hadronness was trained without the MaxHeight.

upper plot shows the spread for the hadronness trained with MaxHeight, the lower plot shows the spread for the hadronness trained without MaxHeight. The spread reduced from about 15% to 5–10% per hadronness bin. So the hadronness estimation without the MaxHeight is more robust, however, there is also a strong loss of sensitivity. This is shown in Fig. 5.7, the efficiency cut increases by almost 50%, in particular at low energies reaching almost 0.5 in hadronness. For this reason it was decided to keep the MaxHeight in the training. The fluctuations of the hadronness in the data are mostly synonymous with the fluctuations of the MaxHeight and therefore the uncertainty will be estimated from the fluctuation in the MaxHeight for the rest of this section.

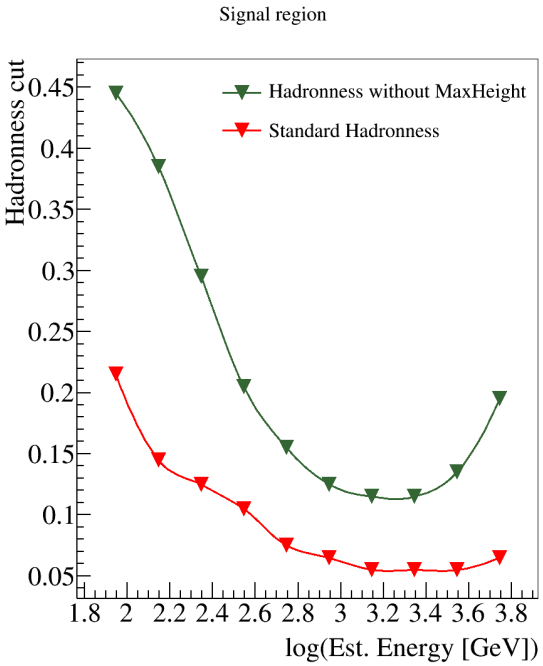

Figure 5.7: The upper hadronness cut containing 65% of the MC electrons as a function of energy. Red shows the signal region size using a hadronness trained using the MaxHeight, green shows the signal region using a hadronness trained without the MaxHeight.

5.2.1. Zenith dependence

To minimize the dependence the range in which the analysis is performed was limited to at most 32 degrees. Figure 5.8 shows the average MaxHeight in centimeter vs. the zenith angle in degrees between 0 and 32 degrees. There is a clear zenith dependence visible already at small zenith angles. This is to be expected as the MaxHeight is calculated as the absolute height rather than the distance along the line of sight between the shower maximum and the telescopes.

The dependence is not in itself problematic as long as it is correctly accounted for in the MC simulations. As can be seen by the red line in Fig. 5.8 the MC protons show the same evolution in zenith as the data and indeed the zenith effect is correctly accounted for.

The final analysis can also be done in multiple zenith bins, reducing the dependence to a negligible effect.

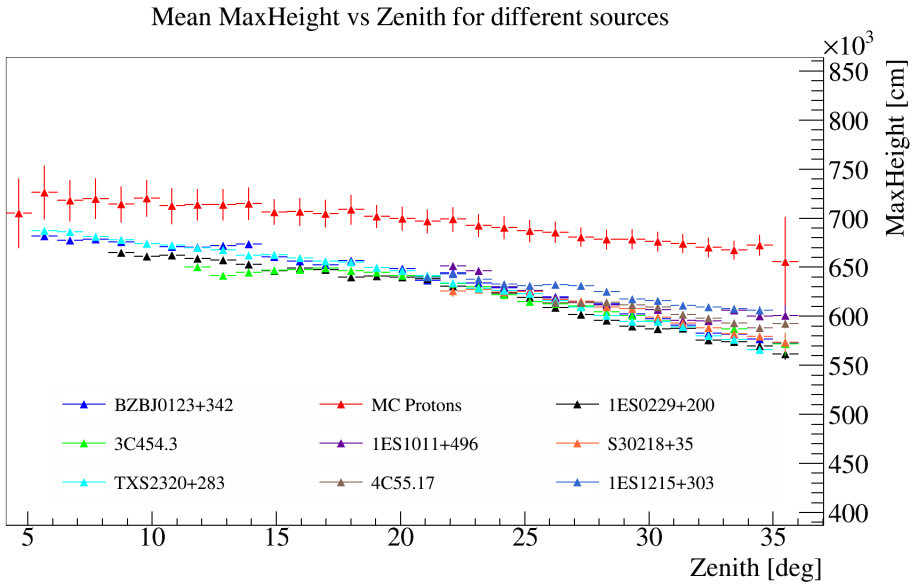

Figure 5.8: The average MaxHeight versus the zenith direction of the telescope.

5.2.2. Azimuth dependence

A dependence on the azimuth was discovered in some of the parameters reconstructed from the data, most importantly the MaxHeight. An independent study of data taken between 2013 and 2015 was performed to better understand this fluctuation.

For more details about the investigation of the azimuth dependence please see section 3.4. The final conclusion was that the northern sources systematically show a smaller MaxHeight, leading to a severe underestimation of the flux of about 50%. This is a strong bias, already alluded to in section 3.3.2 and 3.3.3. Using the point-source analysis of strong sources as a benchmark, it is possible to conclude that the diffuse method works well in the southern sky, where the Crab Nebula spectrum is reproduced correctly, as shown in Fig. 3.11.But the method fails to correctly reproduce the spectrum of Mrk501, a source in the northern sky, as shown in Fig. 3.13.

In addition the discrepancy also affects the spectral slope, as it seems to affect low-energy events more strongly than high-energy events. It was therefore decided to limit the analysis to a range in azimuth where the data and the MC production are in good agreement and the results of the point-source analysis could be reliably reproduced. This range is roughly equal to the southern hemisphere.

Even after carefully selecting only high-quality data in good agreement with the MC, fluctuations within the data set remain. For the point-source analysis, the background estimation is done from data that is taken simultaneously at a small offset in the camera. Fluctuations cancel out as they are present both in the signal and the background measurement. For the diffuse analysis the background is simulated and therefore does not

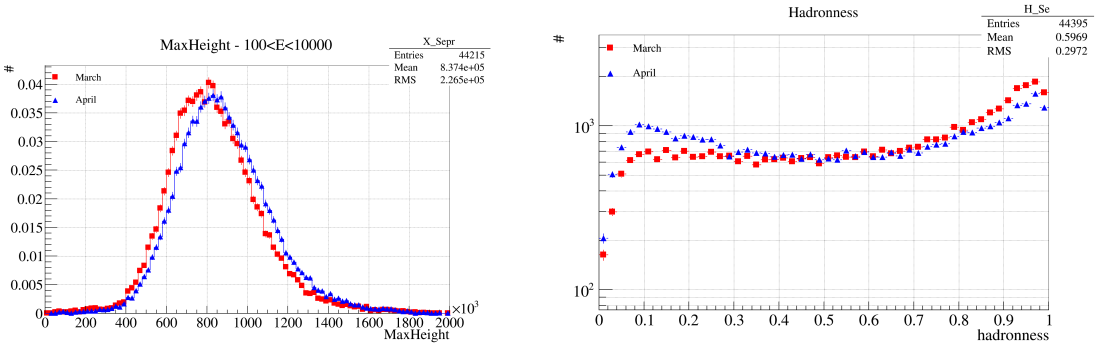

(a) Differences in MaxHeight

(b) Differences in hadronness distribution

Figure 5.9: Fluctuations in parameters of the same source taken two months apart in 2011. The red data was taken in February and beginning of March, the blue data was taken in April.

reflect daily fluctuations. This can lead to large uncertainties. The daily fluctuation is the single largest contribution to the uncertainty on the hadronness, which propagates to the excess calculation and thereby the total flux. As an example, Fig. 5.9a shows the variation in the MaxHeight and Fig. 5.9b shows the hadronness variation in a single source that are unaccounted for by bad weather or zenith and azimuth dependencies. The variation shown here results in 30% less events in the signal region, with the normalization factor almost unchanged. This propagates directly to the excess and the flux calculation as the flux is directly proportional to the excess. As a consequence, the resulting flux is underestimated by 30% for the February data (or overestimated in April). In addition, an energy dependence can be seen: The mismatch is largest at low energies and vanishes at high energies ($> 1\,\mathrm{TeV}$). This directly affects the reconstruction of the spectral index, whose uncertainty has been quantified to a value of up to 0.4, by comparing spectral slopes of different time spans of a single source.

5.3. Variation in the detector acceptance

In contrast to the point-source analysis, the events of the diffuse analysis are not centered on a single point but events distributed all over the camera plane are taken into account. Therefore a basic study of the detector acceptance was performed.

5.3.1. Decrease of sensitivity in the outer ring of the camera plane

As can be seen in Fig. 5.10, the hadronness distribution does not depend on the distance to the camera center within the previously mentioned cut of 1.5 degree from the camera center. However, in even more peripheral layers the situation is different (red distributions): a clear tendency towards more hadron-like events is visible, with the outermost ring having primarily events in the middle of the hadronness distribution. This has two reasons: first the events in the outer ring need to be large events, as the trigger region does not cover that area of the camera. The second reason is that the outer rings, as mentioned in section 2.2, are less precise than the center of the camera for M1. This means that the reconstruction

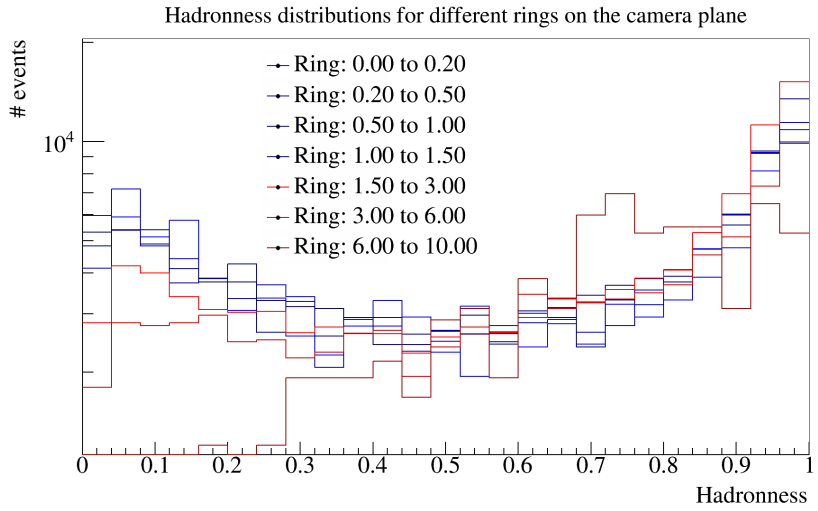

Figure 5.10: Hadronness distribution of events in different rings on the camera plane. The rings are chosen to contain roughly the same amount of events. The blue distributions are the ones that are within the cut applied on the distance to the camera center. The red ones are the distributions of the events that lie outside the cut.

of size and other parameters is less precise and an evaluation in terms of hadron-likeness becomes more difficult. Figure 5.10 shows that while there is a dependence on the distance to the camera in the hadronness distribution, the distance cut applied to the data removes the affected events.

5.3.2. Effect of the different pointing positions

The dependence on the pointing position is mostly due to the limited symmetry in the telescope setup. Many of these effects are known and accounted for in the point-source analysis. Basic cross checks were done for the diffuse analysis, to ensure that this holds true also for that.

The biggest concern is the so-called dead zone. When the two telescopes point in almost parallel directions, the buffer for the first telescope is not large enough to save the signal until the shower reaches the second telescope. The event gets overwritten before the second telescope is triggered. In the worst case no more events are triggered, in the less extreme cases the trigger rates decrease due to missed events. Extensive tests were performed on the sources to analyze the effect of the dead zone on the point-source analysis. The data affected by the dead-zone are removed by limiting the zenith to below thirty-two degrees. The pointing position of the telescopes and the dead zone regions are shown in Fig. 5.11. It can be seen that the high zenith data of Segue1, 4C55.17 and 1FGL J2347.3+0710 approach the dead zone region, without actually entering it. High zenith data from these sources could be affected by the dead zone, however, the high-zenith data is outside the scope of this analysis due to the lack of MC simulation for that zenith range.

The so called wobble-mode in which the data is taken ensures not only that the background is taken quasi-simultaneous with the data, but it also allows for the data to be taken

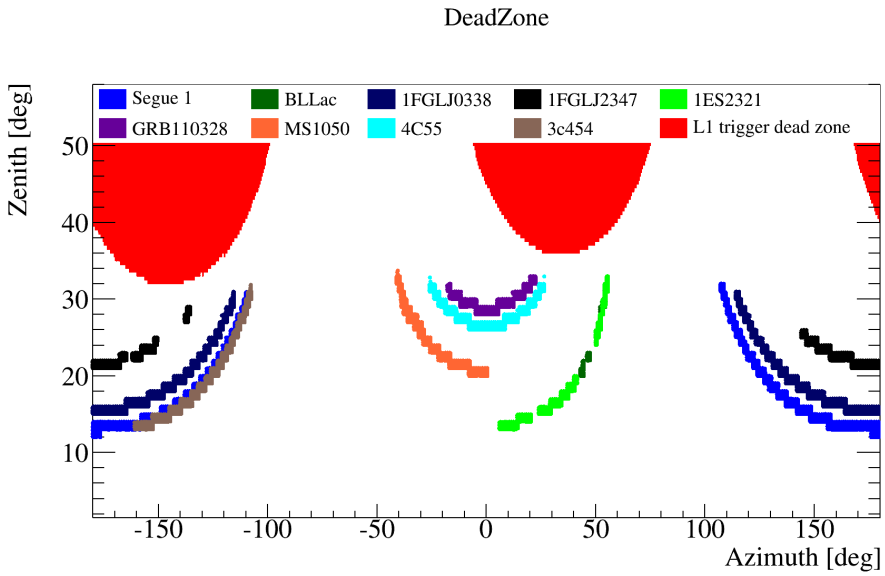

Figure 5.11: The red area shows the dead zone in which some or all events are lost, the remaining colors show the different sources used in the diffuse analysis. It can be seen that this analysis is not affected by the dead zone.

in the same part of the camera as the signal was taken. The wobble positions alternate so that the same amount of time is given to the source and the off-source position in the same part of the camera plane. Since the background is not measured in the diffuse analysis, this is not of particular relevance to the analysis.

However, the fact that only stereo showers, so showers that are triggered by both telescopes are kept, leads to a non-homogeneous distribution of the triggered events on the camera plane. This effect comes from the limited azimuthal symmetry of the telescopes and is called stereo-blob. It is most pronounced in a two-telescope system and was studied in detail in [170] for the point-source analysis. The conclusion was that the point-source analysis suffers from a systematic uncertainty of up to 10% of the background rate below 200 GeV due to the source position being at the outer limit of the stereo-blob for one wobble position, but not the other. This effect only affects the analysis if there is a source position, so the diffuse analysis is not affected by this. To confirm this, the data was split into the different wobble positions for each source and the resulting spectra were compared.

To test for acceptance variation in the camera, the camera plane was split into four parts. The separation was done along the x-axis and y-axis of a coordinate system with the origin in the center of the camera plane. For each quarter the flux was computed. The pull of the measured flux, $\left(\frac{x-\overline{x}}{\sigma_x}\right)$ was calculated for each energy bin. x is the flux at a given energy, $\overline{x}$ is the mean flux value at said energy, σ_x is the error of x.

The distribution of the pulls is shown in Fig. 5.12. The distribution has a central value of -0.1 ± 0.2 and the width of the distribution is 0.9 ± 0.2 showing no indication of systematic effects. The red curve shows the fit that was used to determine these values.

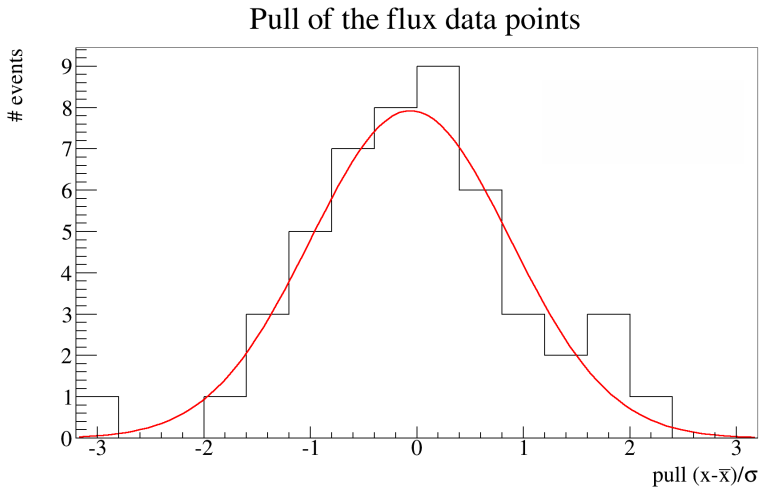

Figure 5.12: Pull distribution of the flux values for the different camera quarters.

5.4. Monte Carlo simulation and data matching

As the random forest is trained on MC and the background is completely estimated from MC, it is important that the MC match the data very closely. The full set of parameter distributions can be found in appendix A.

Several studies comparing MC and data were performed. In particular it was checked that the parameter distributions of data and MC protons match well. Areas where the data and MC did not match were removed using the user-cuts. It was also checked that the parameters have the same kind of energy dependence.

All these studies were performed in the hadronness range from 0.4 to 0.8, where the data is expected to be proton dominated and thereby mostly identical to the MC Proton. The MC data was re-weighted to have the same spectral index as the data and the quality cuts used in the analysis were applied. Notably a leakage cut of 0.2, an island cut of 1.5, a size cut of at least 100PhE and a cut limiting the distance to the camera center to less than 1.5 degree were applied. In addition the sample was decomposed into several energy bins to better see the matching.

First the distributions of each parameter were compared. A sample plot for the energy range 500 GeV to 800 GeV can be seen in Fig. 5.13a. After seeing that there was a satisfactory match between MC and data, the correlation of parameters with the image size was compared. As an example fig 5.13b shows the mean value of the MaxHeight vs. the size of the image on M1. This allows to see that the MaxHeight for MC and data match over the entire range of sizes. A full set of plots can be found in Appendix A. It was found that there are small mismatches between the size of M2 for data and MC. There are more large-sized events in the data than in the MC. This only affects the highest energy ranges, above 5 TeV, to which this analysis is not sensitive. It was also seen, that the length of the Hillas ellipse for M2 shows a slight mismatch at high energies, however, it is negligible in the sense that this parameter does not strongly contribute to the hadronness evaluation and the mismatch only shows at the highest energies. In general the matching between

data and MC is very good, so that no further cuts than the ones described in section 3.2 are needed.

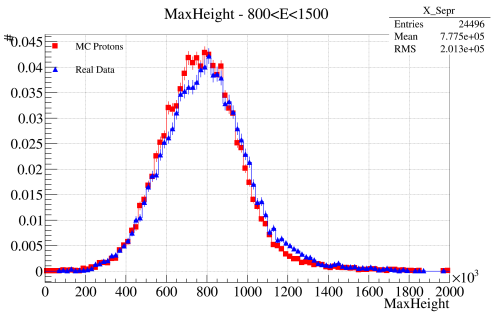

(a) Absolute MaxHeight distribution in the energy range 500 GeV to 800 GeV

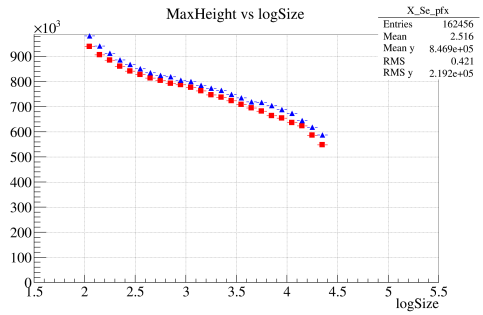

(b) Mean MaxHeight vs the Size of the Hillas ellipse for telescope M2

Figure 5.13: Comparison of MC protons and data.

5.5. Total uncertainty

The uncertainties for the measurement presented in this thesis are summarized in Tab. 5.4. The uncertainties are added quadratically to compute the total uncertainty: The uncertainty of the flux normalization is 47% if one excludes the data affected by the azimuth dependence, as was done in this thesis. The uncertainty on the energy estimation is 15%, the same as for the point-source analysis. The uncertainty on the spectral slope is of order 0.5. This means that this analysis is not sensitive to the break at 800 GeV mentioned in section 4.1.3.

As was pointed out in [36], there is also a systematic uncertainty of about 30% on the flux normalization due to the limited knowledge of the proton interactions in the air shower affecting this measurement.

Systematic effect	Uncertainty	
	Flux Norm	Spectral Index
charge flat-fielding	2-8%	
broken channels / pixels	3%	
NSB	1-4%	
trigger	1%	
unfolding of energy spectra		0.1
non-linearity of readout		0.04
Normalization region	$< 5\%$	< 0.05
MC fluctuations	$< 2\%$	
Signal region	5%	< 0.05
Data day-by-day fluctuations	$\sim 30\%$	0.4
Data-MC matching (averaged)	10%	0.1
Azimuth (removed from analysis)	50%	0.2
Source position in the sky (south only)	15%	0.1
Theoretical uncertainty in proton-proton interaction	30%	

Table 5.4: The table shows a summary of all systematic uncertainties affecting the diffuse analysis. The highlighted section is taken from [41], the second section is the summary of the uncertainties determined in this work. The theoretical uncertainty on proton-proton interaction is taken from [36]. FN stands for flux normalization and SL for spectral slope.

6. Summary

This thesis presents the results of my PhD studies. It investigates the origin of the very-high-energy electron excess above 100 GeV as measured by the satellite experiments. The excess is a smoking gun for a new class of electron accelerators such as pulsars or possibly dark matter. Due to the strong energy losses the very-high-energy electrons infer, these accelerators have to be close-by.

The main focus of my work was the development of the diffuse analysis, as well as the evaluation of the systematic uncertainties affecting the measurement. The method proved to be challenging as the arrival direction of the shower can not be used. This is the main discriminator between signal and background for the standard, point-source analysis normally performed with the MAGIC telescopes.

The diffuse analysis relies instead on the shape of the air showers to differentiate between electrons (or γ-rays) and hadrons (mostly protons). It does so by using a machine learning algorithm to evaluate the likelihood for a shower to be hadronic, the hadronness. Since the background can not be measured, it must be estimated from MC simulations of protons. These simulations had to be generated specifically for this analysis.

The diffuse analysis method was applied to several strong γ-ray sources as a proof of concept. This led to the discovery of an afore unknown azimuth dependence in the reconstructed parameters of the data. Several causes for the dependence, such as the magnetic field, the telescope position and code implementation were tested. This review identified a difference between the assumed position for the MC simulations and the actual telescope position. It was revealed by a survey of the telescopes' position, which showed a previously unaccounted height difference of 1.2 m and an increase of 0.5 m in the distance between the two telescopes. While the height difference between the two telescopes does contribute to the azimuth dependence observed in the reconstructed parameters, it is not sufficient to explain the total dependence observed.

Eventually, it was decided to concentrate on the azimuth range, in which the MC correctly reproduce the data. A cut in azimuth was applied to the data, as well as cuts in energy, observation period and zenith to limit the data to a range which was well-covered by the MC simulations. All data fullfilling these criteria and containing no detectable point-like source where then used to calculate the energy density spectrum of the cosmic electrons.

The cosmic electron spectrum was measured in the energy range from 130 GeV to 4 TeV. The result is shown in Fig.6.1. Contrary to measurements performed by other IACT, the spectrum shows no visible break and follows a pure power-law:

$$\frac{\mathrm{d}F}{\mathrm{d}E}_{\mathrm{Tikhonov}} = (1.17 \pm 0.08_{\mathrm{stat}} \pm 0.47_{\mathrm{sys}}) \times 10^{-7} \times \left(\frac{E}{1\,\mathrm{TeV}}\right)^{-3.14 \pm 0.05_{\mathrm{stat}} \pm 0.5_{\mathrm{sys}}} \mathrm{GeV}^{-1}\,\mathrm{m}^{-2}\,\mathrm{s}^{-1}\,\mathrm{sr}^{-1}.$$

The systematic uncertainty in the flux normalization was estimated to be of the order of 50%, while the uncertainty of the spectral index is 0.5. The main systematic uncertainties

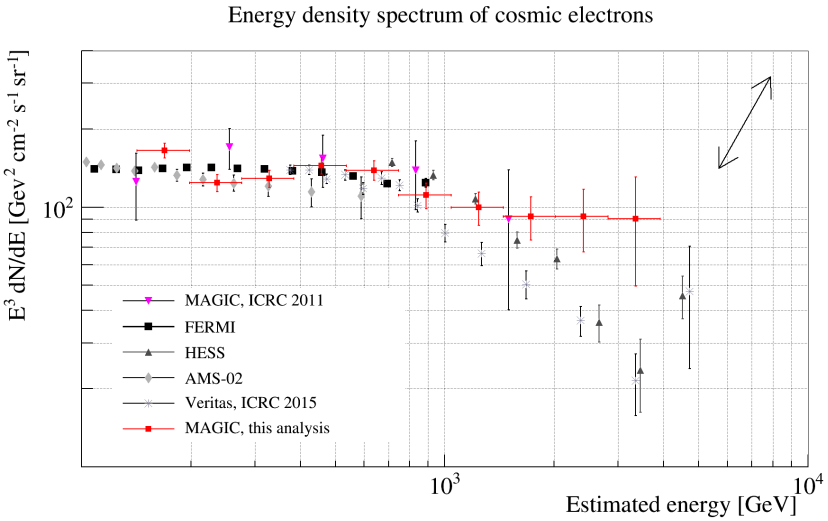

Figure 6.1: The electron spectrum as measured by MAGIC. The arrow represents the systematic uncertainty of the data points shown.

come from the energy estimation and the daily variation in the data. Additional theoretical uncertainties in the proton interaction cross sections affect the accuracy of the MC simulations.

Due to the large systematic uncertainty the interpretation of the spectrum proves difficult. While it is definitely in agreement with a close-by accelerator such as the Vela pulsar, it is impossible to dismiss any of the current models based on this result alone. However, the question of the origin may be answered within the coming years. The next generation of IACTs is currently under construction. It is expected that both the energy range and the γ-hadron separation will be improved with respect to the current generation of IACT. In addition, the CALET mission on the ISS has started operation and expects to publish an extension of the electron spectrum up to 20 TeV within the coming 5 years.

A. Parameter comparison: data - Monte Carlo

A.0.1. Parameter evolution vs energy

Figure A.1: Parameter distribution of shower image in telescope M1, comparing data to proton MC.

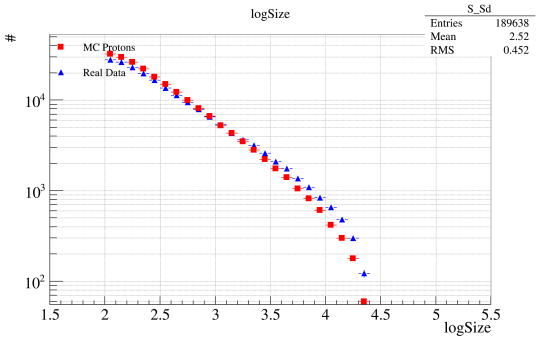

(a) size of the Hillas ellipse

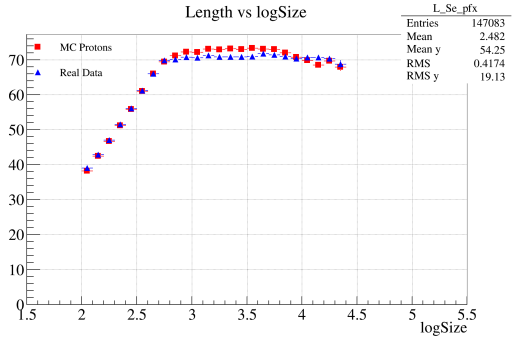

(b) length of the Hillas ellipse

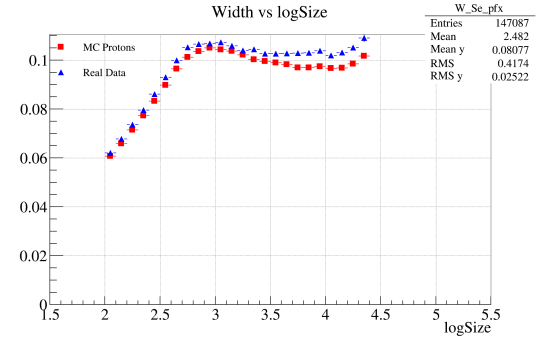

(c) width of the Hillas ellipse

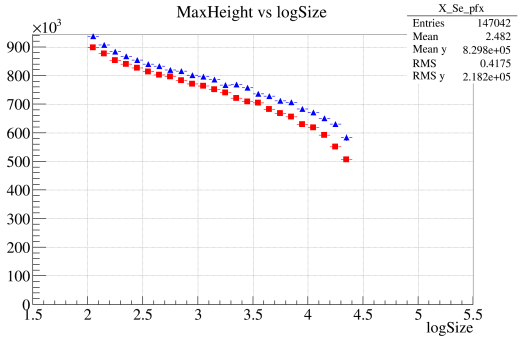

(d) Reconstructed MaxHeight

Figure A.2: Parameter distribution of shower image in telescope M2, comparing data to proton MC.

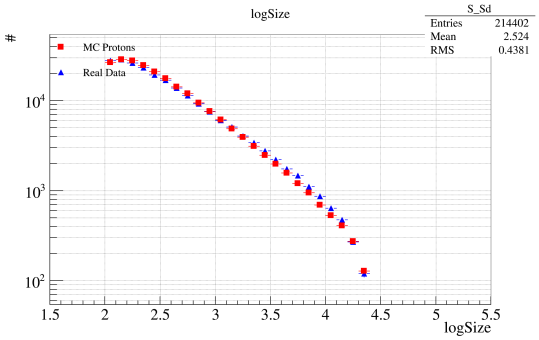

(a) size of the Hillas ellipse

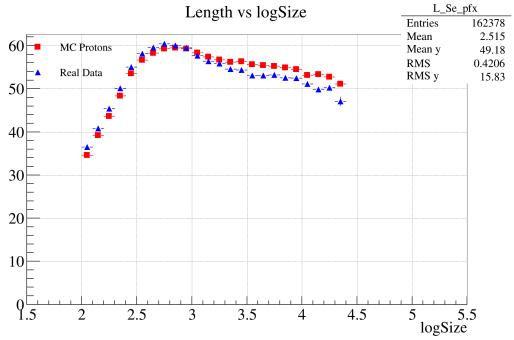

(b) length of the Hillas ellipse

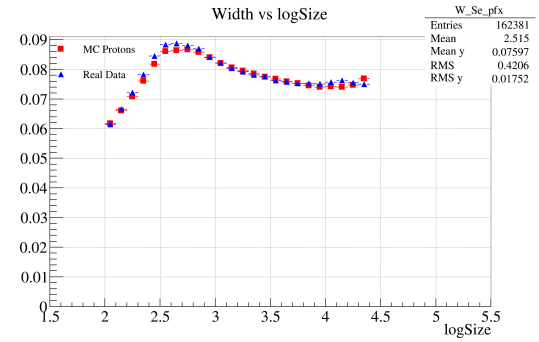

(c) width of the Hillas ellipse

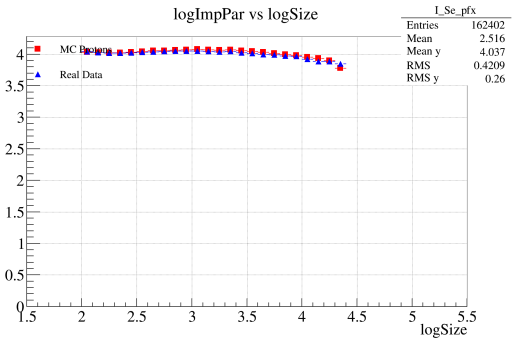

(d) Reconstructed point of Impact

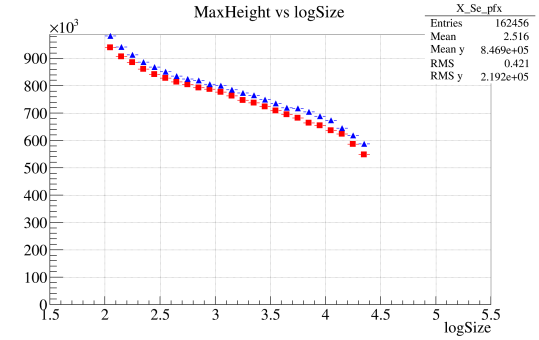

(e) Reconstructed MaxHeight

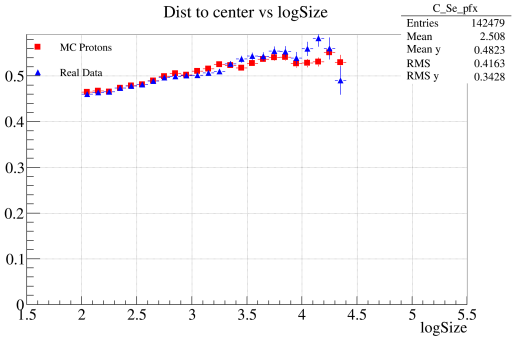

(f) Distribution of events over the camera plane. Distance between camera center and the CoG of the shower

A.0.2. Low energy

Figure A.3: Parameter distribution in the energy range 150 GeV to 300 GeV in telescope M1, comparing data to proton MC.

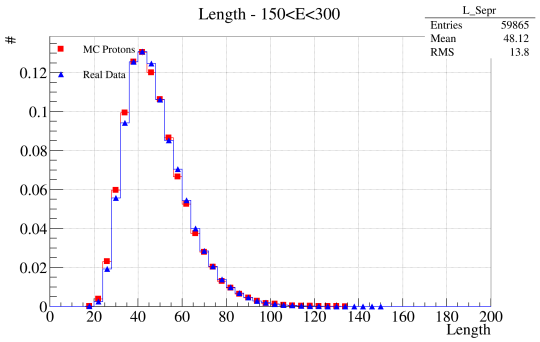

(a) length of the Hillas ellipse

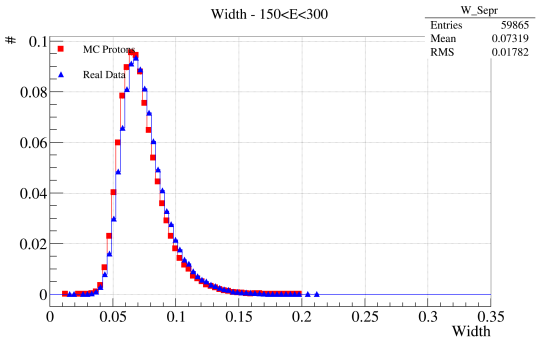

(b) width of the Hillas ellipse

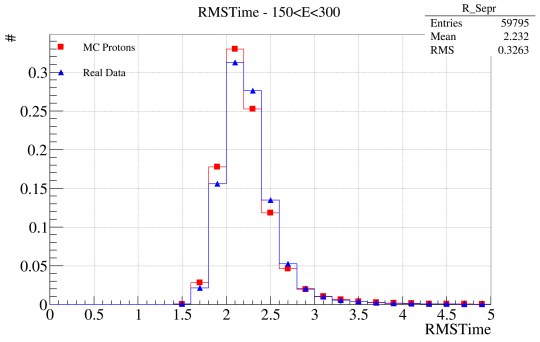

(c) Time span over which the Cherenkov photons arrive.

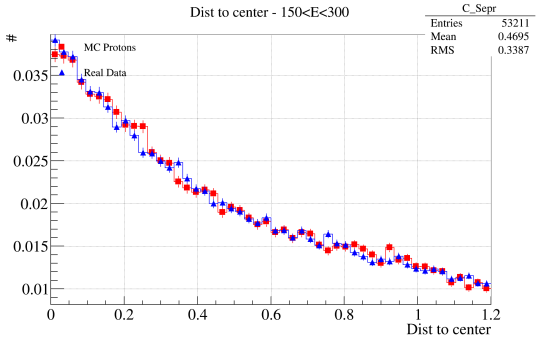

(d) Distribution of events over the camera plane. Distance between camera center and the CoG of the shower

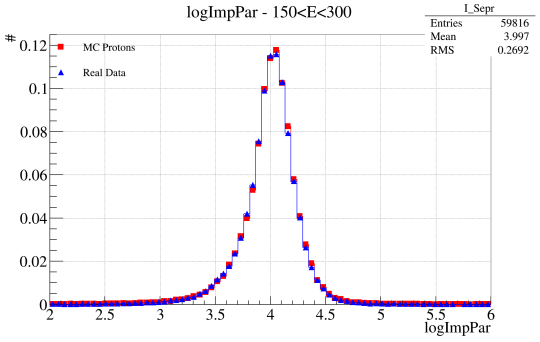

(e) Reconstructed point of impact

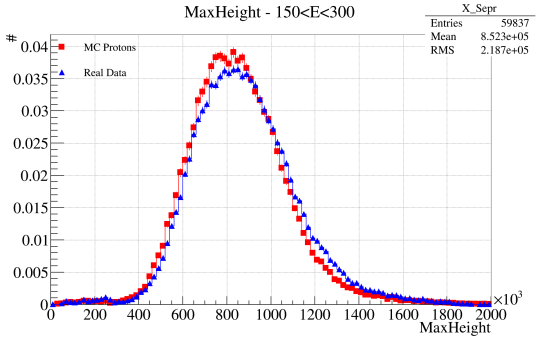

(f) Reconstructed MaxHeight

Figure A.4: Parameter distribution in the energy range 150 GeV to 300 GeV in telescope M2, comparing data to proton MC.

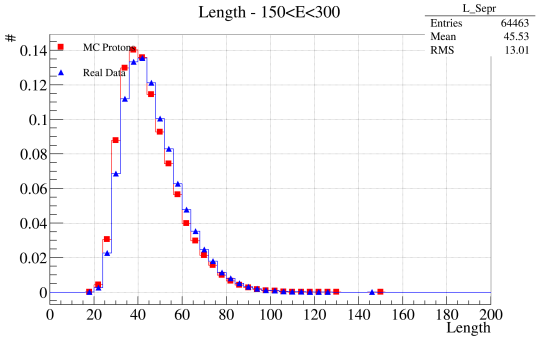

(a) length of the Hillas ellipse

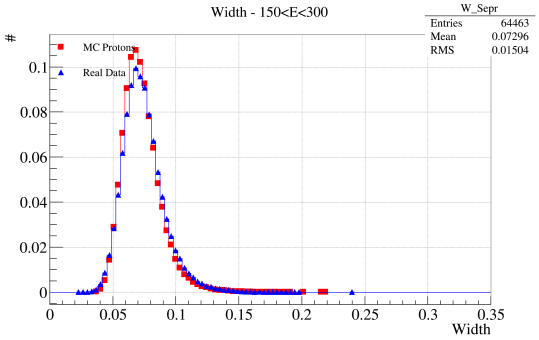

(b) width of the Hillas ellipse

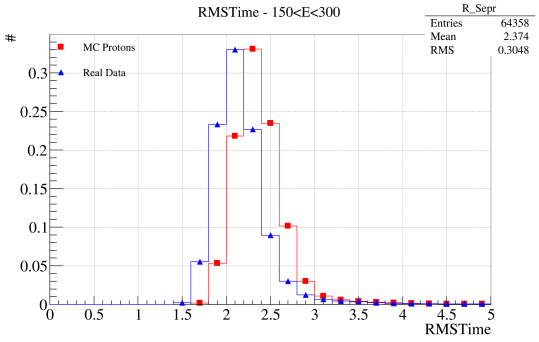

(c) Time span over which the Cherenkov photons arrive.

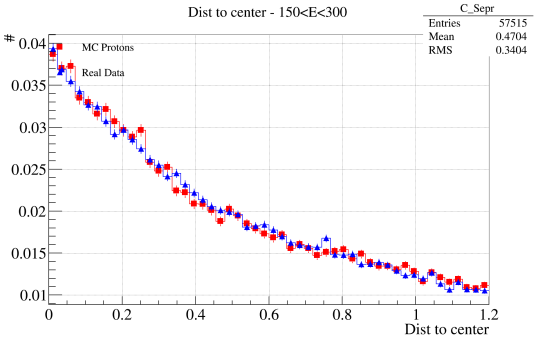

(d) Distribution of events over the camera plane. Distance between camera center and the CoG of the shower

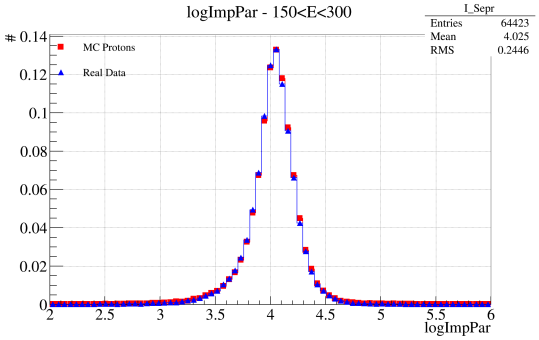

(e) Reconstructed point of impact

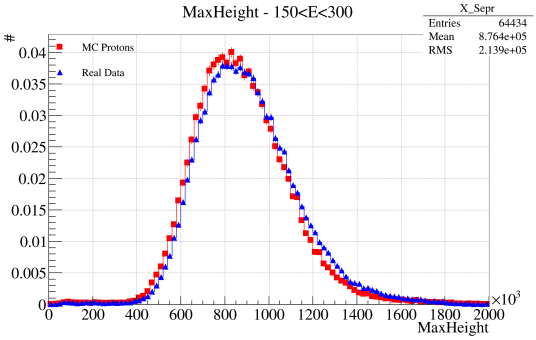

(f) Reconstructed MaxHeight

A.0.3. Intermediate energy

Figure A.5: Parameter distribution in the energy range 300 GeV to 500 GeV in telescope M1, comparing data to proton MC.

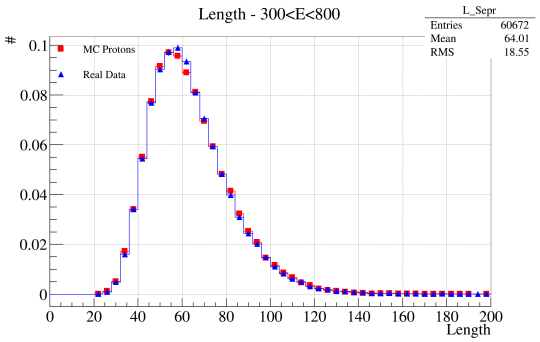

(a) length of the Hillas ellipse

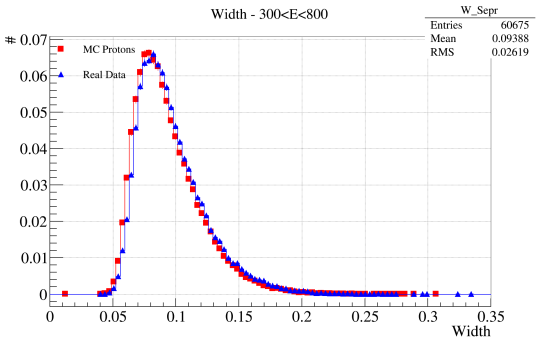

(b) width of the Hillas ellipse

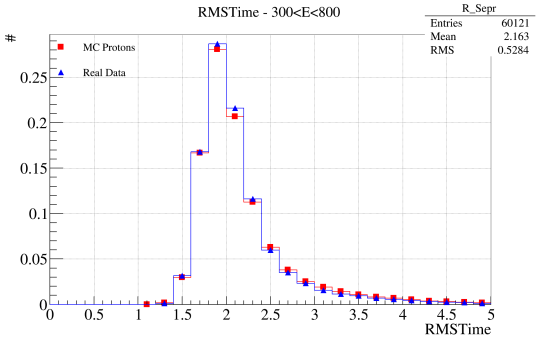

(c) Time span over which the Cherenkov photons arrive.

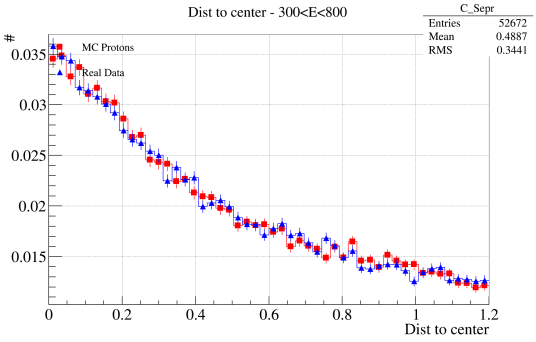

(d) Distribution of events over the camera plane. Distance between camera center and the CoG of the shower

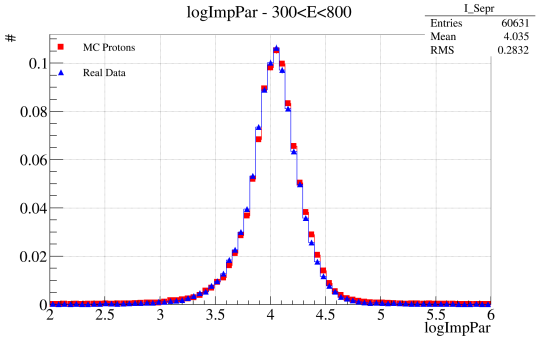

(e) Reconstructed point of impact

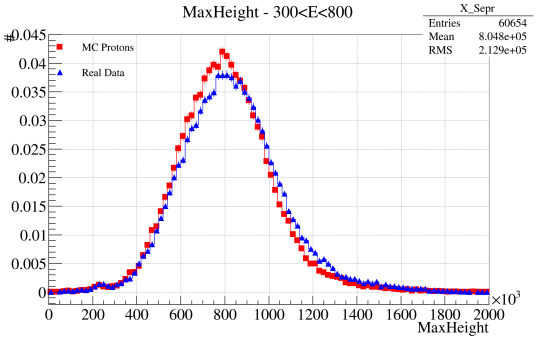

(f) Reconstructed MaxHeight

Figure A.6: Parameter distribution in the energy range 300 GeV to 500 GeV in telescope M2, comparing data to proton MC.

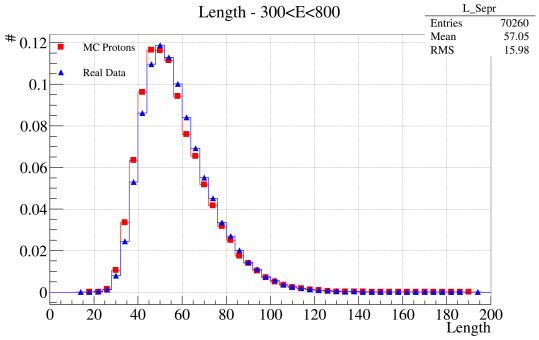

(a) length of the Hillas ellipse

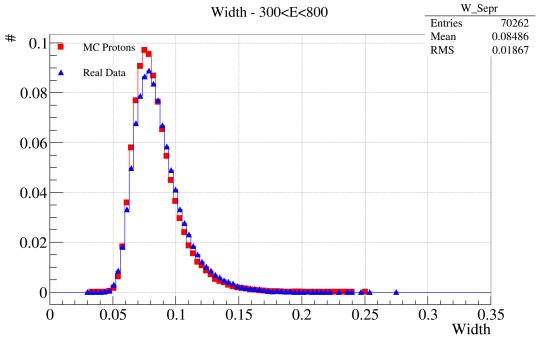

(b) width of the Hillas ellipse

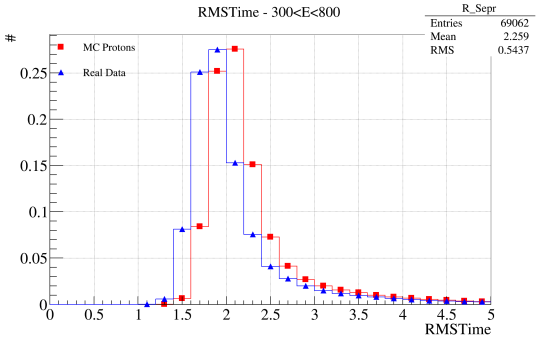

(c) Time span over which the Cherenkov photons arrive.

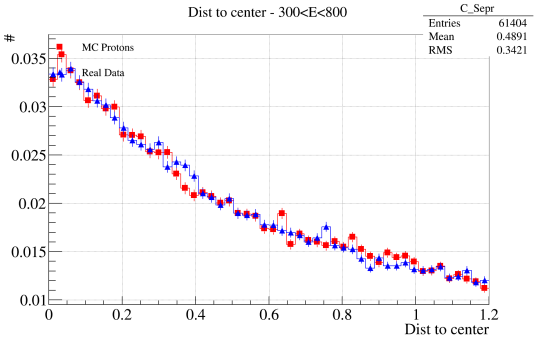

(d) Distribution of events over the camera plane. Distance between camera center and the CoG of the shower

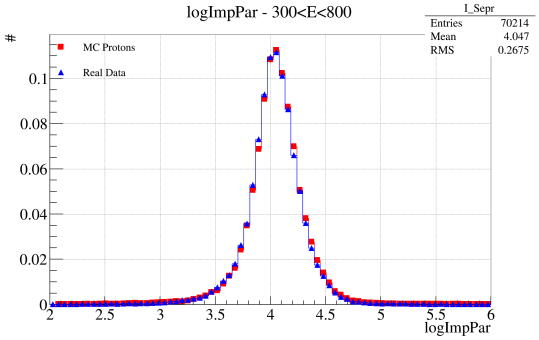

(e) Reconstructed point of impact

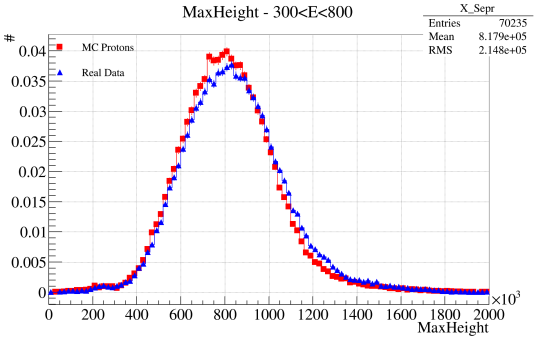

(f) Reconstructed MaxHeight

A.0.4. Middle-high energy

Figure A.7: Parameter distribution in the energy range 500 GeV to 800 GeV in telescope M1, comparing data to proton MC.

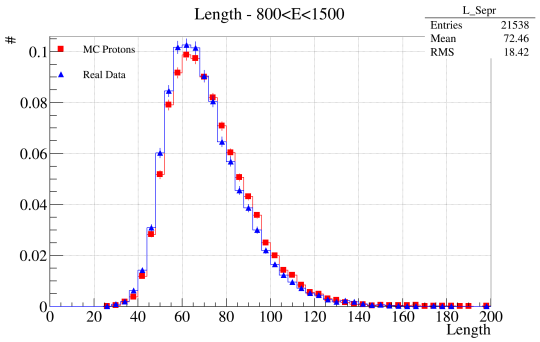

(a) length of the Hillas ellipse

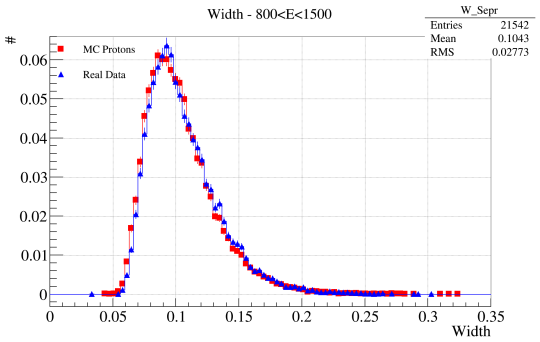

(b) width of the Hillas ellipse

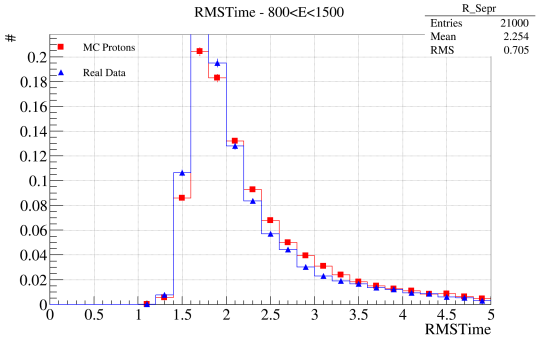

(c) Time span over which the Cherenkov photons arrive.

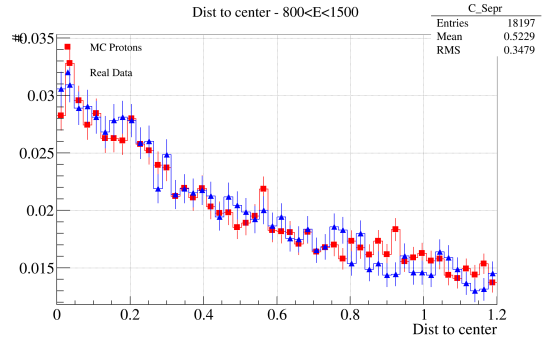

(d) Distribution of events over the camera plane. Distance between camera center and the CoG of the shower

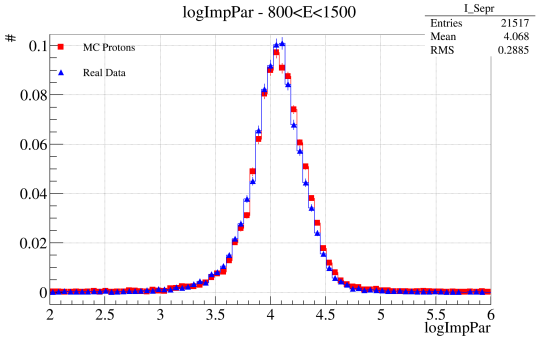

(e) Reconstructed point of impact

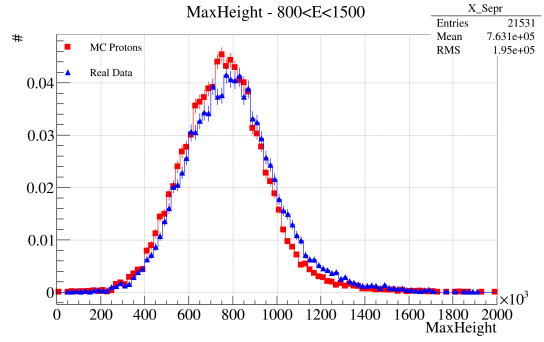

(f) Reconstructed MaxHeight

Figure A.8: Parameter distribution in the energy range 500 GeV to 800 GeV in telescope M2, comparing data to proton MC.

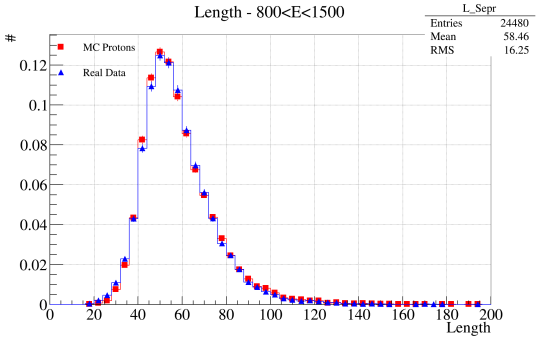

(a) length of the Hillas ellipse

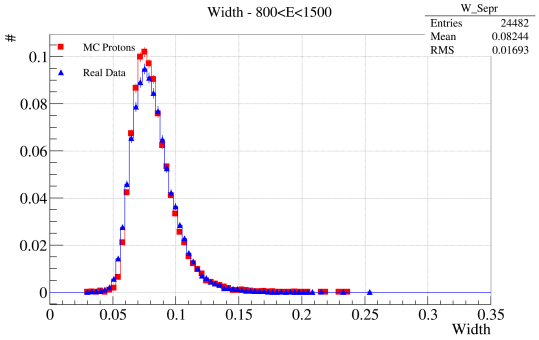

(b) width of the Hillas ellipse

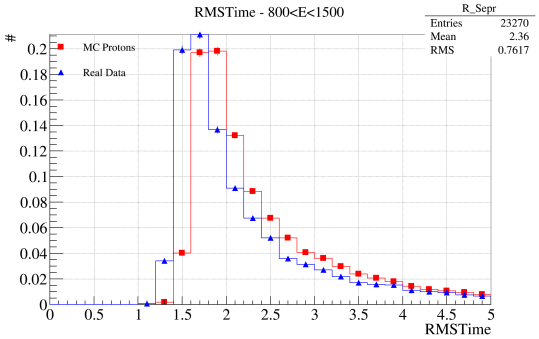

(c) Time span over which the Cherenkov photons arrive.

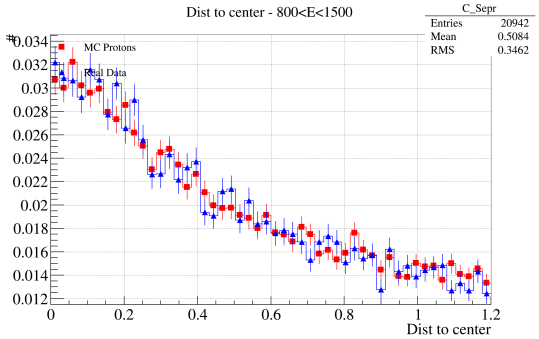

(d) Distribution of events over the camera plane. Distance between camera center and the CoG of the shower

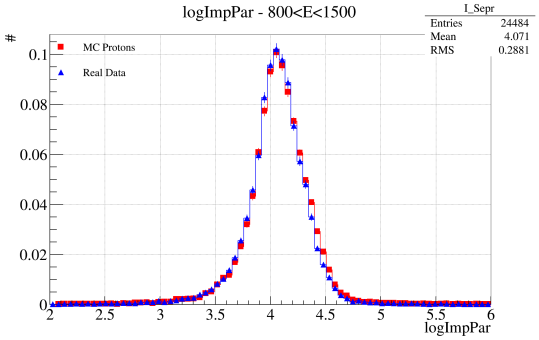

(e) Reconstructed point of impact

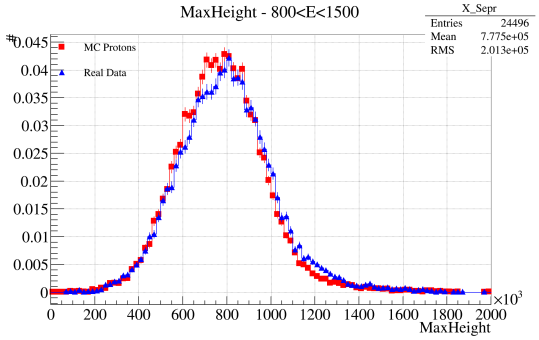

(f) Reconstructed MaxHeight

A.0.5. High energy

Figure A.9: Parameter distribution in the energy range 800 GeV to 1500 GeV in telescope M1, comparing data to proton MC.

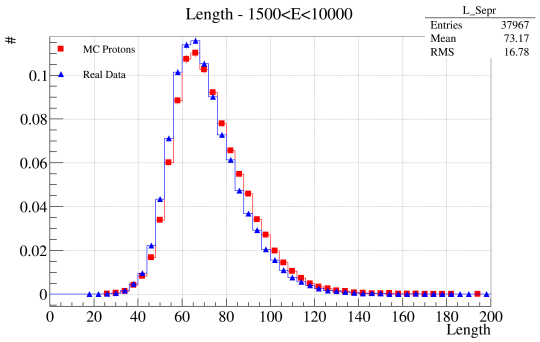

(a) length of the Hillas ellipse

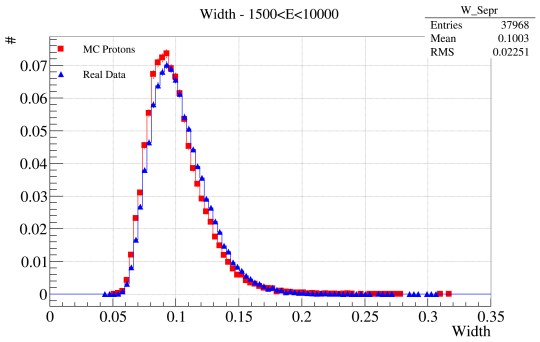

(b) width of the Hillas ellipse

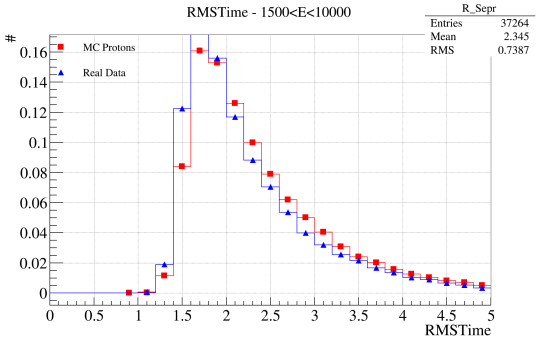

(c) Time span over which the Cherenkov photons arrive.

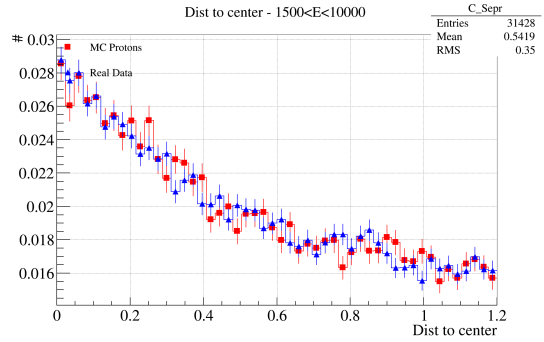

(d) Distribution of events over the camera plane. Distance between camera center and the CoG of the shower

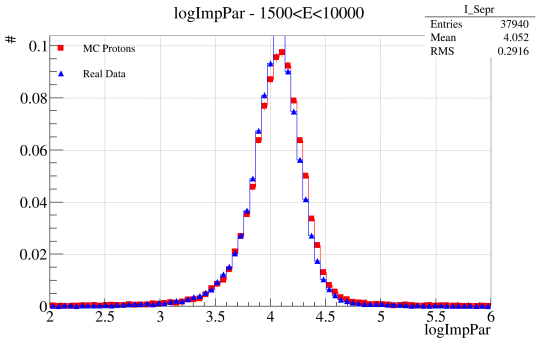

(e) Reconstructed point of impact

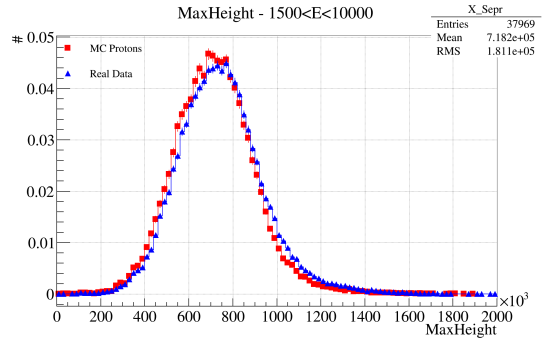

(f) Reconstructed MaxHeight

Figure A.10: Parameter distribution in the energy range 800 GeV to 1500 GeV in telescope M2, comparing data to proton MC.

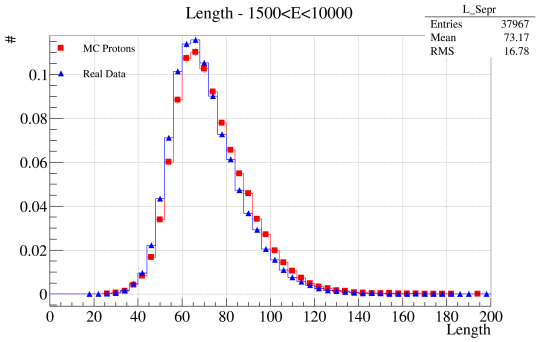

(a) length of the Hillas ellipse

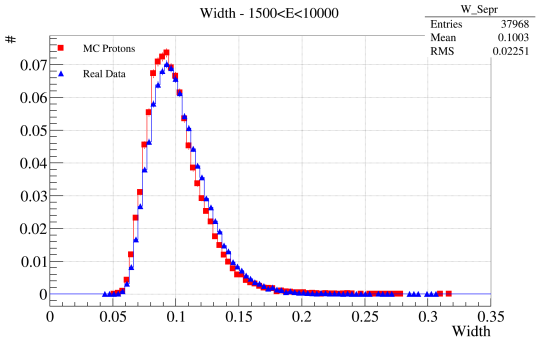

(b) width of the Hillas ellipse

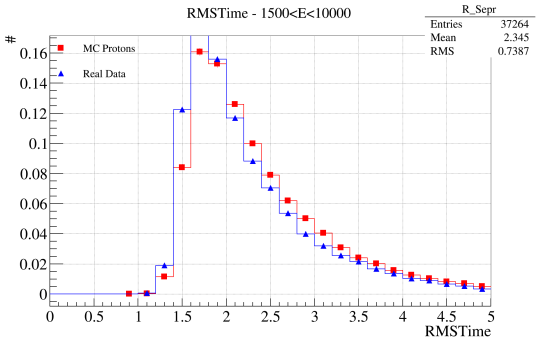

(c) Time span over which the Cherenkov photons arrive.

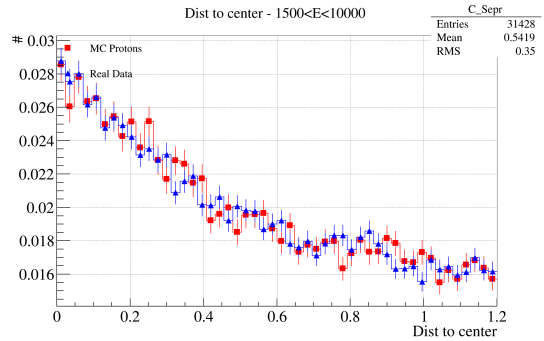

(d) Distribution of events over the camera plane. Distance between camera center and the CoG of the shower

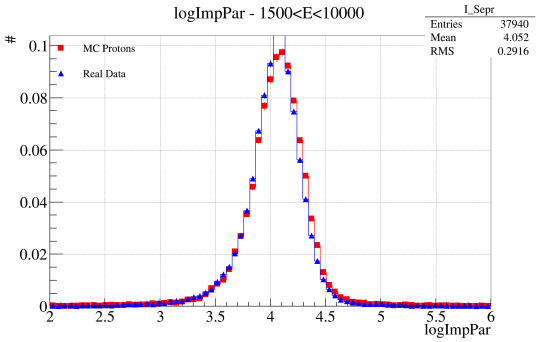

(e) Reconstructed point of impact

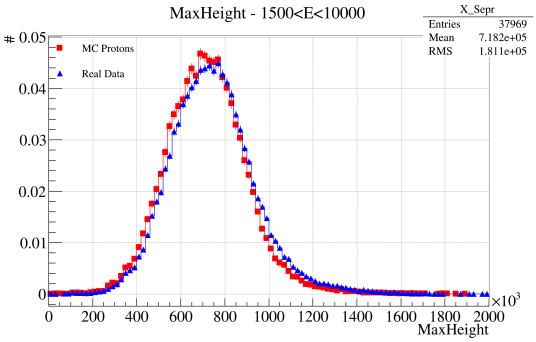

(f) Reconstructed MaxHeight

A.0.6. Very-high energy

Figure A.11: Parameter distribution in the energy range 1500 GeV to 7500 GeV in telescope M1, comparing data to proton MC.

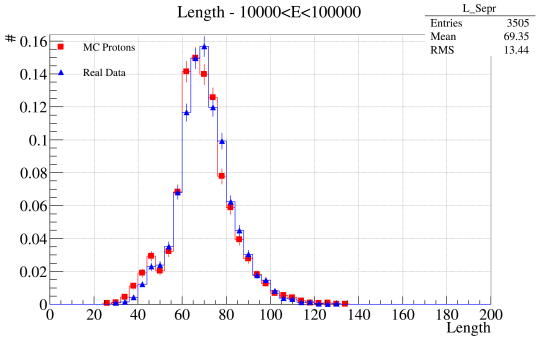

(a) length of the Hillas ellipse

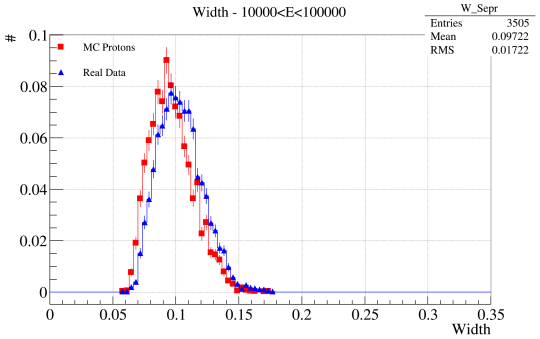

(b) width of the Hillas ellipse

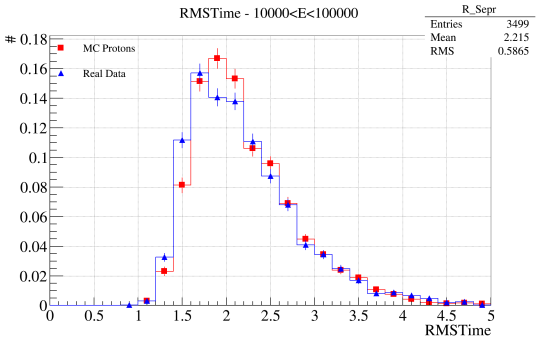

(c) Time span over which the Cherenkov photons arrive.

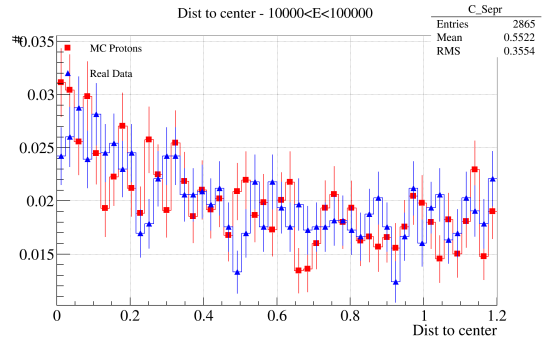

(d) Distribution of events over the camera plane. Distance between camera center and the CoG of the shower

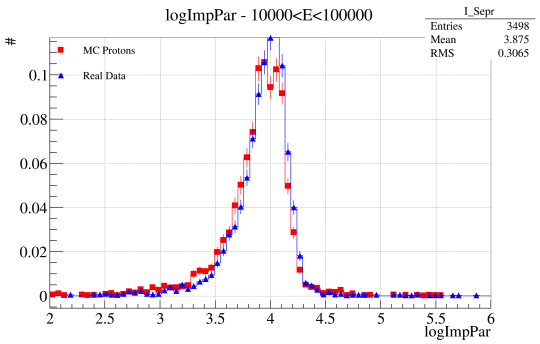

(e) Reconstructed point of impact

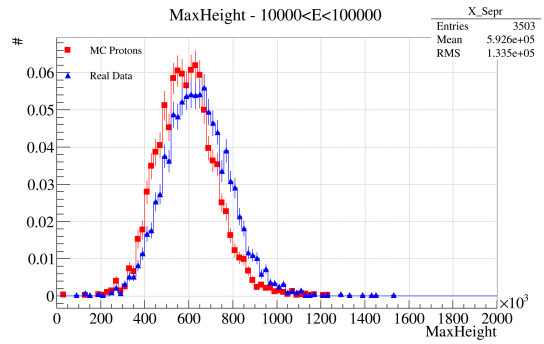

(f) Reconstructed MaxHeight

Figure A.12: Parameter distribution in the energy range 1500 GeV to 7500 GeV in telescope M2, comparing data to proton MC.

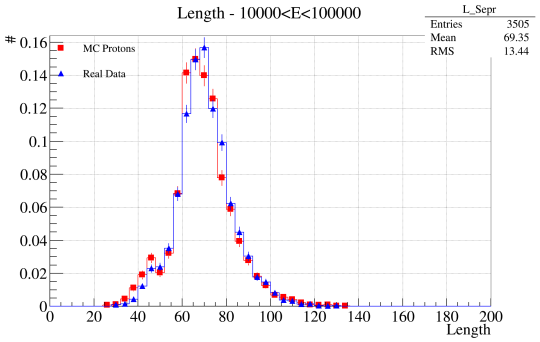

(a) length of the Hillas ellipse

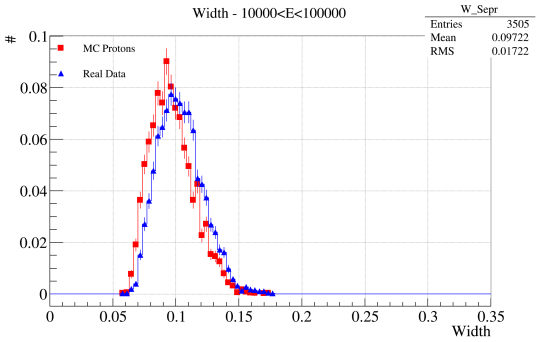

(b) width of the Hillas ellipse

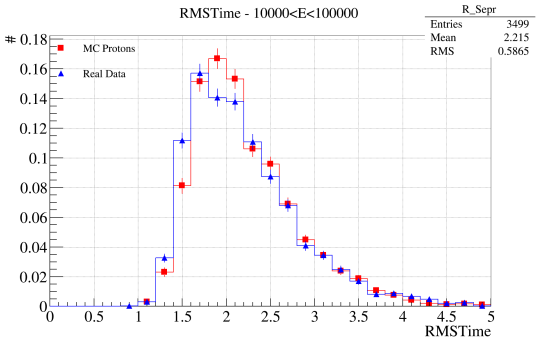

(c) Time span over which the Cherenkov photons arrive.

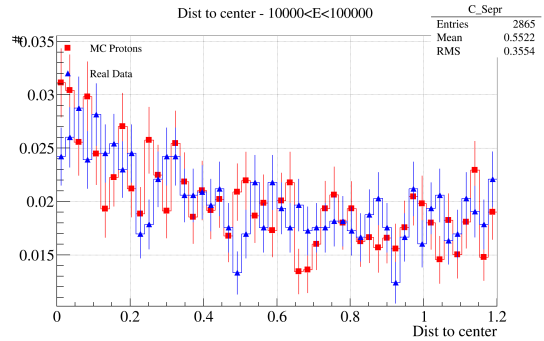

(d) Distribution of events over the camera plane. Distance between camera center and the CoG of the shower

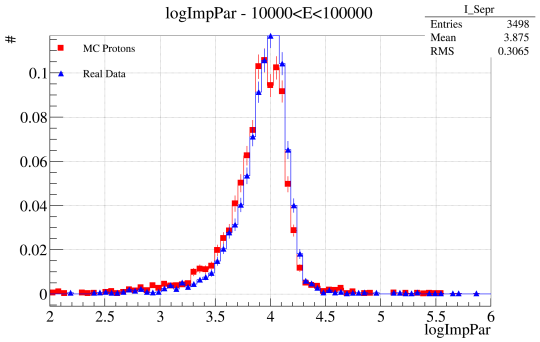

(e) Reconstructed point of impact

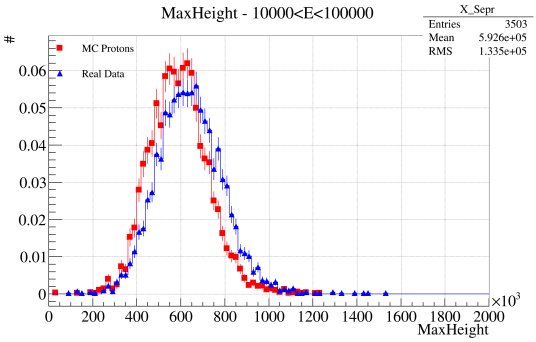

(f) Reconstructed MaxHeight

B. Point-source analysis of sources for the diffuse analysis

B.1. θ^2-plots

The θ^2-plots show the excess of flux coming from the assumed source position over the isotropic background. An excess of less than 2σ was required for the diffuse analysis.

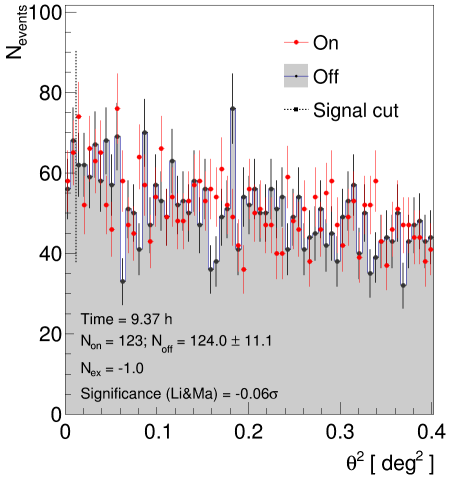

(a) 1FGLJ2347.3+0710

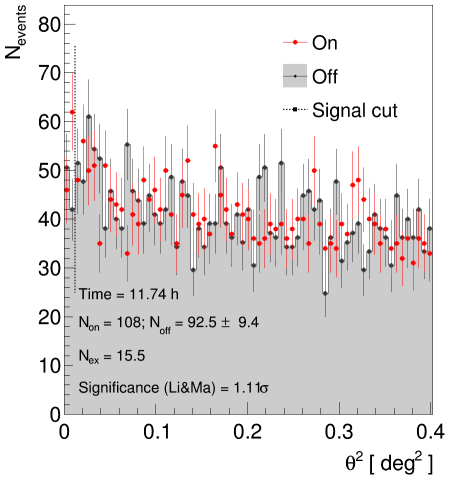

(b) 1FGLJ0338.8+1313

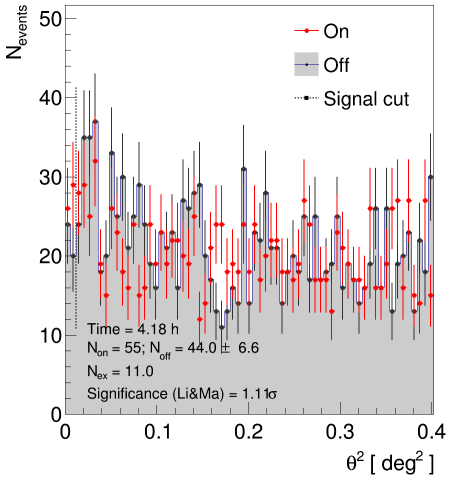

(c) 3c454.3

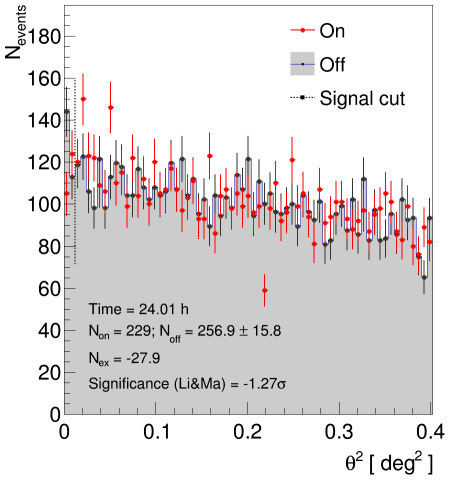

(d) Segue 1

Figure B.1: θ^2 distributions of the sources and the determined excess γ-rays coming from the selected position.

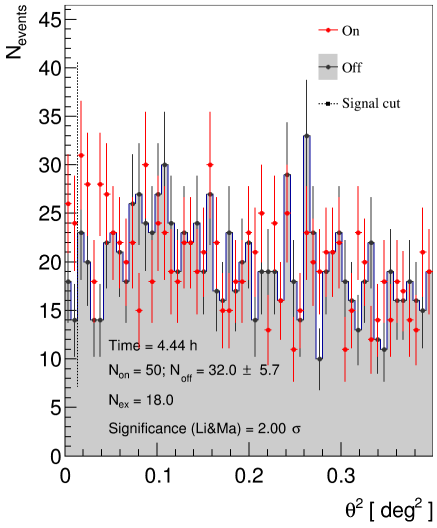

(a) Swift J1644+57

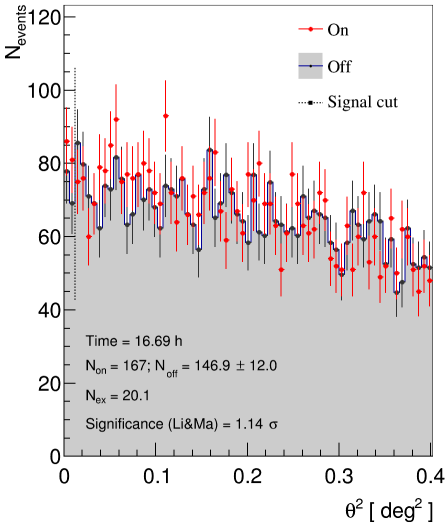

(b) 4c55.17

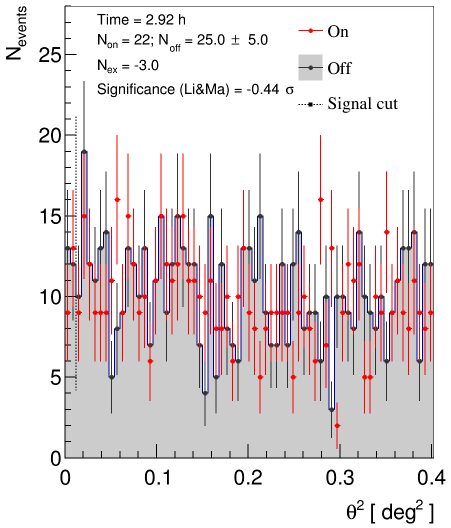

(c) 1ES 2321+419

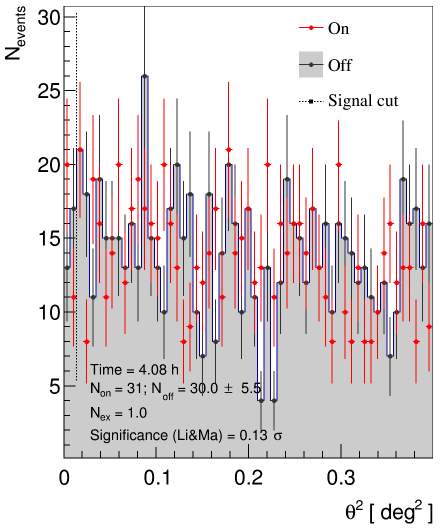

(d) MS1050.7+4946

Figure B.2: θ^2 distributions of the sources and the determined excess γ-rays coming from the selected position.

B.2. Sky maps

The sky maps show the relative flux variation over the observed field of view. The fluctuations are expected to be smaller the longer a source was observed. This is visible, for example comparing 2 h of 3c454.3 with 28 h of Segue 1.

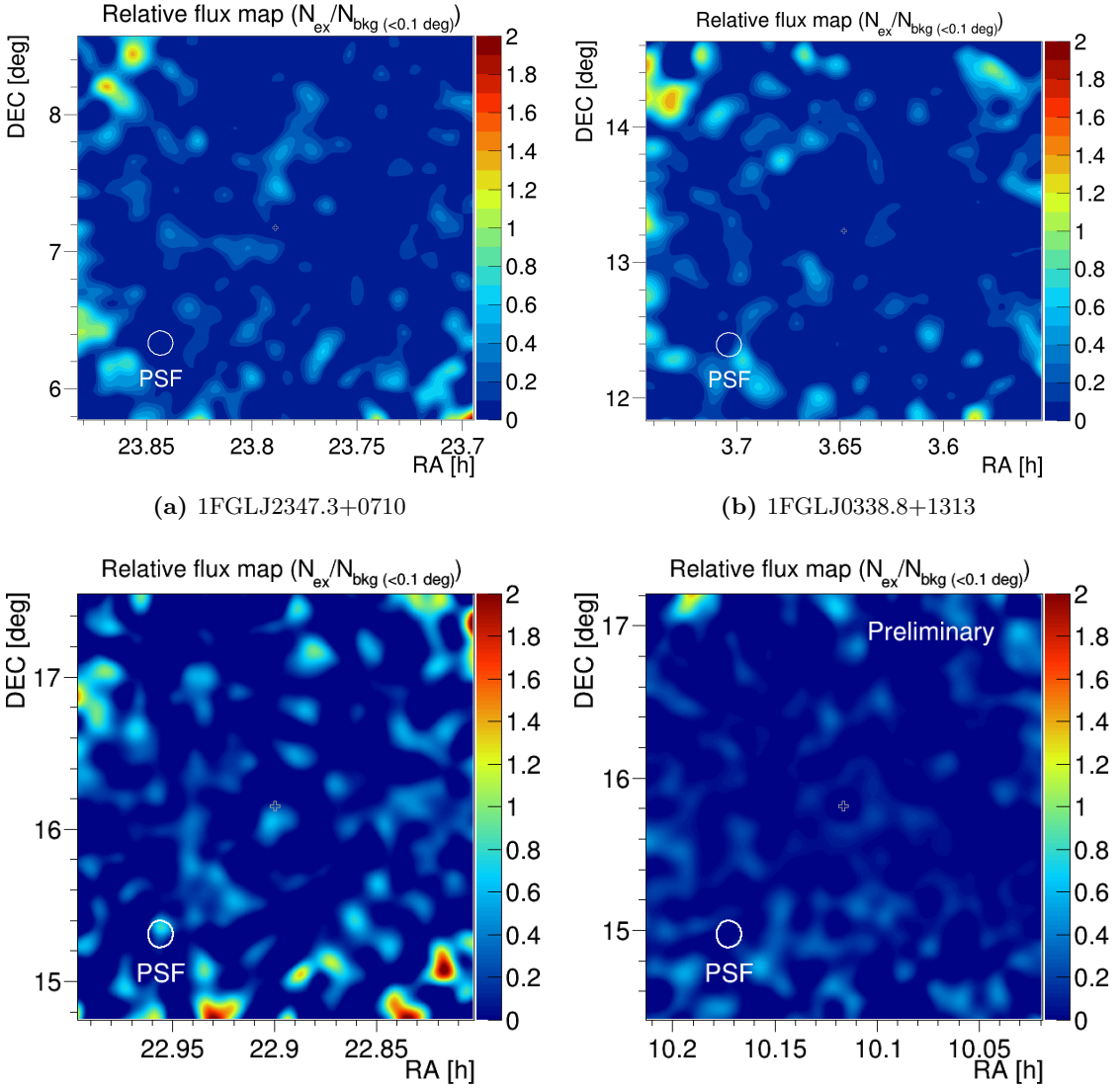

(a) 1FGLJ2347.3+0710

(b) 1FGLJ0338.8+1313

(c) 3c454.3

(d) Segue 1

Figure B.3: sky map of the field of view around the observed sources and the relative coming from the selected position.

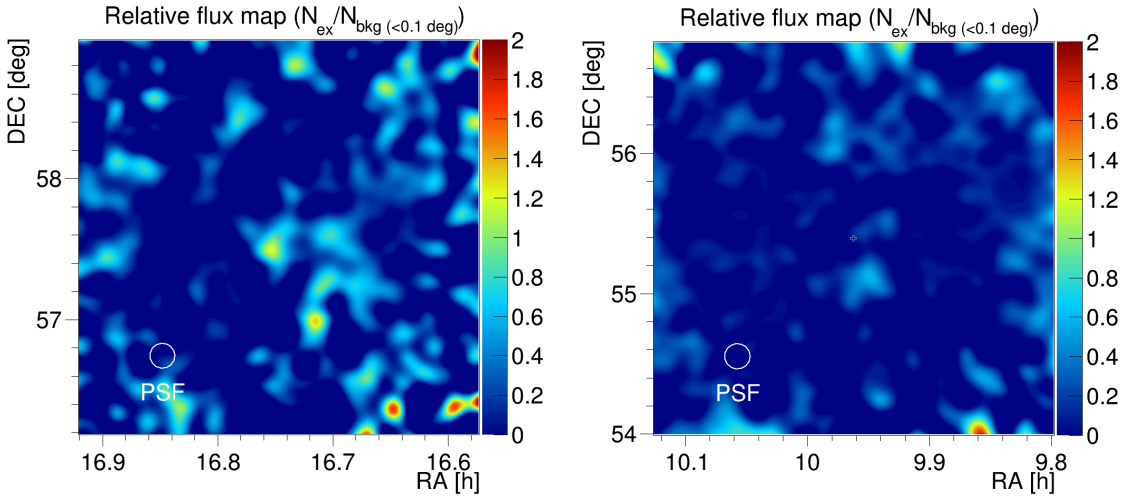

(a) Swift J1644+57 **(b)** 4c55.17

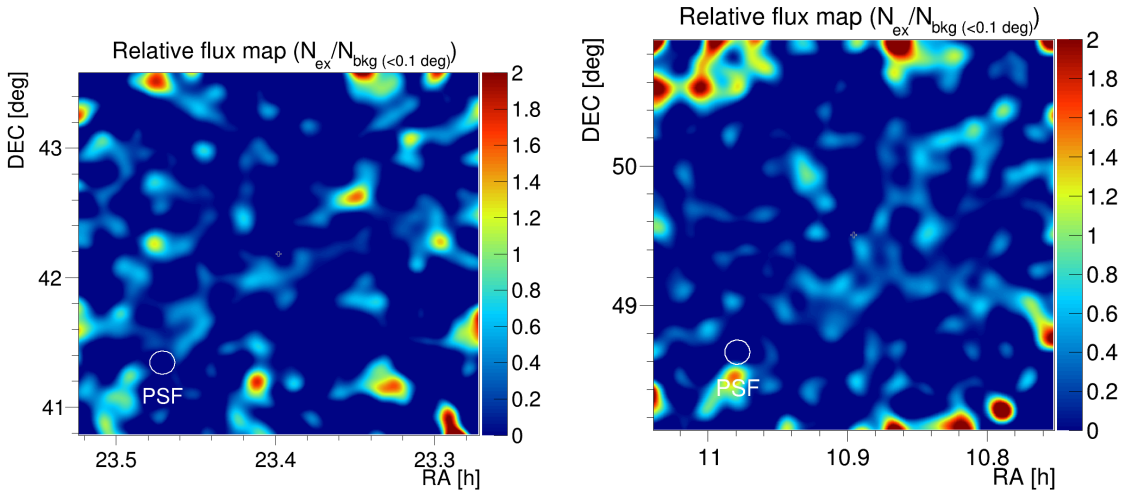

(c) 1ES 2321+419 **(d)** MS1050.7+4946

Figure B.4: sky map of the field of view around the observed sources and the relative coming from the selected position.

List of Figures

List of Tables

Abbreviations

AMS-02 Alpha Magnetic Spectrometer 2. 9

asl above sea level. 25, 82

CoG Center of Gravity. 31

CTA Cherenkov Telescope Array. 18

DISP Distance between Image centroid and Source Position. 33, 34

EAS extensive air shower. 18–20, 23, 25, 26, 82

FoV Field of View. 26–28

GALPROP GALactic PROPagation. 13

GRB Gamma Ray Bursts. 26

HEGRA High Energy Gamma Ray Astronomy. 18

H.E.S.S. High Energy Stereoscopic System. 9, 18

IACT Imaging Atmospheric Cherenkov Technique. 18–20, 23, 25, 26, 82

ISM Inter Stellar Medium. 4

LUT look-up tables. 34

M1 MI, MAGIC-I, first telescope camera. 26, 27, 30–32

M2 MII, MAGIC-II, camera of the second telescope. 26, 27, 30, 32

MAGIC Major Atmospheric Gamma-Ray Imaging Cherenkov. 9, 18, 19, 25, 26, 28, 31, 82

MARS MAGIC Analysis and Reconstruction Software. 28–30, 82

MC Monte Carlo. 34, 71

NSB Night Sky Background. 28, 30, 40

ORM Observatory del Roque de los Muchachos. 26

PhE Photo Electrons. 27–30, 45, 48, 53

PMT photomultiplier tube. 25–28, 30

RF Random Forest. 33, 42

SNR super nova remnant. 4

UTM Universal Transverse Mercator. 76

VERITAS Very Energetic Radiation Imaging Telescope Array System. 18

Bibliography

[1] "AMS Days at CERN" and latest results. https://indico.cern.ch/event/381134/.

[2] Aartsen, M. G., Abbasi, R., Abdou, Y., et al. IceCube search for dark matter annihilation in nearby galaxies and galaxy clusters. *Physical Review D 88*, 12 (dec 2013), 122001.

[3] Abbasi, R. U., Abu-Zayyad, T., Allen, M., et al. first observation of the Greisen-Zatsepin-Kuzmin suppression. *Physical Review Letters 100*, 10 (mar 2008), 101101.

[4] Abdo, A. A., Ackermann, M., Ajello, M., et al. Fermi large area telescope measurements of the diffuse gamma-ray emission at intermediate galactic latitudes. *Physical Review Letters 103*, 25 (dec 2009), 251101.

[5] Abdo, A. A., Ackermann, M., Ajello, M., et al. measurement of the cosmic ray $e^+ + e^-$ spectrum from 20 GeV to 1 TeV with the Fermi large area telescope. *Physical Review Letters 102*, 18 (may 2009), 181101.

[6] Abdo, A. A., Ackermann, M., Ajello, M., et al. spectrum of the iiotropic diffuse gamma-ray emission derived from first-year Fermi large area telescope data. *Physical Review Letters 104*, 10 (mar 2010), 101101.

[7] Abdo, A. A., Ackermann, M., Ajello, M., et al. detection of the small magellanic cloud in gamma-rays with Fermi /LAT. *Astronomy & Astrophysics 523* (nov 2010), A46.

[8] Abeysekara, A. U., and Linnemann, J. T. experimental constraints on γ-ray pulsar gap models and the pulsar GeV to pulsar wind nebula TeV connection. *Astrophysical Journal 804*, 1 (apr 2015), 25.

[9] Abramowski, A., Acero, F., Aharonian, F., et al. search for a dark matter annihilation signal from the galactic center halo with H.E.S.S. *Physical Review Letters 106*, 16 (apr 2011), 161301.

[10] Abramowski, A., Aharonian, F., Benkhali, F. A., et al. search for dark matter annihilation signatures in H.E.S.S. observations of dwarf spheroidal galaxies. *Physical Review D 90*, 11 (dec 2014), 112012.

[11] Abramowski, A., Aharonian, F., Benkhali, F. A., et al. diffuse galactic gamma-ray emission with H.E.S.S. *Physical Review D 90*, 12 (dec 2014), 122007.

[12] Abramowski, A., Aharonian, F., Benkhali, F. A., et al. acceleration of petaelectronvolt protons in the galactic centre. *Nature 531*, 7595 (mar 2016), 476–479.

[13] Abreu, P., et al. the Pierre Auger Observatory I: the cosmic ray energy spectrum and related measurements. In *Proceedings, 32nd International Cosmic Ray Conference (ICRC 2011)* (2011).

[14] Accardo, L., Aguilar, M., Aisa, D., et al. high statistics measurement of the positron fraction in primary cosmic rays of 0.5–500 GeV with the Alpha Magnetic Spectrometer on the International Space Station. *Physical Review Letters 113*, 12 (sep 2014), 121101.

[15] Ackermann, M., Ajello, M., Albert, A., et al. resolving the extragalacticγ-ray background above 50 GeV with the Fermi Large Area Telescope. *Physical Review Letters 116*, 15 (apr 2016), 151105.

[16] Ackermann, M., Ajello, M., Albert, A., et al. The spectrum of isotropic diffuse gamma-ray emission between 100 MeV and 820 GeV. *Astrophysical Journal 799*, 1 (jan 2015), 86.

[17] Ackermann, M., Ajello, M., Allafort, A., et al. measurement of separate cosmic-ray electron and positron spectra with the Fermi Large Area Telescope. *Physical Review Letters 108*, 1 (jan 2012), 011103.

[18] Ackermann, M., Ajello, M., Allafort, A., et al. detection of the characteristic pion-decay signature in supernova remnants. *Science 339*, 6121 (feb 2013), 807–811.

[19] Ackermann, M., Ajello, M., Allafort, A., et al. Fermi large area telescope study of cosmic rays and the interstellar medium in nearby molecular clouds. *Astrophysical Journal 755*, 1 (jul 2012), 22. [Erratum: ApJ.778,82(2013)].

[20] Ackermann, M., Ajello, M., Asano, K., et al. Fermi-LAT observations of the gamma-ray burst GRB 130427A. *Science 343*, 6166 (nov 2013), 42–47.

[21] Ackermann, M., Ajello, M., Atwood, W. B., et al. Fermi LAT observations of cosmic-ray electrons from 7 GeV to 1 TeV. *Physical Review D 82*, 9 (nov 2010), 092004.

[22] Ackermann, M., Ajello, M., Atwood, W. B., et al. Fermi-LAT observations of the diffuse gamma-ray emission: implications for cosmic rays and the interstellar medium. *Astrophysical Journal 750*, 1 (apr 2012), 3.

[23] Ackermann, M., Ajello, M., Atwood, W. B., et al. searches for cosmic-ray electron anisotropies with the Fermi Large Area Telescope. *Physical Review D 82*, 9 (nov 2010), 092003.

[24] Ackermann, M., Albert, A., Anderson, B., et al. dark matter constraints from observations of 25 Milky Way satellite galaxies with the Fermi Large Area Telescope. *Physical Review D 89*, 4 (feb 2014), 042001.

[25] Actis, M., Agnetta, G., Aharonian, F., et al. design concepts for the Cherenkov Telescope Array CTA: an advanced facility for ground-based high-energy gamma-ray astronomy. *Experimental Astronomy 32*, 3 (nov 2011), 193–316.

[26] Adriani, O., Barbarino, G., Bazilevskaya, G., et al. Time dependence of the electron and positron components of the cosmic radiation measured by the PAMELA experiment between July 2006 and December 2015. *Phys. Rev. Lett. 116*, 24 (jun 2016), 241105.

[27] Adriani, O., Barbarino, G. C., Bazilevskaya, G. A., et al. PAMELA results on the cosmic-ray antiproton flux from 60 MeV to 180 GeV in kinetic energy. *Physical Review Letters 105*, 12 (sep 2010), 121101.

[28] Adriani, O., Barbarino, G. C., Bazilevskaya, G. A., et al. an anomalous positron abundance in cosmic rays with energies 1.5–100 GeV. *Nature 458*, 7238 (apr 2009), 607–609.

[29] Adriani, O., Barbarino, G. C., Bazilevskaya, G. A., et al. new measurement of the antiproton-to-proton flux ratio up to 100 GeV in the cosmic radiation. *Physical Review Letters 102*, 5 (feb 2009), 051101.

[30] Adriani, O., Barbarino, G. C., Bazilevskaya, G. A., et al. cosmic-ray electron flux measured by the PAMELA experiment between 1 and 625 GeV. *Physical Review Letters 106*, 20 (may 2011), 201101.

[31] Adriani, O., Barbarino, G. C., Bazilevskaya, G. A., et al. search for anisotropies in cosmic-ray positrons detected by the PAMELA experiment. *Astrophysical Journal 811*, 1 (sep 2015), 21.

[32] Aguilar, M., Aisa, D., Alpat, B., et al. precision measurement of the (e^+ + e^-) flux in primary cosmic rays from 0.5 GeV to 1 TeV with the Alpha Magnetic Spectrometer on the International Space Station. *Physical Review Letters 113*, 22 (nov 2014), 221102.

[33] Aguilar, M., Alberti, G., Alpat, B., et al. first result from the Alpha Magnetic Spectrometer on the International Space Station: precision measurement of the positron fraction in primary cosmic rays of 0.5–350 GeV. *Physical Review Letters 110*, 14 (apr 2013), 141102.

[34] Aharonian, F., Akhperjanian, A. G., Anton, G., et al. probing the ATIC peak in the cosmic-ray electron spectrum with H.E.S.S. *Astronomy and Astrophysics 508*, 2 (dec 2009), 561–564.

[35] Aharonian, F., Akhperjanian, A. G., Bazer-Bachi, A. R., et al. observations of the Crab Nebula with H.E.S.S. *Astronomy and Astrophysics 457*, 3 (oct 2006), 899–915.

[36] Aharonian, F., Akhperjanian, A. G., de Almeida, U. B., et al. energy spectrum of cosmic-ray electrons at TeV energies. *Physical Review Letters 101*, 26 (dec 2008), 261104.

[37] Albert, J., Aliu, E., Anderhub, H., et al. FADC signal reconstruction for the MAGIC telescope. *Nuclear Instruments and Methods in Physics Research Section A: Accelerators, Spectrometers, Detectors and Associated Equipment 594*, 3 (sep 2008), 407–419.

[38] Albert, J., Aliu, E., Anderhub, H., et al. implementation of the random forest method for the imaging atmospheric cherenkov telescope MAGIC. *Nuclear Instruments and Methods in Physics Research Section A: Accelerators, Spectrometers, Detectors and Associated Equipment 588*, 3 (apr 2008), 424–432.

[39] Albert, J., Aliu, E., Anderhub, H., et al. unfolding of differential energy spectra in the MAGIC experiment. *Nuclear Instruments and Methods in Physics Research Section A: Accelerators, Spectrometers, Detectors and Associated Equipment 583*, 2-3 (dec 2007), 494–506.

[40] Albert, J., Aliu, E., Anderhub, H., et al. VHE γ-ray observation of the Crab Nebula and its pulsar with the MAGIC telescope. *Astrophysical Journal 674*, 2 (feb 2008), 1037–1055.

[41] Aleksić, J., Alvarez, E., Antonelli, L., et al. performance of the MAGIC stereo system obtained with Crab Nebula data. *Astroparticle Physics 35*, 7 (feb 2012), 435–448.

[42] Aleksić, J., Ansoldi, S., Antonelli, L., et al. the major upgrade of the MAGIC telescopes, part II: a performance study using observations of the Crab Nebula. *Astroparticle Physics 72* (jan 2016), 76–94.

[43] Aleksić, J., Ansoldi, S., Antonelli, L., et al. optimized dark matter searches in deep observations of segue 1 with MAGIC. *Journal of Cosmology and Astroparticle Physics 2014*, 02 (feb 2014), 008–008.

[44] Aliu, E., Archambault, S., Arlen, T., et al. VERITAS deep observations of the dwarf spheroidal galaxy segue 1. *Physical Review D 85*, 6 (mar 2012), 062001. [Erratum: Phys. Rev.D91,no.12,129903(2015)].

[45] Apel, W. D., Arteaga-Velàzquez, J. C., Bekk, K., et al. ankle-like feature in the energy spectrum of light elements of cosmic rays observed with KASCADE-Grande. *Physical Review D 87*, 8 (apr 2013), 081101.

[46] Arons, J., and Scharlemann, E. T. pair formation above pulsar polar caps - structure of the low altitude acceleration zone. *Astrophysical Journal 231* (aug 1979), 854.

[47] Atwood, W. B., Abdo, A. A., Ackermann, M., et al. the Large Area Telescope on the Fermi gamma-ray space telescope mission. *Astrophysical Journal 697*, 2 (may 2009), 1071–1102.

[48] Auger, P., Ehrenfest, P., Maze, R., Daudin, J., and Fréon, R. A. extensive cosmic-ray showers. *Reviews of Modern Physics 11*, 3-4 (jul 1939), 288–291.

[49] B. Rossi. interaction between cosmic rays and matter. *Nature 132*, 3326 (jul 1933), 173–174.

[50] Bai, Y., Carena, M., and Lykken, J. PAMELA excess from neutralino annihilation in the NMSSM. *Physical Review D 80*, 5 (sep 2009), 055004.

[51] Baltz, E. A., and Edsjö, J. positron propagation and fluxes from neutralino annihilation in the halo. *Physical Review D 59*, 2 (dec 1998), 023511.

[52] Bell, A. R. the acceleration of cosmic rays in shock fronts - I. *Monthly Notices of the Royal Astronomical Society 182*, 2 (feb 1978), 147–156.

[53] Bell, A. R. turbulent amplification of magnetic field and diffusive shock acceleration of cosmic rays. *Monthly Notices of the Royal Astronomical Society 353*, 2 (sep 2004), 550–448.

[54] Bergström, L., Bringmann, T., and Edsjö, J. new positron spectral features from supersymmetric dark matter: a way to explain the PAMELA data? *Physical Review D 78*, 10 (nov 2008), 103520.

[55] Bernardo, G. D., Evoli, C., Gaggero, D., et al. implications of the cosmic ray electron spectrum and anisotropy measured with fermi-LAT. *Astroparticle Physics 34*, 7 (feb 2011), 528–538.

[56] Bernlöhr, K. impact of atmospheric parameters on the atmospheric Cherenkov technique. *Astroparticle Physics 12*, 4 (jan 2000), 255–268.

[57] Bertero, M. linear inverse and III-posed problems. In *Advances in Electronics and Electron Physics Volume 75*, P. W. Hawkes, Ed., vol. 75 of *Advances in Electronics and Electron Physics*. Academic Press, New York, 1989, pp. 1–120.

[58] Bertone, G. *particle dark matter: observations, models and searches*. Cambridge University Press (CUP), 2009.

[59] Biasuzzi, B. *spectral energy distribution modeling of Markarian 501 through a non-linear least square minimization*. Phd thesis, Università degli Studi di Udine, 2016.

[60] Bitossi, M. *ultra-fast sampling and readout for the MAGIC-II telescope data acquisition system.* PhD thesis, Universita di Pisa, 2009.

[61] Blackett, P. *Proceedings of the International Conference on the Emission Spectra of the Night Sky and Aurorae* (1948), 34–35.

[62] Blandford, R. D., and Ostriker, J. P. particle acceleration by astrophysical shocks. *Astrophysical Journal 221* (apr 1978), L29+.

[63] Blasi, P. origin of the positron excess in cosmic rays. *Physical Review Letters 103*, 5 (jul 2009), 051104.

[64] Blümer, J., Engel, R., and Hörandel, J. R. cosmic rays from the knee to the highest energies. *Progress in Particle and Nuclear Physics 63*, 2 (oct 2009), 293–338.

[65] Bohren, C. F., and Albrecht, B. A. *atmospheric thermodynamics*. Oxford University press, 1998.

[66] Borla Tridon, D., Colin, P., Cossio, L., Doro, M., and Scalzotto, V. measurement of the cosmic electron plus positron spectrum with the MAGIC telescopes. In *Proceedings, 32nd International Cosmic Ray Conference (ICRC 2011)* (2011).

[67] Boudaud, M., Aupetit, S., Caroff, S., et al. a new look at the cosmic ray positron fraction. *Astronomy & Astrophysics 575* (feb 2015), A67+.

[68] Bowen, I. S., Millikan, R. A., and Neher, H. V. a very high altitude survey of the effect of latitude upon cosmic-ray intensities and an attempt at a general interpretation of cosmic-ray phenomena. *Physical Review 46*, 8 (oct 1934), 641–652.

[69] Brun, R., and Rademakers, F. ROOT — an object oriented data analysis framework. *Nuclear Instruments and Methods in Physics Research Section A: Accelerators, Spectrometers, Detectors and Associated Equipment 389*, 1-2 (apr 1997), 81–86.

[70] Carmona, E., et al. performance of the MAGIC stereo system. In *Proceedings, 32nd International Cosmic Ray Conference (ICRC 2011)* (2011).

[71] Carquín, E., Díaz, M. A., Gómez-Vargas, G. A., Panes, B., and Viaux, N. confronting recent AMS-02 positron fraction and Fermi-LAT extragalactic γ-ray background measurements with gravitino dark matter. *Physics of the Dark Universe 11* (mar 2016), 1–10.

[72] Chadwick, P. M., Lyons, K., McComb, T. J. L., et al. geomagnetic effects on atmospheric cerenkov images. *Journal of Physics G: Nuclear and Particle Physics 25*, 6 (jan 1999), 1223–1233.

[73] Chang, J., Adams, J. H., Ahn, H. S., et al. an excess of cosmic ray electrons at energies of 300–800 GeV. *Nature 456*, 7220 (nov 2008), 362–365.

[74] Chen, C.-H., Chiang, C.-W., and Nomura, T. dark matter for excess of AMS-02 positrons and antiprotons. *Physics Letters B 747* (jul 2015), 495–499.

[75] Chen, S.-L., Mohapatra, R. N., Nussinov, S., and Zhang, Y. R-parity breaking via type II seesaw, decaying gravitino dark matter and PAMELA positron excess. *Physics Letters B 677*, 5 (jun 2009), 311–317.

[76] Cheng, K. S., Ho, C., and Ruderman, M. energetic radiation from rapidly spinning pulsars. I - outer magnetosphere gaps. II - Vela and Crab. *Astrophysical Journal 300* (jan 1986), 500.

[77] Cherenkov, P. A. visible emission of clean liquids by action of gamma radiation. *Doklady Akademii Nauk SSSR 2* (1934), 451+.

[78] Cirelli, M., Kadastik, M., Raidal, M., and Strumia, A. model-independent implications of the $e^{\pm}$, cosmic ray spectra on properties of dark matter. *Nuclear Physics B 813*, 1-2 (may 2009), 1–21. [Addendum: Nucl. Phys.B873,530(2013)].

[79] Cline, J. M., and Scott, P. dark matter CMB constraints and likelihoods for poor particle physicists. *Journal of Cosmology and Astroparticle Physics 2013*, 03 (mar 2013), 044–044. [Erratum: JCAP1305,E01(2013)].

[80] Cocconi, G. influence of the earth's magnetic field on the extensive air showers. *Phys. Rev. 93*, 3 (feb 1954), 646–647.

[81] Commichau, S., Biland, A., Contreras, J., et al. Monte Carlo studies of geomagnetic field effects on the imaging air cherenkov technique. *Nuclear Instruments and Methods in Physics Research Section A: Accelerators, Spectrometers, Detectors and Associated Equipment 595*, 3 (oct 2008), 572–586.

[82] Commichau, S. C., Biland, A., Kranich, D., et al. geomagnetic field effects on the imaging air shower cherenkov technique. In *Proceedings, 30th International Cosmic Ray Conference (ICRC 2007)* (2007), vol. 3, pp. 1357–1360.

[83] Delahaye, T., Lineros, R., Donato, F., et al. galactic secondary positron flux at the earth. *Astronomy and Astrophysics 501*, 3 (jul 2009), 821–833.

[84] Domingo-Santamaria, E., Flix Molina, J., Scalzotto, V., Wittek, W., and Rico, J. The DISP analysis method for point-like or extended gamma source searches / studies with the MAGIC telescope. In *Proceedings, 29th International Cosmic Ray Conference (ICRC 2005)* (2005).

[85] Drury, L. O. an introduction to the theory of diffusive shock ‘ acceleration of energetic particles in tenuous plasmas. *Reports on Progress in Physics 46*, 8 (aug 1983), 973–1027.

[86] Drury, L. O. origin of cosmic rays. *Astroparticle Physics 39-40* (dec 2012), 52–60.

[87] Egberts, K. the cosmic-ray electron spectrum measured with H.E.S.S. *Proceeding of science EPS-HEP2009* (2009), 097.

[88] Engel, R., Heck, D., and Pierog, T. extensive air showers and hadronic interactions at high energy. *Annual Review of Nuclear and Particle Science 61*, 1 (nov 2011), 467–489.

[89] F. Hess, V. Über Beobachtungen der durchdringenden Strahlung bei sieben Freiballonfahrten. *Physikalische Zeitschrift 13* (November 1912), 1084–1091.

[90] Fan, Y.-Z., Zhang, B., and Chang, J. $e^{\pm}$ excesses in the cosmic ray spectrum and possible interpretations. *International Journal of Modern Physics D 19*, 13 (nov 2010), 2011–2058.

[91] Feng, L., Yang, R.-Z., He, H.-N., et al. AMS-02 positron excess: new bounds on dark matter models and hint for primary electron spectrum hardening. *Physics Letters B 728* (jan 2014), 250–255.

[92] Fermi, E. on the origin of the cosmic radiation. *Physical Review 75*, 8 (apr 1949), 1169–1174.

[93] Frank, I., and Tamm, I. coherent visible radiation of fast electrons passing through matter. *Comptes rendus de l'Académie des sciences de l'URSS 14* (1937), 109–114.

[94] Fruck, C., Gaug, M., Zanin, R., et al. A novel LIDAR-based atmospheric calibration method for improving the data analysis of MAGIC. In *Proceedings, 33rd International Cosmic Ray Conference (ICRC2013)* (2014), p. 1054.

[95] Galbraith, W., and Jelley, J. V. light pulses from the night sky associated with cosmic rays. *Nature 171*, 4347 (feb 1953), 349–350.

[96] Giavitto, G. *observing the VHE gamma-ray sky with the MAGIC telescopes: the blazar B3 22247 + 381 and the Crab pulsar*. Phd thesis, Universitat Autonoma de Barcelona, 2013.

[97] Giesen, G., Lesgourgues, J., Audren, B., and Ali-Haïmoud, Y. CMB photons shedding light on dark matter. *Journal of Cosmology and Astroparticle Physics 2012*, 12 (dec 2012), 008.

[98] Ginsburg, V. the quantum theory of radiation of an electron uniformly moving in a medium. *Journal of Physics-USSR 2* (1940), 441–452.

[99] Goebel, F., Bartko, H., Carmona, E., et al. upgrade of the MAGIC telescope with a multiplexed fiber-optic 2gsamples/s FADC data acquisition system. In *Proceedings, 30th International Cosmic Ray Conference (ICRC 2007)* (2007), vol. 3, pp. 1481–1484.

[100] Gold, T. rotating neutron stars as the origin of the pulsating radio sources. *Nature 218*, 5143 (may 1968), 731–732.

[101] Goldreich, P., and Julian, W. H. pulsar electrodynamics. *Astrophysical Journal 157* (aug 1969), 869.

[102] Greisen, K. end to the cosmic-ray spectrum? *Physical Review Letters 16*, 17 (apr 1966), 748–750.

[103] Grieder, P. K. *extensive air showers: high energy phenomena and astrophysical aspects - a tutorial, reference manual and data book*. Springer, Berlin, Heidelberg, 2010.

[104] Heitler, W. *the quantum theory of radiation*, 3rd ed. ed. Clarendon Press Oxford, 1954.

[105] Hillas, A. M. the origin of ultra-high-energy cosmic rays. *Annual Review of Astronomy and Astrophysics 22*, 1 (sep 1984), 425–444.

[106] Hillas, A. M. cerenkov light images of EAS produced by primary gamma. *International Cosmic Ray Conference 3* (Aug. 1985), 445–448.

[107] Hillas, A. M. differences between gamma-ray and hadronic showers. In *TeV Gamma-Ray Astrophysics*, vol. 75. Springer Science + Business Media, 1996, pp. 17–30.

[108] Hillas, A. M. cosmic rays: recent progress and some current questions. based on invited talk in "Cosmology, Galaxy Formation and Astroparticle Physics on the pathway to the SKA", Oxford, April 2006, 2006.

[109] Hirotani, K. outer-gap versus slot-gap models for pulsar high-energy emissions: the case of the Crab pulsar. *Astrophysical Journal 688*, 1 (oct 2008), L25–L28.

[110] Holder, J. VERITAS: status and performance. In *Science with the New Generation of High Energy Gamma-Ray Experiments* (oct 2007), World Scientific Pub Co Pte Lt.

[111] Hu, H. status of the EAS studies of cosmic rays with energy below 10^{16} eV. In *Proceedings, 31st International Cosmic Ray Conference (ICRC 2009)* (2009).

[112] Huang, X., Vertongen, G., and Weniger, C. probing dark matter decay and annihilation with Fermi LAT observations of nearby galaxy clusters. *Journal of Cosmology and Astroparticle Physics 2012*, 01 (jan 2012), 042–042.

[113] Hugoniot, H. sur la propagation du mouvement dans les corps et spécialement dans les gaz parfaits (première partie). *Journal de l'École Polytechnique 57* (1887), 3–97.

[114] Jackson, J. D., and Levitt, L. C. *classical electrodynamics*, 3rd ed. ed., vol. 15. Wiley, New York, NY, 1999.

[115] James, F., and Roos, M. Minuit: a system for function minimization and analysis of the parameter errors and correlations. *Computer Physics Communications 10*, 6 (dec 1975), 343–367.

[116] K. Gaisser, T. *cosmic rays and particle physics*. Cambridge University Press, 1990.

[117] Kachelriess, M. lecture notes on high energy cosmic rays. 17.th Jyväsklyä Summer School, 2008.

[118] Kamae, T., Karlsson, N., Mizuno, T., Abe, T., and Koi, T. parameterization of gamma, e+/- and neutrino spectra produced by p-p interaction in astronomical environment. *Astrophysical Journal 647*, 1 (aug 2006), 692–708. [Erratum: Astrophys. J.662,779(2007)].

[119] Kobayashi, T., Komori, Y., Yoshida, K., and Nishimura, J. the most likely sources of high-energy cosmic-ray electrons in supernova remnants. *Astrophysical Journal 601*, 1 (jan 2004), 340–351.

[120] Kobayashi, T., Komori, Y., Yoshida, K., et al. observations of high energy cosmic-ray electrons from 30 GeV to 3 TeV with emulsion chambers. *Astrophysical Journal 760*, 2 (nov 2012), 146.

[121] Kohri, K., Ioka, K., Fujita, Y., and Yamazaki, R. can we explain AMS-02 antiproton and positron excesses simultaneously by nearby supernovae without pulsars or dark matter? *Progress of Theoretical and Experimental Physics 2016*, 2 (feb 2016), 021E01.

[122] Kotera, K., and Olinto, A. V. the astrophysics of ultrahigh-energy cosmic rays. *Annual Review of Astronomy and Astrophysics 49*, 1 (sep 2011), 119–153.

[123] Kraushaar, W. L., and Clark, G. W. search for primary cosmic gamma rays with the satellite explorer XI. *Physical Review Letters 8*, 3 (feb 1962), 106–109.

[124] Li, T.-P., and Ma, Y.-Q. analysis methods for results in gamma-ray astronomy. *Astrophysical Journal 272* (sep 1983), 317.

[125] Linsley, J. evidence for a primary cosmic-ray particle with energy 10^{20} eV. *Physical Review Letters 10*, 4 (feb 1963), 146–148.

[126] Longair, M. S. *high energy astrophysics, 3rd edn.* No. 2. Cambridge University Press, mar 2011.

[127] López, A., Savage, C., Spolyar, D., and Adams, D. Q. Fermi/LAT observations of dwarf galaxies highly constrain a dark matter interpretation of excess positrons seen in AMS-02, HEAT, and PAMELA. In *Meeting of the APS Division of Particles and Fields (DPF 2015) Ann Arbor, Michigan, USA, August 4-8, 2015* (mar 2016), vol. 2016, IOP Publishing, pp. 033–033.

[128] Lorimer, D. R., and Kramer, M. *handbook of pulsar astronomy.* Cambridge Observing Handbooks for Research Astronomers. Cambridge University Press, Oct. 2012.

[129] Malyshev, D., Cholis, I., and Gelfand, J. pulsars versus dark matter interpretation of ATIC/PAMELA. *Physical Review D 80*, 6 (sep 2009), 063005.

[130] Marrocchesi, P. S. CALET on the ISS: a high energy astroparticle physics experiment. *Journal of Physics: Conference Series 718* (may 2016), 052023.

[131] Mauro, M. D., Donato, F., Fornengo, N., and Vittino, A. dark matter vs. astrophysics in the interpretation of AMS-02 electron and positron data. *Journal of Cosmology and Astroparticle Physics 2016*, 05 (may 2016), 031–031.

[132] Mertsch, P., and Sarkar, S. AMS-02 data confront acceleration of cosmic ray secondaries in nearby sources. *Physical Review D 90*, 6 (sep 2014), 061301.

[133] Millikan, R. A., and Cameron, G. H. Hhgh frequency rays of cosmic origin III. measurements in snow-fed lakes at high altitudes. *Physical Review 28*, 5 (nov 1926), 851–868.

[134] Mirzoyan, R. on the calibration accuracy of light sensors in atmospheric cherenkov fluorescence and neutrino experiments. In *Proceedings, 25th International Cosmic Ray Conference (ICRC 1997)* (1997), vol. 7, p. 265.

[135] Mirzoyan, R., Kankanian, R., Krennrich, F., et al. the first telescope of the HEGRA air cherenkov imaging telescope array. *Nuclear Instruments and Methods in Physics Research Section A: Accelerators, Spectrometers, Detectors and Associated Equipment 351*, 2-3 (dec 1994), 513–526.

[136] Moralejo, A., et al. MARS, the MAGIC analysis and reconstruction software. In *Proceedings, 31st International Cosmic Ray Conference (ICRC 2009)* (2009).

[137] Morlino, G. the role of ionization in the shock acceleration theory. *Monthly Notices of the Royal Astronomical Society 412*, 4 (feb 2011), 2333–2344.

[138] Moskalenko, I. V., and Strong, A. W. production and propagation of cosmic-ray positrons and electrons. *Astrophysical Journal 493*, 2 (feb 1998), 694–707.

[139] Moskalenko, I. V., Strong, A. W., and Reimer, O. diffuse gamma rays. In *Cosmic Gamma-Ray Sources*. Springer Science + Business Media, 2004, pp. 279–310. [Astrophys. Space Sci. Libr.304,279(2004)].

[140] Mücke, A. Mmdeling the April 1997 flare of Mkn 501. In *AIP Conference Proceedings* (2000), AIP Publishing, pp. 149–153. [AIP Conf. Proc.515,149(2000)].

[141] Muslimov, A. G., and Harding, A. K. high-altitude particle acceleration and radiation in pulsar slot gaps. *Astrophysical Journal 606*, 2 (may 2004), 1143–1153.

[142] Musser, J. limits on the multi-TeV cosmic ray electron flux from CREST. In *Proceedings, 34th International Cosmic Ray Conference (ICRC 2015)* (2015).

[143] Neronov, A., Semikoz, D. V., and Taylor, A. M. low-energy break in the spectrum of galactic cosmic rays. *Physical Review Letters 108*, 5 (jan 2012), 051105.

[144] Ney, E. P. cosmic radiation and the weather. *Nature 183*, 4659 (feb 1959), 451–452.

[145] Nishimura, J., Fujii, M., Taira, T., et al. emulsion chamber observations of primary cosmic-ray electrons in the energy range 30-1000 GeV. *Astrophysical Journal 238* (may 1980), 394.

[146] Olive, K. review of particle physics. *Chinese Physics C 38*, 9 (aug 2014), 090001.

[147] Oser, S., Bhattacharya, D., Boone, L. M., et al. high-energy gamma-ray observations of the Crab Nebula and pulsar with the solar tower atmospheric cerenkov effect experiment. *Astrophysical Journal 547*, 2 (feb 2000), 949–958.

[148] Ostrowski, M. mechanisms and sites of ultra high energy cosmic ray origin. *Astroparticle Physics 18*, 3 (dec 2002), 229–236.

[149] Pacini, D. la radiazione penetrante alla superficie ed in seno alle acque. *Il Nuovo Cimento 3*, 1 (dec 1912), 93–100.

[150] Pacini, F. energy emission from a neutron star. *Nature 216*, 5115 (nov 1967), 567–568.

[151] Panov, A. D., Zatsepin, V. I., Sokolskaya, N. V., et al. possible structure in the cosmic ray electron spectrum measured by the ATIC-2 and ATIC-4 experiments. *Astrophysics and Space Sciences Transactions 7*, 2 (apr 2011), 119–124.

[152] Paoletti, R., Bigongiari, C., Bitossi, M., Cecchi, R., and Pegna, R. The global trigger system of the magic telescope array. In *2008 IEEE Nuclear Science Symposium Conference Record* (oct 2008), Institute of Electrical & Electronics Engineers (IEEE), pp. 2781–2783.

[153] Paoletti, R., Cecchi, R., Corti, D., et al. the trigger system of the MAGIC telescope. *IEEE Transactions on Nuclear Science 54*, 2 (apr 2007), 404–409.

[154] Pierbattista, M. *gamma-ray pulsar physics: gap-model populations and light-curve analyses in the FERMI era*. Phd thesis, Université Paris 7, 2013.

[155] Pierbattista, M., Harding, A. K., Gonthier, P. L., and Grenier, I. A. young and middle age pulsar light-curve morphology: comparison of Fermi observations withγ-ray and radio emission geometries. *Astronomy & Astrophysics 588* (apr 2016), A137.

[156] Pohl, M. cosmic-ray electron signatures of dark matter. *Physical Review D 79*, 4 (feb 2009), 041301.

[157] Profumo, S. dissecting cosmic-ray electron-positron data with Occam's Razor: the role of known pulsars. *Open Physics 10*, 1 (jan 2012), 1–31.

[158] Rankine, W. J. M. on the thermodynamic theory of waves of finite longitudinal disturbance. *Philosophical Transactions of the Royal Society A: Mathematical, Physical and Engineering Sciences 160* (1870), 277–288.

[159] Rao, M. V. S., and Sreekantan, B. V. *extensive air showers*. World Scientific Pub Co Pte Lt, Singapore, oct 1998.

[160] Rossi, B., and Greisen, K. cosmic-ray theory. *Reviews of Modern Physics 13*, 4 (oct 1941), 240–309.

[161] Rubin, V. C., and W. Kent, J. F. rotation of the andromeda nebula from a spectroscopic survey of emission regions. *Astrophysical Journal 159* (feb 1970), 379.

[162] Schmelling, M. the method of reduced cross-entropy a general approach to unfold probability distributions. *Nuclear Instruments and Methods in Physics Research Section A: Accelerators, Spectrometers, Detectors and Associated Equipment 340*, 2 (feb 1994), 400–412.

[163] Schure, K. M., Bell, A. R., Drury, L. O., and Bykov, A. M. diffusive shock acceleration and magnetic field amplification. *Space Science Reviews 173*, 1-4 (apr 2012), 491–519.

[164] Serpico, P. D. astrophysical models for the origin of the positron "excess". *Astroparticle Physics 39-40* (dec 2012), 2–11.

[165] Shen, C. S., and Mao, C. Y. anisotropy of high energy cosmic-ray electrons in the discrete source model. *Astrophysical Letters 9* (1971), 169.

[166] Simpson, J. A. elemental and isotopic composition of the galactic cosmic rays. *Annual Review of Nuclear and Particle Science 33*, 1 (dec 1983), 323–382.

[167] Slatyer, T. R., Padmanabhan, N., and Finkbeiner, D. P. CMB constraints on WIMP annihilation: energy absorption during the recombination epoch. *Physical Review 80*, 4 (aug 2009), 043526.

[168] Sreekumar, P., Bertsch, D. L., Dingus, B. L., et al. constraints on the cosmic rays in the small magellanic cloud. *Physical Review Letters 70*, 2 (jan 1993), 127–129.

[169] Staszak, D. A cosmic-ray electron spectrum with VERITAS. In *Proceedings, 34th International Cosmic Ray Conference (ICRC 2015)* (2015).

[170] Steinke, B. *first study of fast variability in Markarian 421 with the MAGIC stereoscopic system.* Phd thesis, Technical University Munich, 2012.

[171] Strong, A. W., and Moskalenko, I. V. propagation of cosmic-ray nucleons in the galaxy. *Astrophysical Journal 509*, 1 (dec 1998), 212–228.

[172] Strong, A. W., Moskalenko, I. V., and Ptuskin, V. S. cosmic-ray propagation and interactions in the galaxy. *Annual Review of Nuclear and Particle Science 57*, 1 (nov 2007), 285–327.

[173] Strzys, M. private communication.

[174] Sturrock, P. A. a model of pulsars. *Astrophysical Journal 164* (mar 1971), 529.

[175] Taylor, J. H., and Manchester, R. N. recent observations of pulsars. *Annual Review of Astronomy and Astrophysics 15*, 1 (sep 1977), 19–44.

[176] Thoudam, S., Rachen, J. P., van Vliet, A., et al. cosmic-ray energy spectrum and composition up to the ankle - the case for a second galactic component. Submitted to Astronomy & Astrophysics, 2016.

[177] Tikhonov, A., and Arsenin, V. methods of solution of Ill-posed problems. *SIAM Rev. 21*, 2 (apr 1977), 266–267.

[178] Torii, S. overview of the CALET mission to the ISS. In *Proceedings, 32nd International Cosmic Ray Conference (ICRC 2011)* (2011), vol. 6, p. 351.

[179] Tsai, Y.-S. pair production and bremsstrahlung of charged leptons. *Reviews of Modern Physics 46*, 4 (oct 1974), 815–851. [Erratum: Rev. Mod. Phys.49,521(1977)].

[180] Ulrich, R., Engel, R., and Unger, M. hadronic multiparticle production at ultra-high energies and extensive air showers. *Physical Review D 83*, 5 (mar 2011), 054026.

[181] Unger, M. cosmic rays above the knee. Invited talk at the 21st European Cosmic Ray Symposium, 2008, Kosice, 2008.

[182] Völk, H. J., Berezhko, E. G., and Ksenofontov, L. T. new evidence for strong nonthermal effects in Tycho's supernova remnant. *Astrophysics and Space Science 309* (2007), 389–394.

[183] Völk, H. J., and Bernlöhr, K. imaging very high energy gamma-ray telescopes. *Experimental Astronomy 25*, 1-3 (mar 2009), 173–191.

[184] Wagner, R. *measurement of very high energy gamma-ray emission from four blazars using the MAGIC telescope and a comparative blazar study.* Phd thesis, Technical University Munich, 2006.

[185] Watson, A. A. high-energy cosmic rays and the Greisen–Zatsepin–Kuz'min effect. *Reports on Progress in Physics 77*, 3 (feb 2014), 036901.

[186] Weekes, T. C., Cawley, M. F., Fegan, D. J., et al. observation of TeV gamma rays from the Crab Nebula using the atmospheric cerenkov imaging technique. *Astrophysical Journal 342* (jul 1989), 379.

[187] Wittek, W. image parameters. *MAGIC TDAS 02-03* (2002).

[188] Yang, R.-Z., de Oña Wilhelmi, E., and Aharonian, F. probing cosmic rays in nearby giant molecular clouds with the Fermi Large Area Telescope. *Astronomy & Astrophysics 566* (jun 2014), A142.

[189] Yoshida, K., Torii, S., Yamagami, T., et al. cosmic-ray electron spectrum above 100GeV from PPB-BETS experiment in Antarctica. *Advances in Space Research 42*, 10 (nov 2008), 1670–1675.

[190] Zatsepin, G. T., and Kuzmin, V. A. upper limit of the spectrum of cosmic rays. *JETP Letters 4* (1966), 78–80. [Pisma Zh. Eksp. Teor. Fiz.4,114(1966)].

[191] Zwicky, F. on the masses of nebulae and of clusters of nebulae. *Astrophysical Journal 86* (oct 1937), 217.

Danksagung

An dieser Stelle möchte ich den Menschen danken, die mich während meiner Doktorarbeit begleitet haben.

- Elisa Bernardini, die mir das alles überhaupt erst ermöglicht hat. Danke auch für die immer verfgbare Unterstützung und Hilfestellung bei der Organisation von Forschungsaufenthalten und Konferenzbesuchen.
- Pierre Colin für die vielen Tips und Ratschläge. Und dafür, dass er immer Zeit für Fragen hatte.
- Meike de With und Gessica de Caneva für das Mitfiebern und Mitleiden, das Korrekturlesen und alles Andere.
- Giovanna Pedaletti für ihr offenes Ohr und ihre zahlreichen Ratschläge zur Implementierung und ihr detailliertes Korrekturlesen.
- Michele Palatiello dafür, dass er das Ganze mit mir bis zum Ende durchgezogen hatte.
- Der Zeuthener IceCube-Gruppe für das Asyl, wenn meine Gruppe mal wieder nur aus mir bestand.
- Der, kleinen aber feinen, Zeuthener MAGIC-Gruppe für eine entspannte und freundliche Arbeitsatmosphäre.
- Der MAGIC Kollaboration für die interessante und lehrreiche Zeit auf La Palma sowie bei den Kollaborationstreffen.
- Last, but not least meinen Korrekturlesern Gerhard, Lisa, Konstancja und Simon für die vielen nützlichen Tips!

Selbstständigkeitserklärung

Ich erkläre, dass ich die Dissertation selbständig und nur unter Verwendung der von mir gemäß § 7 Abs. 3 der Promotionsordnung der Mathematisch-Naturwissenschaftlichen Fakultät, veröffentlicht im Amtlichen Mitteilungsblatt der Humboldt-Universität zu Berlin Nr. 126/2014 am 18.11.2014, angegebenen Hilfsmittel angefertigt habe.